Dendrites Inhibition in Rechargeable Lithium Metal Batteries

Thesis by

Asghar Aryanfar

In Partial Fulfillment of the Requirements

for the Degree of

Doctor of Philosophy

California Institute of Technology

Pasadena, California

2015

(Defended April 22, 2015)

In memory of maman

for baba, Parisa, Fariba, Zahra and Akbar

0.1 Acknowledgements

I would like to end my long and exciting PhD journey by saying a big "THANK YOU" to all the productive discussions with collaborators.

First and foremost, I should thank Prof. Michael Hoffmann and Prof. William Goddard for introducing me to the post-graduate world and giving me the freedom to follow my passion and discover the "new".

I consider myself lucky to have eventually found what I love to do and to wake up every day happy and excited about the day to come. This wouldn't be possible without the unconditional support and love from my family: My sisters Parisa, Fariba, Zahra, and my brother Akbar. I always missed you. We went through extremely difficult times together, right before I came to California, but despite the distance we stayed close and I am just wordless how to thank you.

A genuine thanks to Dr. Agustin Colussi for providing skillful guidance with contagious enthusiasm and inspiration. AJ encouraged me to discover new fields and enlarge my knowledge to better embrace physical and electrochemistry. I will remember his passionate and absolute discipline during entire my future career. My sincere thanks also goes to Daniel Brooks, Tao Cheng and Boris Merinov, for all the productive collaborations.

I would like to thank my thesis committee members, Prof.s Julia Greer, Austin Minnich and Jose Andrade for being willing to spend their precious time on my dissertation.

Farshid Roumi and Clement Cid, thanks for introducing me to the world of batteries and boosting my experimental knowledge. I should not forget other lab members for on and off discussions: Rifkha Kameel, Xing Xie, Hanspeter Zöllig, Francesca Riboni, Dae Jung Kwon, Kangwoo Cho, Hao Zhang, Cody Finke, Yan Qu and Yang Yang. My thanks to Caltech friends I have continuously been in touch with: Ramses Mourhatch, Mohsen Chitsaz, Ramathasan Thevamaran, Srivatsan Hulikal, Aaron Towne and Toktam Mohammadnejad. They all made Caltech an awesome place to work in.

I would also like to thank department assistants Nora Oshima, Kathy Young, and Megan Schmid and office of Dean of Graduate studies, Ms. Natalie Gilmore and Felicia Hunt and Prof. Joseph Shepherd for their accommodations.

I also acknowledge Prof.s Brent Fultz, Nadia Lapusta, and Richard Murray for spending their times for on and off discussions.

My thanks also go to Nathan Dalleska and Su Young Ryo for solving my instrumentation-related problems. Finally, I would like to thank Nazanin Mossahebi, Mernaz Masoumi, Parisa Kadivar, Mohammad Reza Rajati, Mojgan Yousefi, and Hossein Sharifazadeh for their continuous support during my PhD years.

0.2 Abstract

The specific high energy and power capacities of rechargeable lithium metal (Li^0) batteries are ideally suited to portable devices that are valuable as storage units for intermittent renewable energy sources. Lithium, the lightest (M=6.94 $g.mol^{-1}$ & ρ=0.53$g.cm^{-3}$) and most electropositive metal (E^0=-3.04V vs SHE), would be the optimal anode material for rechargeable batteries if it wouldn't lead to unexpected failure of such devices due to short-circuiting via *dendrites* that grow across electrodes upon recharging. This phenomenon poses a major safety issue because it triggers a series of adverse events that start with overheating, followed by the thermal decomposition and ultimately the ignition of the organic solvents used in such devices. During subsequent discharge periods, the lithium dendrites isolate from the electrode and form *Dead Lithium*, which is electrochemically inactive and causes the battery capacity fade.

In this thesis, we developed an experimental platform for understanding, tracking and quantifying the dendrite populations grown in a Li battery prototype upon charging under various conditions. Simultaneously, we developed a computational framework for predicting the dynamics of dendrite propagation. The coarse-grained Monte Carlo model assisted us in the interpretation of pulsing experiments, whereas MD calculations provided insights into the mechanism of dendrites thermal relaxation. Furthermore, we have developed alghorithms to quantify the battery capacity loss from detached dead lithium crystals.

Contents

List of Figures

Chapter 1

Introduction to Batteries

Battery is an electrochemical devices that stores electrical energy in the chemical bonds. Rechargeable batteries are the most common energy storage system for clean source for electronic portable devices, hybrid and electric vehicles, satellites, electric grids and modern medicine applications. Despite impressive growth of batteries applications in daily lifestyle, the underlying science and technology needs fast advancement. Certainly, when compared, energy storage cannot keep pace with the rate of progress in the computer industry. Moore's law predicts a doubling of memory capacity every two years.

A battery is composed of several electrochemical cells that are connected in series and/or in parallel to provide the required voltage or capacity, respectively. Each cell consists of a positive and a negative electrode (both sources of chemical reactions) separated by electrolyte solution/solid electrolyte containing dissociated salts, which enable ion transfer between two electrodes. Once these electrodes are connected externally, the chemical reactions proceed in tandem at both electrodes., thereby liberating electrons electrons and enabling the current to be tapped by the user.

1.1 Historical Developments

The first practical battery is the generally known *Volta Cell* (also called the *Galvanic cell*. It's invention, over two centuries ago, spawned the invention of variety of batteries based principally on the Volta cell. However, interestingly, during the last century, only three batteries, namely, the MnO_2 primary battery, and the secondary batteries of lead/acid or nickel (cadmium-metal hydrite) have been in use. while these batteries are reaching their technical limit, new concepts have been used in development of lithium ion and lithium metal secondary batteries with higher ability during recent decades.

The motivation for using a battery technology based on Lithium metal as anode relied initially on the fact that Li is the most electropositive (-3.04V vs SHE) as well as the lightest (M=6.94 g.mol^{-1} & ρ=0.53g.cm^{-3}) metal, thus facilitating the design of storage systems with high energy density. (Fig. 1.4) The advantage in using Lithium metal was first demonstrated in the 1970's with the assembly of primary (non-rechargeable) Li cells. Over the same period numerous inorganic compounds were shown to react with alkali metals in a reversible way. the discovery of such materials, which were later identified as intercalation compounds, was crucial in the development of high-energy rechargeable Li systems. The system however encountered the shortcomings of a Li-metal/liquid electrolyte combination. Uneven (dendritic) Li growth as the metal was replayed during each subsequent cycle. (Fig.1.1)

1.2 Basics of Current Li-ion batteries

Li can be used as a charge carrier in almost all diffuse all electrode candidate materials that can conducts electrons. When two different electrodes are in put in contact physical contact via the electrolyte, the Li atoms diffuse from the electrode with a high electrochemical potential (i.e., the negative electrode) to the electrode with a low electrochemical potential (i.e., the positive electrode). The electrolyte is a solution

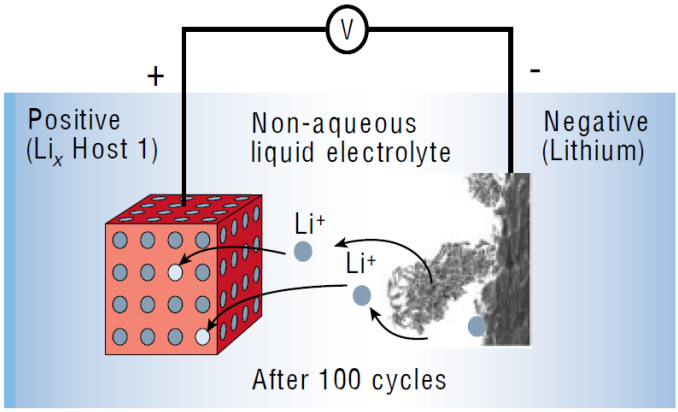

Figure 1.1: Rechargeable lithium metal with Li dendrite produced in the anode surface. [1]

that conducts Li-ions but not electrons. When the battery discharges, Li-ions are produced in the anode, diffuse through the electrolyte and get reduced in the the cathode. The electrons flow through an external circuit from the negative to the positive electrode and provide the electrical energy for the intended device. Both the ionic and the electronic processes are reversed during recharge by an external power source.(Fig. 1.1)

1.3 Thermodynamics

The energy storage and power characteristics of batteries follow directly the thermodynamic and kinetic formulations for chemical reactions. [4] The basic thermodynamics for a reversible electrochemical reaction is:

$$\Delta G = \Delta H - T\Delta S \tag{1.1}$$

where G is the Gibbs free energy, or the available energy in a reaction for the useful work, H is the enthalpy, or the energy released by the reaction, S is the entropy, and T is the absolute temperature, with $T\Delta S$ being the heat associated with the reaction. The terms ΔG , ΔH and ΔS are state functions and depend only on the chemistry of the electrode materials and the initial and final states of the reactions. The free

energy, ΔG represents the net useful energy available from a given reaction, thus, the net available electrical energy from a reaction in a battery cell is given by:

$$\Delta G = -nFE \tag{1.2}$$

where n is the number of electrons transferred per mole of reactants, F is the Faraday constant, and E is the voltage of the cell corresponding to the electrode/electrolyte chemistry and state of charge. Equation 1.2 represents the balance between the chemical and electric driving forces upon the ions under open circuit conditions, hence E refers to the open circuit potential of a cell where there is no current flowing. The open circuit potential is determined by the difference in the electrically neutral chemical compositions of the electrodes. The chemistry of the electrolyte interface reactions play no role due to absence of net current. The amount of electricity produced, nF, is determined by the total amount of available charge carriers which is a measure for battery capacity. the voltage is an intensive parameter.[5]

The change of free energy for a given species i defines the chemical potential. The chemical potential μ_i is related to another thermodynamic quantity, the activity a_i:

$$\mu_i = \mu_i^0 + RTln(a) \tag{1.3}$$

where μ_i^0 is a constant, the value of the chemical potential of species i in its standard state. R is the gas constant, and T the absolute temperature. Consider an electrochemical cell in which the activity of species i is different in the two electrodes, $a_i(-)$ in the negative electrode, and $a_i(+)$ in the positive electrode. The difference between the chemical potential on the positive side and that on the negative side is written as $\mu_i^+ - \mu_i^- = RTln[a_i(+)/a_i(-)]$. If this chemical potential difference is balanced by the electrostatic energy from Equation 1.2, we have:

$$E = \frac{RT}{nF} ln[\frac{a_i(+)}{a_i(-)}] \tag{1.4}$$

The above relation is the Nernst equation, which relates the measurable cell volt-

age to the chemical difference across an electrochemical cell. If the activity of species i in one of the electrodes is a standard reference value, the Nernst equation provides the relative electrical potential of the other electrode.[5].

1.4 Kinetics

Thermodynamics describes reactions at equilibrium and the maximum energy available for a given reaction. Compared to the open circuit potential at equilibrium state, the voltage drops off when current is drawn from the battery because of kinetic limitations of reactions. Figure 1.2 shows a typical discharge curve of a battery. [5, 6] However, the detailed mechanism of battery electrode reactions often involves a series of physical, chemical, and electrochemical steps, including charge-transfer and charge transport reactions. The rates of these individual steps determine the kinetics of the electrode. Basically, three different kinetics effects for polarization are often considered: (1) activation polarization is related to the kinetics of the electrochemical redox (or charge-transfer) reactions taking place at the electrode/electrolyte interfaces of anode and cathode; (2) ohmic polarization is correlated to the resistance of individual cell components and to the resistance due to contact problems between the cell components; (3) concentration polarization is due to mass transport limitations during cell operation.[6]

Activation polarization arises from kinetics of the charge-transfer reaction taking place at the electrode/electrolyte interface. This type of kinetics is best understood using transition-state theory. The current flow is often described by the Butler-Volmer equation:

$$j = j_0\{exp[\frac{\alpha nF\eta}{RT}] - exp[-\frac{\alpha_c nF\eta}{RT}]\} \tag{1.5}$$

where j is the electrode current density, j_0 is the exchange current density, T is the absolute temperature, n is the ionic valence number, F is the Faraday constant, R is universal gas constant, α_c and α_a are cathodic and anodic charge transfer coefficients

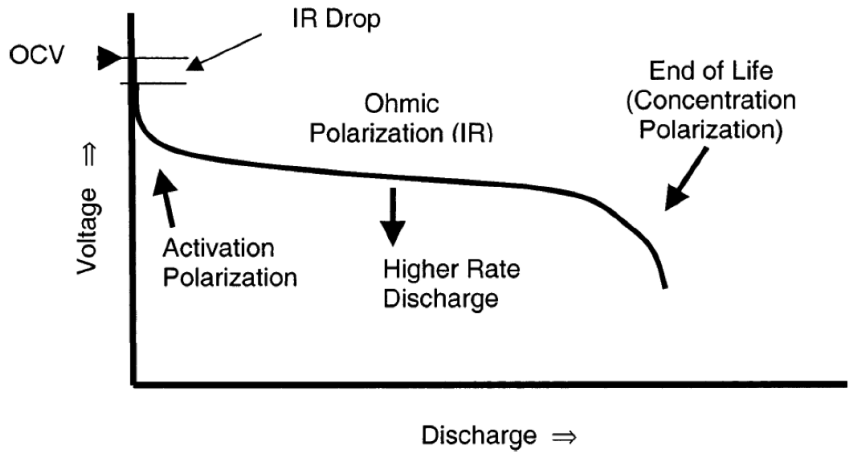

Figure 1.2: A typical discharge curve of a battery.

and η is the activation over-potential defined as below:

$$\eta = E - E_{eq} \tag{1.6}$$

where E is the electrode potential and E_{eq} is the equilibrium potential.

The ohmic losses arises from the resistance of the electrolyte, materials of constructions of the electrodes, current collectors, terminals and contact between particles of the active mass. Ohmic polarization appears or disappears instantaneously when current flows or ceases. Typically the linear Ohm's law relates the current and potential. As the redox reactions proceed, the availability of the active species at the electrode/electrolyte interface changes. Concentrations polarization arises from limited mass transport capabilities, for example, limited diffusion of active species to and from the electrode surface to replace the reacted material to sustain the reactions. This type of polarization usually becomes the rate-limiting step at the completion of charge/discharge.

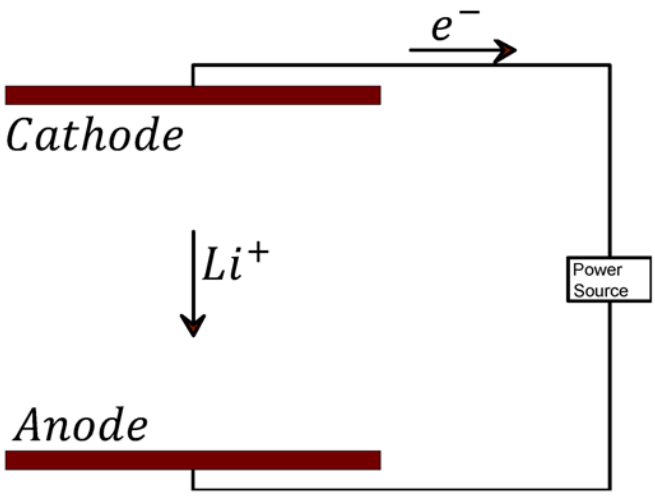

Figure 1.3: Schematic representation of battery during charge period, forming lithium dendrites.

1.5 Metrics

Batteries are evaluated with their charge capacity (Q), voltage (V), current (I), cyclability (charge and energy efficiency), energy density (mAh.g^{-1} or mAh.L^{-1}), power density (Wh.g^{-1} or Wh.L^{-1}) and cost. These parameters are a function of chemical (μ)/ electrical ($\vec{E}$) and mechanical (σ) interactions among cathode as well as chemical and physical properties of anode, cathode and electrolyte as the three main components forming a battery cell. In lithium batteries, lithium ions migrate from anode to cathode in discharge and vice versa in charge. The electrodes act as a medium for redox (reduction/oxidation) reactions and are host to lithium ions. The battery capacity is determined by minimum lithium-hosting capacity of cathode and anode materials/components. The cycling rate is determined by electrolyte conductivity and the voltage.[1]

Measures of battery performance are related to intrinsic property of the materials that form the positive and negative electrodes. The cycle-life and lifetime are dependent to the nature of the interfaces between the electrodes and electrolyte, whereas safety is a function of the electrode materials and interfaces.

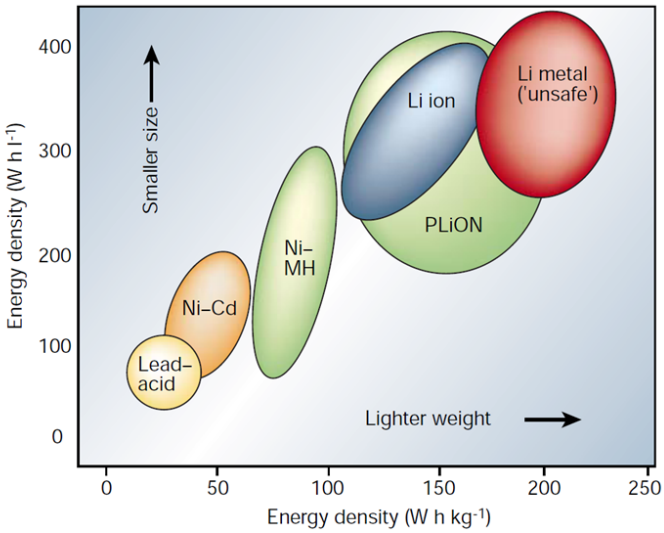

Figure 1.4: Comparison of different battery technologies in terms of volumetric and gravimetric energy density.[1]

Energy density of electrode material is defined as its capacity for hosting lithium ions per unit of mass or volume. Fig. 1.4 shows the comparison of energy density of different battery materials.

Regardless of battery type, nonuniform electrodeposition on the anode and dendritic growth usually creates amorphous dendrites(Fig.1.5). Dendrite shape ranges from nearly linear and pointed (needle-like) to highly branched (bush-like). [7] Lithium crystals grow on the anode surface upon charge in each cycle.(Fig. 1.3) Any asperity on the surface acts as a sink for cations with random movements, since it provides more surface area and also is relatively closer to them.

On the other hand, during each subsequent discharge, part of lithium dendrite is separated from the rest of the crystal due to nonuniform dissolution in different dendritic sites. The corresponding isolated crystals are identified as *Dead Lithium* as they are electrochemically inactive but chemically active due to high surface area and may cause thermal instabilities. Fig. 1.6 shows the schematic representation of formation of dead lithium crystals. In this thesis we seek to characterize lithium dendrite evolution based on physical/environmental parameters and inhibit/prevent their formation/propagation.

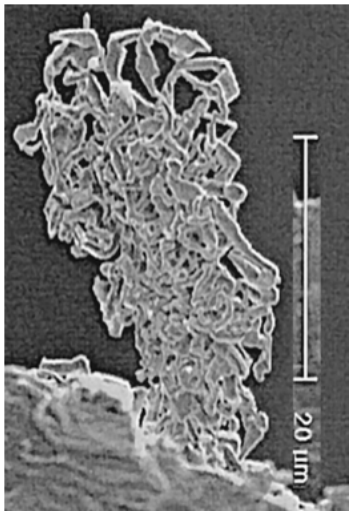

Figure 1.5: SEM image of typical lithium dendrite.[2]

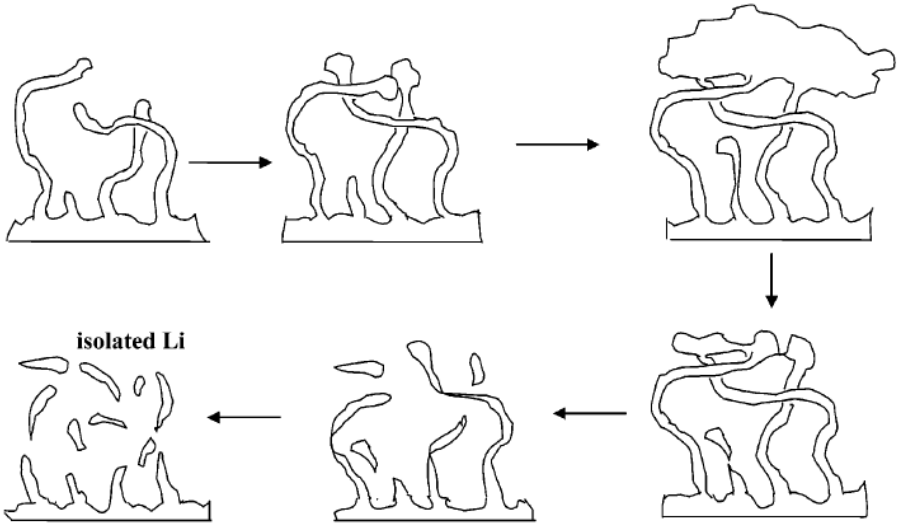

Figure 1.6: Schematic description for the formation of isolated lithium particles from Li dendrites. The uneven dissolution of dendrites leaves lithium crystals detached from the lithium substrate. The isolated lithium crystals become electrochemically *dead* but chemically reactive due to their high surface area. [3]

Chapter 2

Pulse Charging

Acknowledgement: The main part of this chapter is published in the Journal of Physical Chemistry Letters, 2014, 5(10), pp 1721-1726.[8]

http://pubs.acs.org/doi/abs/10.1021/jz500207a

2.1 Abstract

Short-circuiting via dendrites compromises the reliability of Li-metal batteries. Dendrites ensue from instabilities inherent to electrodeposition that should be amenable to dynamic control. Here, we report that by charging a scaled coin-cell prototype with 1 ms pulses followed by 3 ms rest periods the average dendrite length is shortened ∼2.5 times relative to those grown under continuous charging. Monte Carlo simulations dealing with Li^+ diffusion and electromigration reveal that experiments involving 20 ms pulses were ineffective because Li^+ migration in the strong electric fields converging to dendrite tips generates extended depleted layers that cannot be replenished by diffusion during rest periods. Because the application of pulses much shorter than the characteristic time τ_c = O(∼1 ms) for polarizing electric double layers in our system would approach DC charging, we suggest that dendrite propagation can be inhibited (albeit not suppressed) by pulse charging within appropriate frequency ranges.

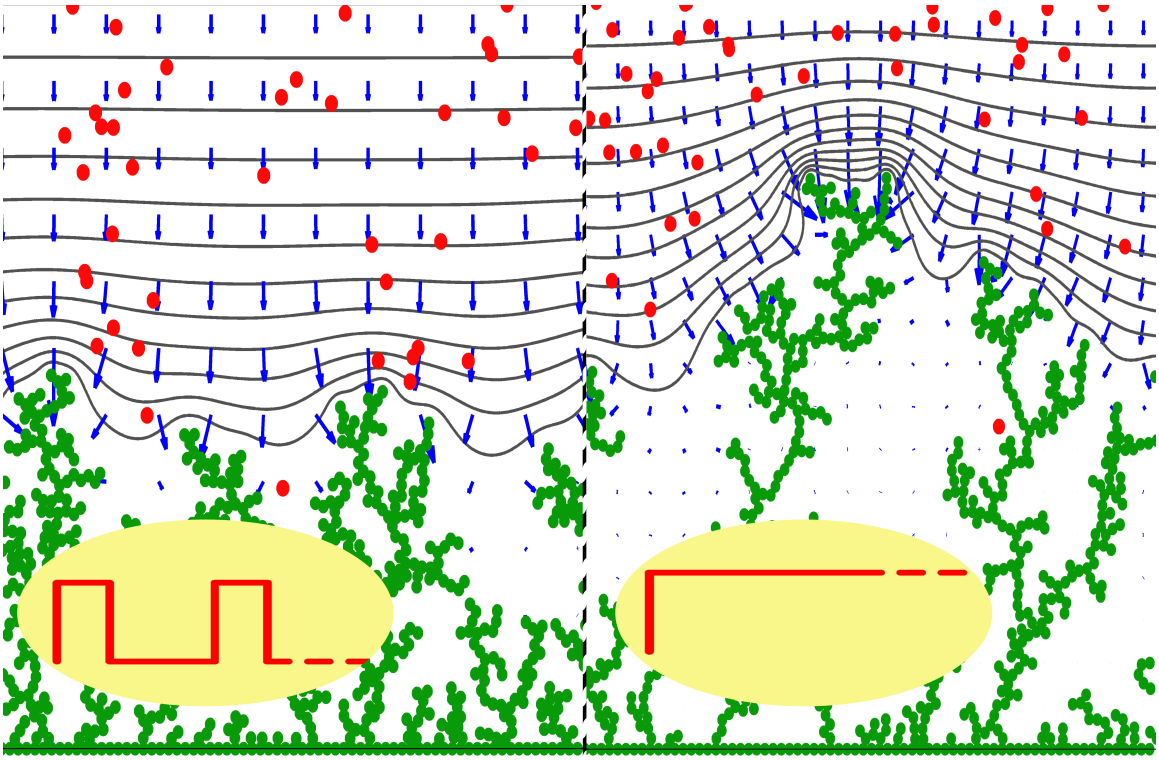

Figure 2.1: Graphical Abstract.

2.2 Introduction

The specific high energy and power capacities of lithium metal (Li^0) batteries are ideally suited to portable devices and are valuable as storage units for intermittent renewable energy sources.[9, 10, 11, 12, 13, 14, 15] Li^0, the lightest and most electropositive metal, would be the optimal anode material for rechargeable batteries if it were not for the fact that such devices fail unexpectedly by short-circuiting via the dendrites that grow across electrodes upon recharging.[16, 17] This phenomenon poses a major safety issue because it triggers a series of adverse events that start with overheating, which is potentially followed by the thermal decomposition and ultimately the ignition of the organic solvents used in such devices.[18, 19, 3] Li^0 dendrites have been imaged, probed, and monitored with a wide array of techniques.[12, 13, 20] Moreover, their formation has been analyzed[21, 22] and simulated at various levels of realism.[17, 23, 24] Numerous empirical and semi-empirical strategies have been employed for mitigating the formation of Li^0 dendrites that were mostly based on

modifications of electrode materials and morphologies and variations of operational conditions.[10] Thus, reports can be found on the effects of current density,[25, 2, 7] electrode surface morphology,[18] solvent and electrolyte composition,[26, 27, 28, 29] electrolyte concentration,[25] evolution time,[30] the use of powder electrodes,[31] and adhesive lamellar block copolymer barrier[32] on dendrite growth. We suggest that further progress in this field should accrue from the deeper insights into the mechanism of dendrite propagation that could be gained by increasingly realistic and properly designed experiments and modeling calculations.[28] We considered that Li^0 dendrite nucleation and propagation are intrinsic to electrodeposition as a dynamic process under nonequilibrium conditions.[13, 21] Furthermore, in contrast with purely diffusive crystal growth, Li-ion (Li^+) electro-migration is an essential feature of electrolytic dendrite growth.[33] More specifically, we envisioned that runaway dendrite propagation could be arrested by the relaxation of the steep Li^+ concentration gradients that develop around dendrite tips during charging. This is not a new strategy,[4] but to our knowledge the quantitative statistical impact of pulses of variable duration on dendrite length has not been reported before. Herein, we report experiments focusing on dendrite growth in a scaled coin cell prototype fitted with Li^0 electrodes charged with rectangular cathodic pulses of variable frequencies in the kHz range. We preserve the geometry and aspect ratio of commercial coin cells in our prototype, whose dimensions facilitate the visual observation of dendrites. The effects of pulsing on stochastic phenomena such as dendrite nucleation and growth are quantified for the first time on the basis of statistical averages of observed dendrite length distributions. We also present novel coarse-grained Monte Carlo model calculations that, by dealing explicitly with Li^+ migration in time-dependent nonuniform electric fields, provide valuable insights into the underlying phenomena. We believe our findings could motivate the design of safer charging protocols for commercial batteries.

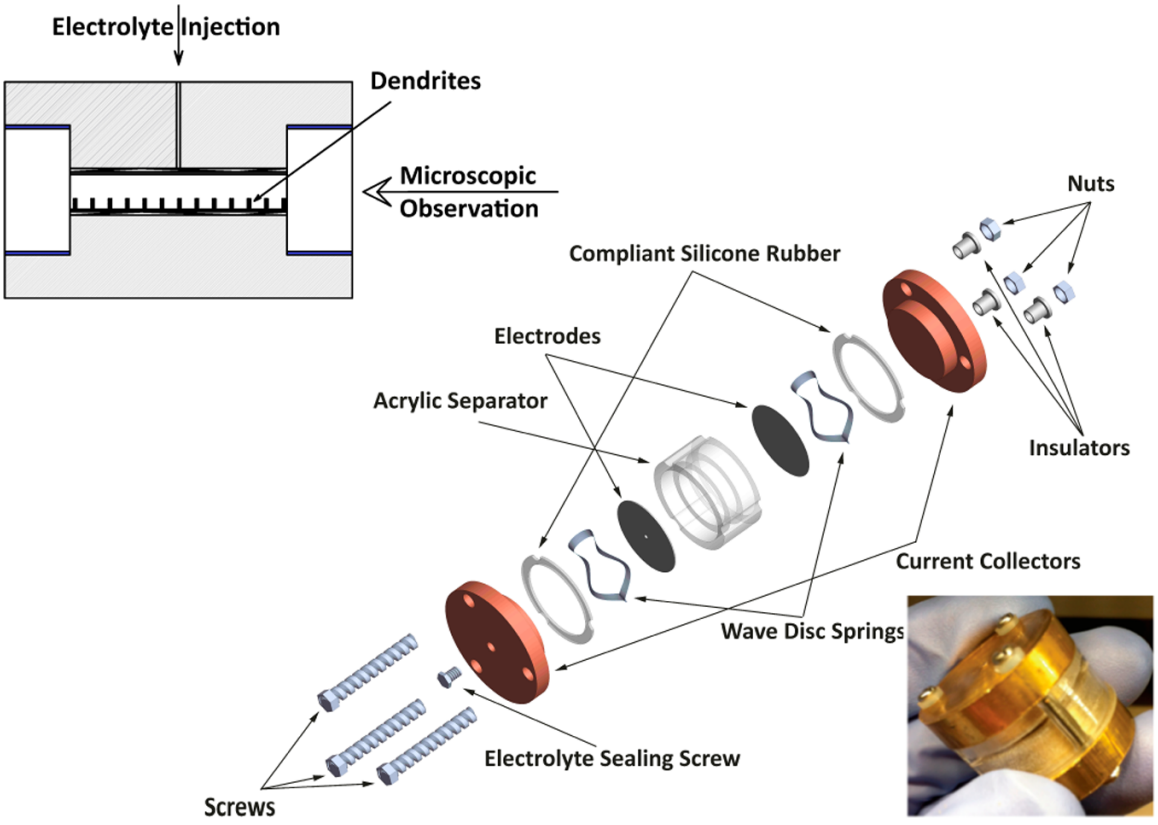

Figure 2.2: Top to bottom: cross section, exploded view, and physical appearance of the cell.

2.3 Experiments

We performed our experiments in a manually fabricated electrolytic cell that provides for *in situ* observation of the dendrites grown on the perimeter of the electrodes at any state of charge (Fig. 2.2). The cell consists of two Li^0 disc electrodes separated by a transparent acrylic separator. The cell was filled with 0.4 cm^3 of 1M $LiClO_4$ in propylene carbonate (PC) as electrolyte.

The cell separator was crafted from an acrylic plate by means of universal ILS9 laser cutter and interelectrode distance was precision-machined to 1/8". Current collectors were machined from copper rod alloy 110 (d=1") with protrusion of compatible with separator depression for an effective sealing. Ring gaskets (ID=9/16" , OD=5/8") were chopped out from silicone rubber sheet (McMaster-Carr, Plain Back, thickness=0.02").

Lithium foil (Aldrich, 99.9% on trace metal basis) 0.38 mm thick was punched (d=5/8") to be used as electrode. The counter lithium electrode and corresponding current collector were punched and threaded respectively (d=1/32") in the middle for later electrolyte injection. Lithium oxide layers were scraped out via a sharp blade and Dimethoxyethane (DME). The clean electrodes were flattened by being rolled via a glass tube. Both electrodes were intercalated in the separator. Wave disc springs (McMaster-Carr, high-carbon steel, ID=0.413" , OD=0.622", thickness=0.006") were planted after electrodes to compensate for unpredicted gap. Silicone rubber rings were laid between current collectors and the separator to provide airtight sealing. All cell components were washed with deionized water and isopropyl alcohol and dried under vacuum at 60^0C for 48 hours and then transferred to an argon-filled glovebox (H_2O , $O_2 \leq 0.5$ ppm). The components were sandwiched with insulated screws.

$LiClO_4$ (Aldrich, battery grade, 99.99% trace metal basis) was dried for 24 hours in a vacuum oven at 100^0C and dissolved in PC (Aldrich, 99.7% Anhydrous), and 1M $LiClO_4$/PC was synthesized through stoichiometric mixing to be used as an electrolyte. The electrolyte was injected into the cell afterwards and the hole was plugged through a small screw lined with Teflon tape.

The demo cell was fabricated with representative electrodes and electrolyte and was cycled with the rate of 1 mA.cm^{-2} and C/5 (τ_{cycle}= 10 hrs), for 400 cycles inside the glovebox and for the most of the period, the stable voltage regime was recorded without drying out the electrolyte. The negligible voltage and current variations are attributed to lithium electrode surface reorganization to different morphologies measurement noises in the lab. Multiples cells were fabricated and subsequently charged with Bio-logic instruments (SP-50, VSP) and Neware battery tester (BTS-5V10mA, Shenzhen, China). The cells were flushed in perimeter via isopropyl alcohol after each experiment for dendrite measurements.

The pulse charging frequency f is defined as:

$$f = \frac{1}{t_{ON}} \tag{2.1}$$

And the idle ratio γ is expressed as:

$$\gamma = \frac{t_{OFF}}{t_{ON}} \tag{2.2}$$

Arrays of multiple such cells were simultaneously electrolyzed with trains of 2 mA.cm^{-2} pulses of variable t$_{ON}$ durations and idle ratios generated by a programmable multichannel charger. After the passage of 48 mAh (173 C) through the cells, we measured the lengths of 45 equidistant dendrites grown on the cells perimeters by means of Leica M205FA optical microscope through the acrylic separator. Because dendrites propagate unimpeded in our device, that is, in the absence of a porous separator, our experiments are conducted under conditions for controlling dendrite propagation that are more adverse than those in actual commercial cells. The multiplicities and lengths [n$_i$,λ_i] of the 45 dendrites were measured in a series of experiments performed at t$_{ON}$=$\{$1,20$\}$ms , $\gamma = \{0$ (DC),1,2,3$\}$. Dendrite lengths typically spanned the 200 μm to 3000 μm range. Their average length $\bar{\lambda}$ defined by Eq. 2.3.

$$\bar{\lambda} = \frac{\int n_i \lambda_i}{L \int n_i} \tag{2.3}$$

which represents a Figure of merit for appraising the effect of pulsing on the outcome of stochastic processes, and is normalized to the inter-electrode distance L. The resulting $\bar{\lambda}$ values are shown as blue bars as functions of γ for t$_{ON}$ = $\{1, 20\}$ ms pulses in Fig. 2.3.

2.4 Modeling Framework

We have developed a model for lithium dendrite growth containing the fundamentals and main mechanisms involved in ionic transport. The electrochemical potential variation is the main drive for ionic movements and is defined by Eq. 2.4. [34] The convection is typically negligible due to thin cell geometry. [22]

$$\bar{\mu} = \mu_0 + RTln(a) + zF\phi \tag{2.4}$$

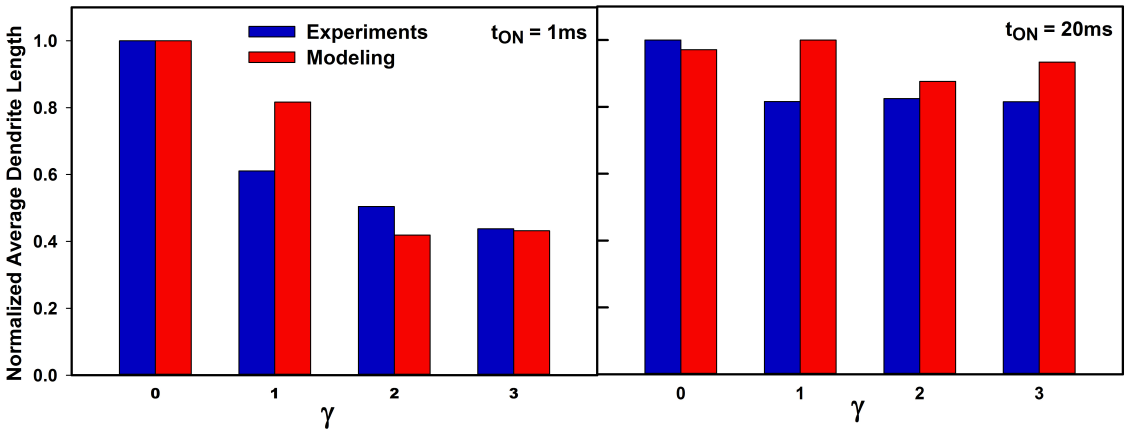

Figure 2.3: Pulse charging effect $\{t_{ON}, \gamma\}$ on dendrite measure $\bar{\lambda}$.

and the ionic flux comes from Eq. 2.5:

$$W = -\frac{CD}{RT}\nabla\bar{\mu} \approx -D\nabla C - \frac{zF}{RT}DC\nabla\phi \tag{2.5}$$

Eq. 2.5 proves that the two most important effect on ionic flux are *concentration* and *potential* variations. Dendrites contain at least hundreds of Li^0 atoms while the interionic interactions occur in the order of picoseconds. In order to make it computationally affordable, we have developed a Coarse-Grain Monte Carlo (CG-MC) model that deals explicitly with averages of displacements due to diffusion and electromigration in bigger time-scales. The model consists of a square domain with a cathode on the top and an anode in the bottom. We have assumed periodic boundary conditions (PBC) in the x direction and solid boundaries at $y = 0$ and $y = l$. Let the position of each Li^+ at time t and $(t + \Delta t)$ be $\vec{r}_i(t)$ and $\vec{r}_i(t + \Delta t)$, respectively. During interval Δt, Li^+ ions will perform random walks due to collisions with the solvent and/or migration under the applied electric field. Assuming that Li^+ ions reach stationary velocities instantaneously, we obtain Eq. 2.6.

$$\vec{r}_i(t + \Delta t) - \vec{r}_i(t) = \sqrt{2D_+\Delta t}\vec{\mathbf{g}} + \mu_+\vec{\mathbf{E}}\Delta t \tag{2.6}$$

where D_+ is the diffusion coefficient of ions for the electrolyte solution and μ_+ is their mobility, which can be obtained from Einstein relation in Eq. 2.7. [34]

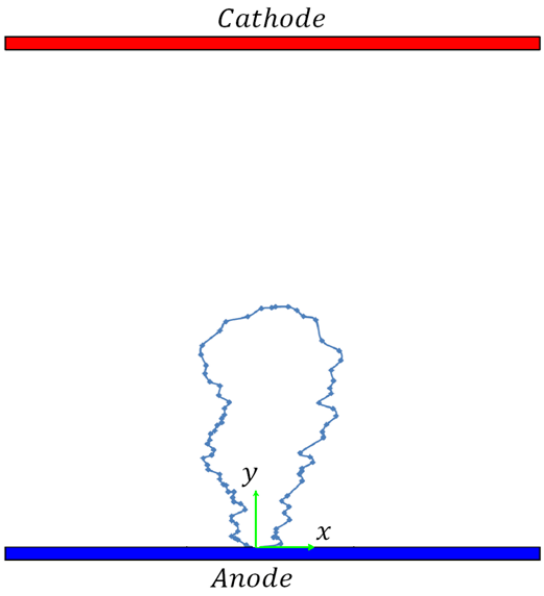

Figure 2.4: Schematic model representation.

$$\mu_+ = \frac{D_+}{k_B T} \tag{2.7}$$

The first and second terms in the RHS of Eq. 2.6 are the mean displacements due to ionic diffusion and electromigration, respectively. $\vec{\mathbf{g}}$ is a normalized 2D vector representing random motion via diffusion, Δt is the computational time interval, and $\vec{\mathbf{E}}$ is the electric field vector. Dendrite length is λ_i(t) was evaluated as their height $\bar{\lambda}_i$(t) above the surface of the electrode.

$$\lambda_i(t) = max_{k=1:n}\vec{\zeta_k}(t).\hat{\mathbf{j}} \tag{2.8}$$

where $\hat{\mathbf{j}}$ is the unit vector normal to the surface of the electrode, $\vec{\zeta_k}$ is the position of each individual atom in the dendrite and n is the total number of lithium atoms incorporated into the dendrite.

By neglecting electrostatic ion-ion interactions, given that they are effectively screened because $\lambda_D = 0.27$ nm is smaller than the average interionic separation $R_{i,j}$ = 1.2 nm, $\vec{\mathbf{E}}$(x, y, t) is computed using Laplace's Eq.:

$$\frac{\partial^2\phi}{\partial x^2} + \frac{\partial^2\phi}{\partial y^2} = -\frac{\rho}{\epsilon} \approx 0 \tag{2.9}$$

It is obvious that this approximation prevents our model from accounting for charge polarization, that is, the partial segregation of anions from cations under applied fields. Thus, in our calculations the electric field is instantaneously determined by the evolving geometry of the equipotential dendritic anode. Note that the concentration gradients that develop in actual depleted boundary layers would lead to even greater electric field enhancements than reported herein. We were forced to adopt the approximation implicit in Eq. 2.9 because the inclusion of ion-ion interactions and charge imbalances would be forbiddingly onerous in calculations based on MC algorithms. We consider, however, that the inclusion of a variable electric field represents a significant advance over previous models.[17]

When a Li^+ ion comes within d_{att} of a Li^0 on the surface or dendrite, it attaches to the structure at the bonding distance 2.38 Å. At the end of each timestep, if the electrode is on and a Li^+ ion comes within 2.38 Å of a Li^0 on the dendrite surface, it attempts to attach to the structure. The Li^+ ion selects a neighboring surface Li^0 ion and is moved perpendicularly away to a distance of 2.38 Å. If there are multiple neighboring Li^0 atoms within a distance of 2.38 Å, one is selected at random. The above procedure is repeated up to 50 times until the Li^+ ion has exactly one neighboring Li^0 at a distance of 2.38 Å. The Li^+ ion is then deposited onto the structure as a Li^0 ion. In the rare case where the Li^+ still has multiple neighbors after 50 iterations, it is returned to its position one timestep before it approached the Li^0. If an ion deposits as lithium atom, the potential field is recalculated based on new boundary condition.

The simulation is stopped and measurements are made either when 600 lithium ions are deposited or when the dendrite grows within 2.38 Å of the upper electrode. The former stopping condition is used in 98% of simulations, typically after 90% or more of the ions were deposited. To maintain a constant number of Li^+, every time a Li^+ is annihilated as Li^0 at the dendritic sites and lithium electrode surface, another

lithium ion is added a random x coordinate at the top of the domain. Also periodic boundary conditions (PBC) were assumed in the x direction. i.e., every Li^+ exiting the domain from right/left boundaries, enters from the opposite side.

Although the experiments were done in galvanostatic condition, a stable voltage has been observed. To determine the electric field we applied a constant voltage boundary condition for the anode at $y = 0$ and the anode at $y = L$:

$$\phi_{anode} = 0 \tag{2.10}$$

$$\phi_{cathode} = V_+ \tag{2.11}$$

When the electrode is off, the boundary condition becomes:

$$\phi_{anode} = \phi_{cathode} = 0 \tag{2.12}$$

Thus, there is no electrostatic field in the cell domain. The Li^+ deposition is allowed while the electrode is on, as there is an overpotential, and not while the electrode is off. We define the dendrite equipotential surface as points within a distance $r_s = 1.55$ Å of Li^0 attached to the electrode. Since the lithium dendrite is conductive and connected to the anode, we have:

$$\phi_{dendrite} = \phi_{anode} \tag{2.13}$$

As discussed in the text, we assume that implicit counterions screen out cation-cation interactions. Eq. 2.9 was solved numerically using a finite difference method using a 167×167 grid by iterating the following Eq. in 2D: [35]

$$\phi_{i,j} = \frac{1}{4}(\phi_{i+1,j} + \phi_{i-1,j} + \phi_{i,j+1} + \phi_{i,j-1}) \tag{2.14}$$

Pseudocode 1: Finite Difference method for electric field.

1. Set initial value for potential as $\phi_{i,j} = \phi_{anode} + (\phi_{cathode} - \phi_{anode}).\frac{i}{m}$.

2. Set *threshold*

3. **LOOP**

4. $\zeta = \phi$

5. $\phi_{dendrite} = \phi_{anode}$.

6. $\phi_{bottom} = \phi_{anode} \quad , \quad \phi_{top} = \phi_{cathode}$

7. $\phi_{i,j} = \frac{1}{4}(\phi_{i+1,j} + \phi_{i-1,j} + \phi_{i,j+1} + \phi_{i,j-1})$

8. Err=$|\phi - \zeta| \leq$ *threshold*? yes $\rightarrow$ **Exit Loop**, no: $\rightarrow$ **Repeat Loop**

9. $E_{i,j} = -\frac{\phi_{i+1,j} - \phi_{i-1,j}}{\Delta x}\hat{\mathbf{i}} - \frac{\phi_{i,j+1} - \phi_{i,j-1}}{\Delta y}\hat{\mathbf{j}}$

When a Li^+ ion was deposited, 50 iterations of Eq. 4.10 were performed, which was empirically shown to have good convergence. The electrostatic field was calculated numerically as:

$$E_{i,j} = -\frac{\phi_{i+1,j} - \phi_{i-1,j}}{\Delta x}\hat{\mathbf{i}} - \frac{\phi_{i,j+1} - \phi_{i,j-1}}{\Delta y}\hat{\mathbf{j}} \tag{2.15}$$

As expected, it was observed that the large electrostatic field occurs at the dendrite tip and is a major contributor to dendrite dendrite growth [36]. It should be emphasized that our model is more realistic than those previously reported[17] because it takes into account the important fact that dendritic growth is critically dependent on the strong electric fields that develop about the dendrites tips upon charging.[37] The key role of electro-migration in dendrite propagation has been dramatically demonstrated by the smooth Li^0 anode surfaces produced in the presence of low concentrations of non-reducible cations, such as Cs^+, that, by preferentially accumulating on dendrite tips, neutralize local electric fields and deflect Li^+ toward the flat anode regions.[11] Given the typically small overpotentials for metal ion reduction on metallic electrodes,[34] we consider that the effect of the applied external voltage on dendrite growth operates via the enhancement of Li^+ migration rather than accelerating Li^+ reduction. In other words, the population of electroactive Li^+

species within the partially depleted double layers surrounding the anode should be established by the competition of ion diffusion versus electromigration rather than Li^+ deposition. Furthermore, note that in our model dendrite nucleation is a purely statistical phenomenon, that is, nucleation occurs spontaneously because there is a finite probability that two or more Li^+ ions are successively reduced at a given spot on the anode surface. Once a dendrite appears, a powerful positive feedback mechanism sets in. The enhanced electric field at the tip of the sharp dendrites draws in Li^+ ions faster, thereby accelerating dendrite growth/propagation and depleting the solution of Li^+ in its vicinity. The concentration gradients observed nearby growing dendrites are therefore deemed a consequence of the onset of dendrites. In our view, simultaneity does not imply causality,[38, 39] that is, we consider that Li^+ depletion around dendrites is more of an effect rather than the cause of dendrite nucleation. Note, however, that experimentally indistinguishable mechanisms of dendrite nucleation are compatible with our interpretation that the effects of pulsing on dendrite propagation arise from the competition between ion diffusion and electromigration. Because of the computational cost of atomistic modeling, we simulate processes in a 2D domain that is smaller than the section of the actual cell. We chose its dimensions ($L^* \times L^* = 16.7nm \times 16.7nm$, Table 2.1) to exceed the depth of actual depletion boundary layers at the anode. Because our calculations aim at reproducing the frequency response of our experiments, simulation time was set to real time. Therefore, to constrain within our domain the diffusional displacements occurring in real time, we used an appropriately scaled diffusion coefficient D_+^*. The adopted D_+^*= 1.4 × 10^{-10} cm^2/s = 5.6 × 10^5 D_+ value leads to $MSD^* \approx 0.3$ L^* after 1 ms. The Eq. 2.7 ensures that this choice sets the scaled mobility at $\mu_+^* = D_+^*$ (F/RT) = 5.6 × 10^{-9} cm^2/Vs.

Pseudocode 2: Dendrite Evolution:

1. **Set**: initial electrode atoms, number of free ions, physical constants.
2. EM Dis.=$\mu\vec{\mathbf{E}}\Delta t$ & Diff. Dis.= $\sqrt{2D\Delta t}$.

Table 2.1: Parameters used in Monte Carlo Calculations

Domain size L	16.7nm × 16.7 nm
Δ t (integration step)	1 μs
$V_{cathode}$	0V
V_{anode}	85 mV
D_+ (Li^+ diffusion coefficient)	1.4×10^{-10} cm^2/s
μ_+ (Li^+ mobility)	5.6×10^{-9} $cm^2/V.s$
Li^+ radius	1.2 Å
free Li^+ ions	50
maximum Li^0 atoms	600

3. x_i=rand(H), y_i=rand(L)

4. if $r_{i,dend} < 2.38\mathring{A} \rightarrow r_{i,dend} < 2.38$ & $atom_i \rightarrow$ dendrite.

5. **LOOP 1**: Compute $\vec{\mathbf{E}}$ from Pseudocode 1.

6. **LOOP 2**:$\Delta r_i = \sqrt{2D\Delta t} + \mu\vec{\mathbf{E}}\Delta t$

7. If $r_{i,j} \leq 2.38\mathring{A} \rightarrow$ Cancel the event.

8. If $x_i > H \rightarrow x_i = x_i - H$, If $x_i < H \rightarrow x_i = x_i + H$

9. If $y_i < 0 \rightarrow$ Attach to nearest dendrite atom , If $y_i > L \rightarrow y_i = y_i - L$

10. If $r_{i,dendrite} \leq 2.38\mathring{A} \rightarrow$ {$r_{i,dendrite}$= 2.38Å & Insert 1 free ion at y=L} → **Repeat Loop 2.**

11. max(y_i) ≥ L ? yes: **Exit**, no: **Repeat Loop 1.**

Then in order to have $EMD^*=\mu_+^*|E|^*$ t ∼ MSD^*, the scaled electric field must be $|E|^* = (V_{anode}\text{-}V_{cathode})^*/MSD^* = |E|_0/5.6 \times 10^{-5} = 1.7 \times 10^5$ V cm^{-1}, from which we obtain $(V_{anode}\text{-}V_{cathode})^*= MSD^* \times 1.7 \times 10^5$ V cm^{-1} = 85 mV. The 2D Monte-Cerlo algorithm implemented on this basis calculates the trajectories of individual Li^+ ions via random diffusion and electromigration under time and position dependent electric field $\vec{\mathbf{E}}$ (x,y,t).

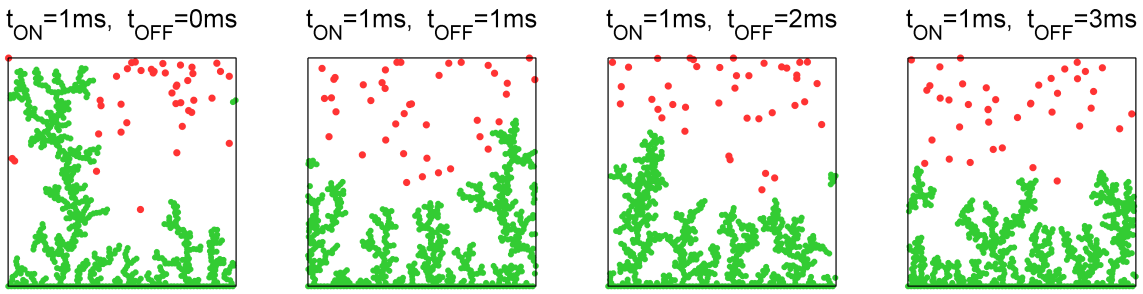

Figure 2.5: Left to right: dendrite morphologies for charging with $t_{ON} = 1ms$ pulses at $\gamma = \{0(DC), 1, 2, 3\}$. Li^0, Li^+.

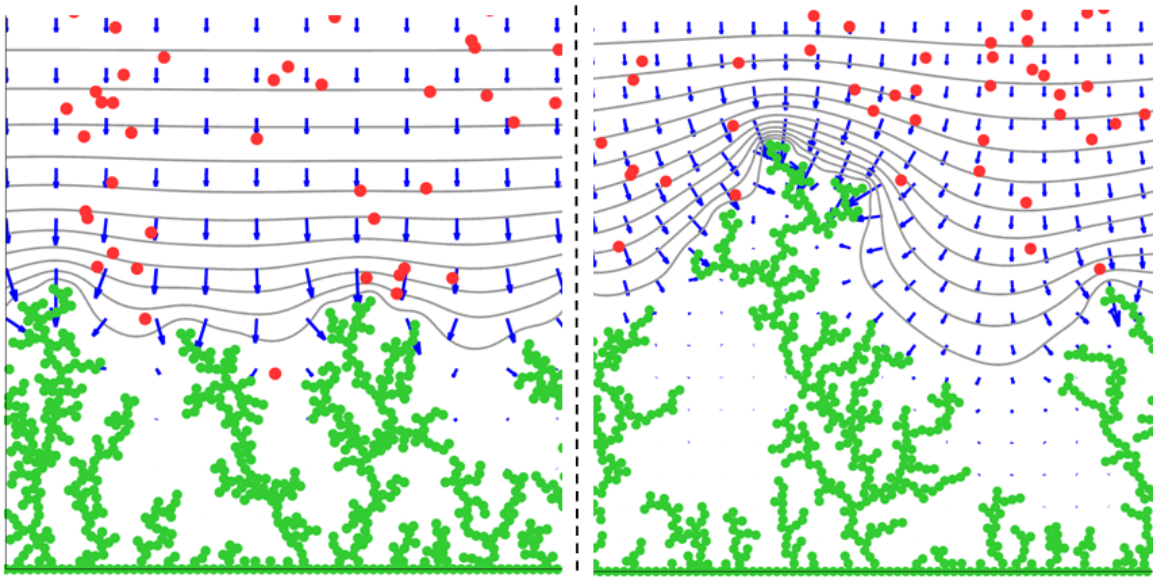

Figure 2.6: Simulations for charging with $t_{ON} = 1ms$ (left) and $t_{ON} = 20ms$ (right) at $\gamma = 3$. Li^0, Li^+, ϕ, $\vec{\mathbf{E}}$

.

These phenomena are visualized from the computational results shown in Fig.s 2.5,2.6,2.7, and 2.8. Calculations for longer t_{OFF} values show marginal improvements because $\partial[Li^+]/\partial\hat{\mathbf{n}}$ gradients ($\hat{\mathbf{n}}$ is normal unit vector to dendrite surface) remain largely unaffected in simulations for $\gamma > 3$. Fig. 2.7 shows typical morphologies of dendrites consisting of a given number of deposited Li^0.

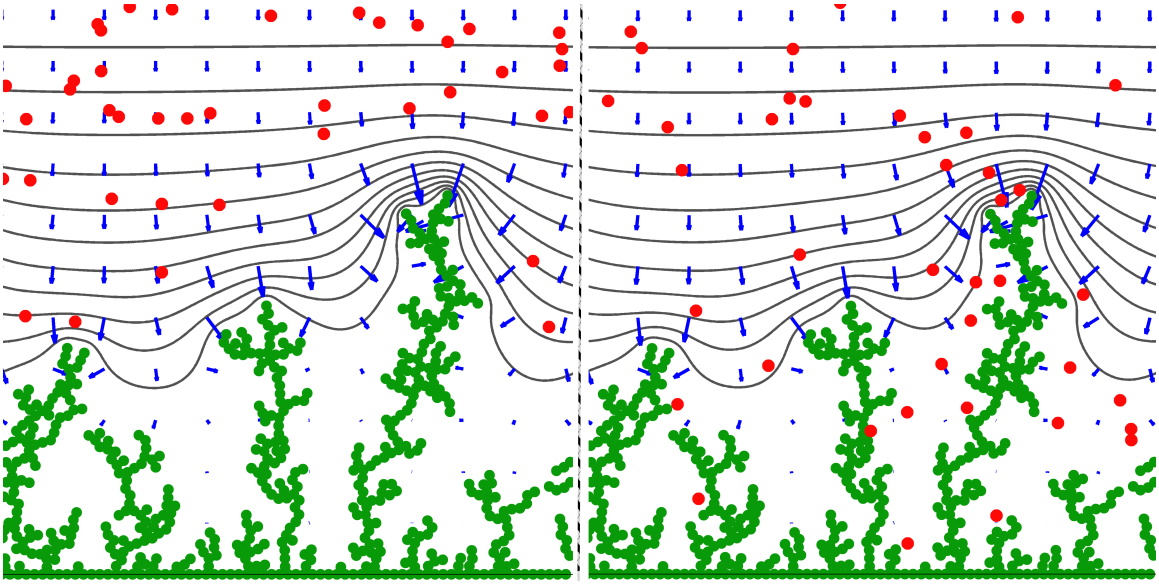

Figure 2.7: Simulations for charging with $t_{ON} = 1ms$, $\gamma = 1$ pulses. Left: after a charging pulse. Right: at the end of the successive rest period (right). Li^0, Li^+, ϕ, $\vec{\mathbf{E}}$.

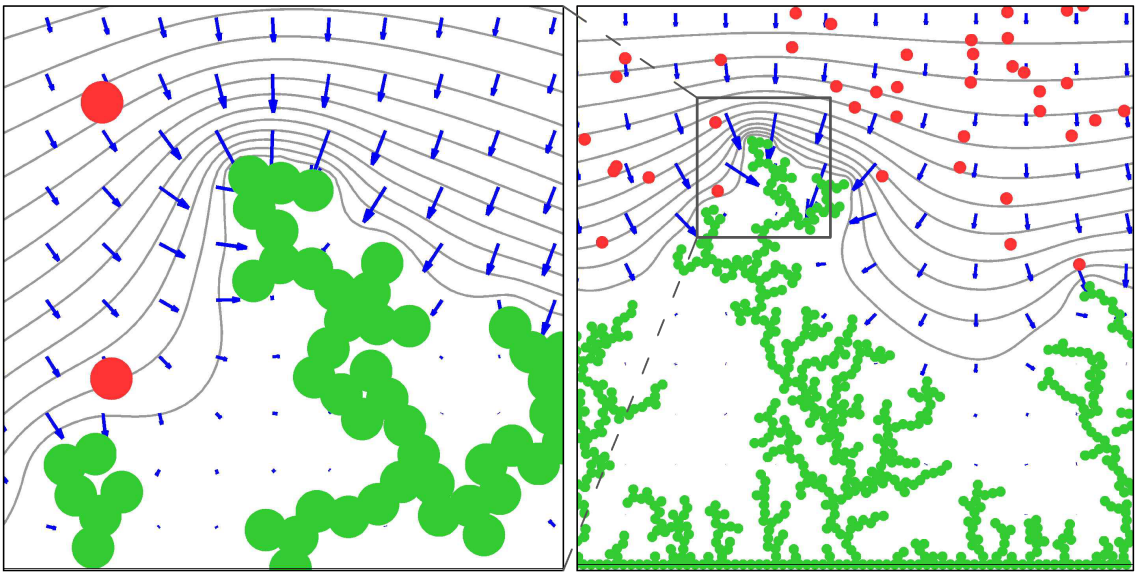

Figure 2.8: Zooming in the tip of the leading dendrite produced by charging with $t_{ON} = 20ms$, $\gamma = 3$ pulses after 243 ms (end of simulation time). Li^0, Li^+, ϕ, $\vec{\mathbf{E}}$.

2.5 Results & Discussion

It is apparent that the application of $[t_{ON} = 1ms; t_{OFF} = 3ms]$ pulse trains reduces average dendrite lengths by $\sim$ 2.4 times relative to DC charging, whereas $t_{ON} = 20ms$ pulses are rather ineffective almost at any γ. Hence, shorter t_{ON} pulses are beneficial for inhibiting dendrite propagation but are bound by the condition $t_{ON} \geq \tau_c$ (Eq. 2.17). The underlying reason is that shorter t_{ON} pulses inhibit dendrites at earlier propagation stages where the curvatures of most dendrite tips have not reached the magnitude at which local electric fields would lead to the $EMD > MSD$ runaway condition. Notice that the stage at which dendrite propagation can be controlled by pulsing relates to the curvature of tip dendrites, which is a morphological condition independent of current density. Higher current densities, however, will shorten the induction periods preceding dendrite nucleation.[40]

Calculated dendrite heights were quantified by dividing the x axis (parallel to the surface of the anode) in four sectors. Here, *dendrite height* in each sector is the height of the Li^0 atoms furthest from the electrode. To ensure good statistics, each simulation was run 100 times, for a total of 400 measurements per data point. The key experimental result, that is, that longer t_{OFF} rest periods are significantly more effective in reducing $\bar{\lambda}$ after $t_{ON} = 1$ ms than $t_{ON} = 20$ ms charging pulses, is clearly confirmed by calculations (Fig. 2.5). Metallic dendrites grow with random morphologies into equipotential structures held at $V = V_-$, thereby perturbing the uniform electric field prevailing at the beginning of the experiments. The high-curvature dendrite tips act as powerful attractors for the electric vector field, which by accelerating Li^+ toward their surfaces depletes the electrolyte self-enhances its intensity. This positive feedback mechanism has its counterpart in the electrolyte regions engulfed by dendrites because, by being surrounded with equipotential surfaces, Gauss's theorem ensures that the electric fields will nearly vanish therein.[34] It should be emphasized that the key feature is that ion displacements from electromigration are proportional to t_{ON}, whereas diffusive displacements increase as $\sqrt{t_{ON}}$. Above some critical t_{ON} value, the depth of the deplete layers will increase to the point at which they could

not be replenished during the rest periods of the same order.

Basic arguments help clarify the physical meaning of the $t_{ON} \approx$ 1ms time scale. The mean diffusive displacement (MSD) of Li^+ ions, MSD = $\sqrt{2D_+\Delta t}$ (where D_+ is the experimental diffusion coefficient of Li^+ in PC), defines the average thickness of the depletion layers created (via Faradaic reduction of Li^+ at the anode) that could be replenished by diffusion during rest periods t_{OFF}.[22] Notice that MSD is a function of time$^{1/2}$ and depends on a property of the system (D_+), that is independent of operating conditions such as current density.

From Eq. 2.7 the electric fields $|E|_c$ at which Li^+ electromigration displacements, EMD=$\mu_+|E|_c\Delta$t, that would match MSD are given by Eq. 2.16:

$$|E|_c = \sqrt{\frac{2RT}{F\mu\Delta t}} \tag{2.16}$$

Thus, with 2RT/F=50 mV at , and t=1ms,we obtain $|E|_c$ =707 V.cm^{-1},which is considerably stronger than the initial field between the flat parallel electrodes: $|E|_0$=V_0/L = 9.4 V cm^{-1}. Cathode flatness and field homogeneity, however, are destroyed upon the inception of dendrites, whose sharp (i.e., large radii of curvature) tips induce strong local fields.[22, 34] Under such conditions, Li^+ will preferentially migrate to the tips of advancing dendrites rather than to flat or concave sectors of the anode surface.[21, 22, 41, 40, 42] Because the stochastic nature of dendrite propagation necessarily generates a distribution of tip curvatures, the mean field condition EMD $\geq$ MSD at specified t_{ON} values is realized by a subset of the population of dendrites. On sharper dendrites the inequality EMD $\geq$ MSD will apply at the end of t_{ON} pulses. Thus, larger $|E|_c$ values would extend the EMD $\approx$ MSD conditions to dendrites possessing sharper tips, that is, to a larger set of dendrites that could be controlled by pulsing. Note the weak $|E|_c\mu_+^{-1/2}\eta^{-1/2}$ dependence on solvent viscosity η.

From this perspective, because $|E|_c \approx t^{1/2}$ the application of longer charging pulses will increase the width of the depletion layers over a larger subset of dendrites to such an extent that such layers could not be replenished during rest periods. The preceding analysis clearly suggests that shorter t_{ON} periods could be increasingly

beneficial. *Could t_{ON} be shortened indefinitely?* No, because charging at sufficiently high frequencies will approach DC conditions. The transition from pulsed to DC charging will take place whenever t_{ON} becomes shorter than the characteristic times τ_c of the transients associated with the capacitive polarization of electrochemical double layers. This is so because under t_{ON} pulses shorter than τ_c most of the initial current will be capacitive, that is, polarization will significantly precede the onset of Faradaic interfacial electron transfer. A rule-of-thumb for estimating τ_c on "blocking" electrodes via Eq. 2.17. [43, 44, 45, 46, 47]

$$\tau_c = \frac{\lambda_D L}{D_+} \tag{2.17}$$

L the interelectrode gap, and D_+ the Li^+ diffusion coefficient. In the experiments $\tau_c \approx 3.3ms$. In eq2.17 , λ_D is the Debye screening length defined in Eq. 2.18:

$$\lambda_D = \sqrt{\frac{\epsilon k_B T}{2z^2 e^2 C_0}} \tag{2.18}$$

In our system, with $C_0 = 1$ M Li^+ solutions in PC (ϵ= 65), $D_+ = 2.58 \times 10^6$ cm^2 s^{-1}, at 298 K, λ_D= 0.27. Because the double layer capacitance must be discharged via Faradaic currents in the ensuing rest periods,[48] it is apparent that the decreasing amplitude of polarization oscillations under trains of t_{ON} pulses much shorter than $\sim \tau_c$ will gradually converge to DC charging.

2.6 Conclusions

We have demonstrated (1) that by charging our lithium metal cell with t_{ON}=1 ms, γ=t_{OFF}/t_{ON}=3 pulse trains, the average dendrite length $\bar{\lambda}$ is significantly reduced (by $\approx$ 70%) relative to DC charging and (2) that such pulses are nearly optimal for dendrite inhibition because they are commensurate with the relaxation time $\tau_c \sim$ 3ms for the diffusive charging of the electrochemical double layers in our system. Monte Carlo simulations dealing explicitly with lithium ion diffusion, electromigration in time-dependent electric fields, and deposition at the anode are able to reproduce the

experimental trends of t_{ON} on average dendrite lengths.

Chapter 3

Quantifying Dead Lithium Crystals

Aknowledgement: The main part of this chapter is published in the Physical Chemistry Chemical Physics, 2014, 16, 24965-24970.

http://pubs.rsc.org/en/content/articlepdf/2014/cp/c4cp03590a

3.1 Abstract

We quantify the effects of the duration of the charge-discharge cycling period τ on the irreversible loss of anode material in rechargeable lithium metal batteries. We have developed a unique quantification method for the amount of dead lithium crystals (*DLCs*) produced by sequences of galvanostatic charge-discharge periods of variable duration t in a coin battery of novel design. We found that the cumulative amount of dead lithium lost after 144 Coulombs circulated through the battery decreases sevenfold as τ shortens from 16 to 2 hours. We ascribe this outcome to the faster electrodissolution of the thinner dendrite necks formed in the later stages of long charging periods. This phenomenon is associated with the increased inaccessibility of the inner voids of the peripheral, late generation dendritic structures to incoming Li^+.

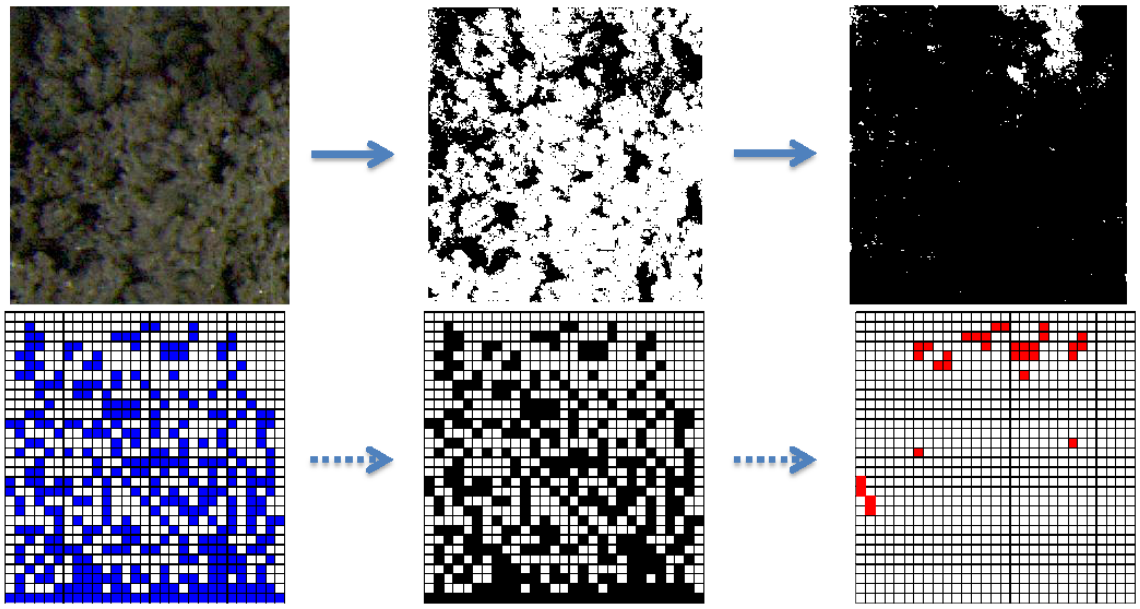

Figure 3.1: Graphical Abstract

3.2 Introduction

Intermittent renewable energy is optimally stored by electrical devices that possess the largest charge-to-weight capacity ratio (CAP) and deliver the most power (PWR).[10] The low mass density (ρ=534 kg.m^{-3}) and high redox potential (E_0 = -3.05V vs. SHE) of pure lithium (Li^0) make it the anode material of choice. Unfortunately, Li^0 also has the lowest surface energy density among anode metals. This property decreases the excess free energy of high-curvature thin necks and sharp dendrite tips, thereby favoring the growth of loosely connected microstructures.[49, 50] As a result, dendrites connected to the bulk of electrodeposits by thin necks readily re-dissolve during discharge. The breakup of such necks releases the so-called *dead lithium crystals* (DLCs). DLCs represent an irreversible loss of battery capacity.[51, 52] This drawback not only compromises the reliability but ultimately decreases the capacity of Li^0 batteries. [49, 9, 53, 54, 55, 56]

Work on dendrite growth has mainly focused on the effects of charging protocol,[8, 17] current density,[2, 7] electrode surface morphology,[57, 58] temperature,[59, 60] solvent and electrolyte chemical composition,[27, 28, 26] electrolyte concentration[25,

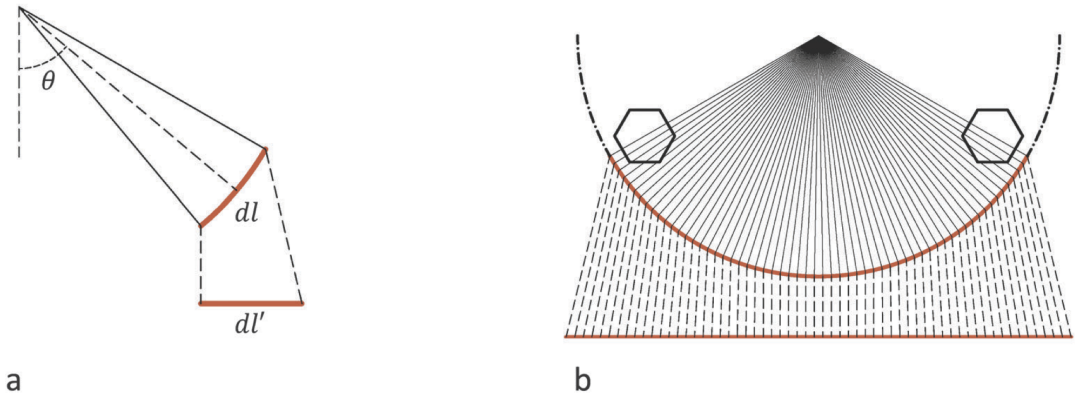

Figure 3.2: (a) Projection of curved surface elements (dl) onto flat segments (dl'). (b) Top view from 120^0 sector of the cell perimeter.

61], and evolution time[30, 20] on dendrite growth. Some strategies include the use of powder electrodes[31] and adhesive polymers.[32] The empirical nature of these approaches, however, reflects the fact that current models of dendrite growth exist based on various simplifying assumptions that have fallen short of capturing the essentials of this phenomenon.[7, 22, 62, 63, 64, 65]. We view DLC formation as a manifestation of the intrinsic sponginess of Li^0 electro-deposits,[66] and the non-uniform dissolution rates of such deposits upon discharge.[52, 67, 68]

We report experimental results on the effect of the duration of the charg-discharge period τ on the amount of DLCs produced at constant charge. DLC quantification is based on rigorous counting based on the computer analysis of the digitalized images of electrodeposits produced in scaled-up coin cells of our own design.

3.3 Experiments

We have fabricated a device specially designed to visually observe the morphology of electrodeposits[69] (Fig. 2.2). The geometric characteristics of the cell, such as the electrode surface and separation, are known to be critical for the morphology of deposits.[70] Accordingly, our device meets the boundary conditions and geometry of typical coin cells and hence provides a realistic setup for studying these phenomena. Further details can be found elsewhere.[8]

A 0.38mm thick lithium foil (Aldrich, 99.9%) was scraped to remove oxide layers by means of a sharp blade and dimethyl carbonate and then flattened by being rolled with clean glass tubes. Disc electrodes (d= 9/16") were punched from the clean foil and tightly pressed between the separator and the current collectors by means of silicone gaskets and electrically insulated screws. $LiClO_4$ (Aldrich, battery grade, 99.99%) was dried for 24 hours under vacuum at 100^0C and then dissolved in PC (Aldrich, 99.7% Anhydrous). 1M $LiClO_4$/PC solutions were used in all experiments. They were then injected into the cells, which were sealed afterwards with stoppers lined with a Teflon tape. All operations were carried out in a glovebox continuously purged with pure argon.

Four identical cells were assembled and cycled galvanostatically at the rate of $2mA.cm^{-2}$. The cycling period, τ, and the corresponding number of cycles, i.e., the total duration of charging, were adjusted such that the total circulated charge (40 mAh=144 Coulombs) was the same in all cells in each set of experiments. After the last discharge cycle, the cells, kept intact, were taken outside the glovebox and placed under a Leica 205FA microscope. High-resolution images were taken showing lateral views of the three equiangular 120^0 sectors of cell peripheries.

Since the images acquired at the focal plane of the camera correspond to those of the curve perimeters of the cell, we developed an algorithm that projects finite segments of the acquired images onto a flat surface according to Eq. 3.1:

$$dl'_i = \frac{dl_i}{cos(\theta_i)} \tag{3.1}$$

where dl'_i is the width of the projected element, dl_i is the width of the original element in the acquired image, and θ_i is the corresponding angle about the axis of the cylindrical cell (Fig. 3.2). The projected elements were assembled into the reconstructed flat images used for analysis.

3.4 Digital Quantification

The projected images were cast into 100 × 400 pixel grids. The resulting 2D matrices (one for each 120^0 sector) contain information on the hue, saturation, and brightness of each pixel in a 0 to 255 scale. Dendritic forms were distinguished from voids by establishing a grayness threshold, t_{thresh}, which classifies matrix elements into *black* (i.e., those whose illumination falls below the grayness threshold) and *white* classes. The optimal grayness threshold t_{thresh} is determined by minimizing the intra-class variance $\sigma_w^2(t)$ iteratively following Otsu's method:[71]

$$\begin{aligned} \text{Find} \quad & t_{tresh} \\ \text{to minimize} \quad & \sigma_w^2(t) \end{aligned}$$

where:

$$\sigma_w^2(t) = w_1(t)\sigma_1^2(t) + w_2(t)\sigma_2^2(t) \tag{3.2}$$

σ_w^2(t) is the weighted sum of black and white variances $\sigma_1^2(t)$ and $\sigma_2^2(t)$ with w_1(t) and w_2(t) are the corresponding weights (probabilities), respectively. Fig. 3.3 shows an original image and the corresponding binary image created by this procedure.

The area A of a given microstructure E_m is defined by Eq: 3.3:

$$A = \sum_{m=1}^{N} E_m \tag{3.3}$$

where N is the number of E_m elements contained in such a microstructure.

From A_{DLC} we evaluated the mass, m_{DLC}, and volume, V_{DLC}, of DLCs via dimensional analysis according to Eq. 3.4, which is based on the assumption that the porosity of the dendrites is homogenous throughout:

$$m_{DLC} \propto V_{DLC} \propto A_{DLC}^{3/2} \tag{3.4}$$

We distinguished two types of microstructures:

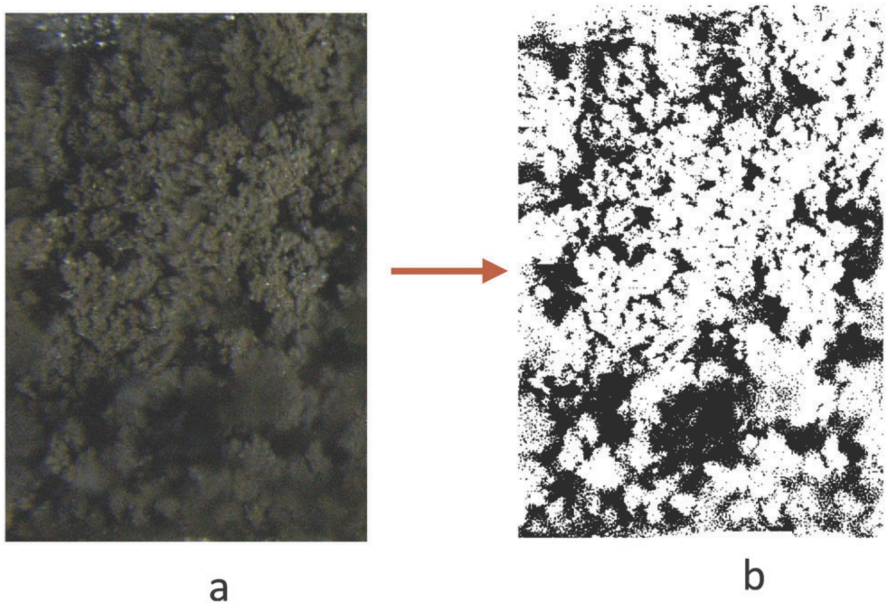

Figure 3.3: (a) The original microscopic dendrite image. (b) Binary image reconstructed by using Otsu's method.

1. Dead lithium crystals, *DLCs*, are groups of connected elements surrounded by void regions (Fig. 3.4-a).

2. Dendrites, *DNDs*, are groups of elements connected to the anode (Fig. 3.4-b).

We define Eq. 3.5 as the mass fraction ratio for DLCs f_{DLC}:

$$f_{DLC} = \left(\frac{\sum_{i=1}^{k} A_{DLC,i}}{A_{TOT}} \right)^{\frac{3}{2}} \tag{3.5}$$

k is the number of elements belonging to DLC groups of area $A_{DLC,i}$, and A_{TOT} is the total area of electrodeposited Li^0.

We also define DNDs as the measure for circulated lithium within the cells in Eq. 3.6:

$$f_{DEP} = \left(\frac{\sum_{i=1,j=1}^{M,N} Lit_{i,j}}{E_{TOT}} \right)^{\frac{3}{2}} \tag{3.6}$$

M and N run from $i, j = 1$ to $i = 100$ and $j = 400$, respectively. $Lit_{i,j}$ is 1 if the

pixel is recognized as Li^0 and 0 otherwise, and $E_{TOT} = 40000$ is the number of grid pixels.

In order to identify the connectivity of Li^0 elements to the anode we searched whether a given pixel in the 2D binary matrix is connected to the elements representing the anode surface by at least one of its 4 sides and 4 vertices by means of an iterative loop (Fig. 3.4-a and 3.4-b). Then, we search in each matrix column the upper-most of such elements, whose i-index defines the range of those belonging to the DND class. For the elements lying on the left and right borders of each image we used PBC, i.e., we assumed that the same morphology is replicated beyond the left and right borders. Fig. 3.4-c shows a sample binary image of the deposition. The identified DLCs are shown in Fig. 3.4-d.

Pseudocode 3: Recursive algorithm for Identification and counting of a DLC

1. Total=0;
2. **For** each pixel(i) {i=1:40000}
3. Total = Total + counted;
4. counted=0; [Global Variable]
5. **isdead(pixel(i))**
6. counted=counted+1;
7. **If** neighbors==0 → **Exit**(function)
8. **If** a neighbor == anode → counted=0 & **Exit**(function)
9. **Else** remove pixel(i) & **isdead(neighbors)**
10. **end**(function)
11. **end**(for)

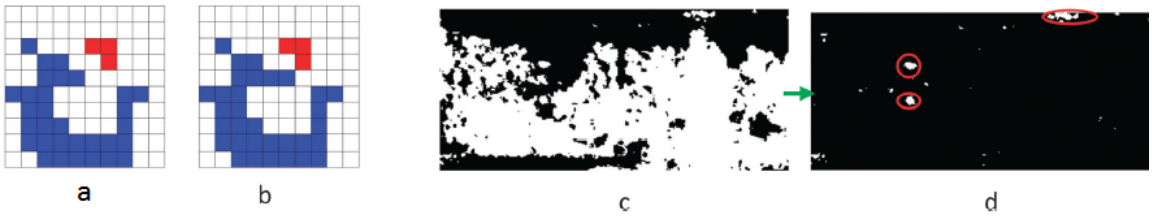

Figure 3.4: (a) Digital lattice showing a detached DLC (red). (b) Lithium dendrite (red) with connection from neighbors to deposited volume. (c) Binary image of dendritic lithium electrodeposits. (d) Identified DLCs; Largest DLCs are shown in the red enclosures.

3.5 Results & Discussion

It is apparent that the mass fraction of dead lithium crystals, f_{DLC}, which is in effect a measure of the loss of battery capacity, is directly correlated with the duration of the charging period $\tau/2$ (Fig. 3.7). The cumulative battery capacity losses were reduced sevenfold by shortening t from 16 to 2 hours after the same amount of charge (40 mAh = 144 C) circulated through the batteries in all cases. The data in Fig. 3.8 confirm that the amount of deposited Li^0 (i.e., of circulated charge) remains constant under all experimental conditions. Since DLCs are produced by severing the capillary bridges (*necks*) that linked them to the body of Li^0 electrodeposits during discharge, the results shown in Fig. 3.7 in fact reflect how the morphology and connectivity of deposits change along charging periods.[51, 67] Fig. 3.6, which is a plot of the voltage $V(t)$ required to maintain constant current i_0 during charge and discharge periods, provides revealing insights into the evolution of electrodeposits. Considering that current density i increases exponentially with overpotential η:

$$i \propto exp(\eta) = exp[V(t) - E(t)] \tag{3.7}$$

($E(t)$ is the instantaneous reduction potential of the Li^+/Li^0 couple at each stage of the charging-discharging cycles) the observed $V(t)$ variations reflect how $E(t)$ changes during charge and discharge. Departures from the value for Li^+ reduction into perfect flat Li^0 crystals ($E^0(t)$ = -3.05 V at Li^+ unitary activity) would arise when Li^+ is reduced to curved microstructures. By virtue of Kelvin's effect, dendrite curved tips

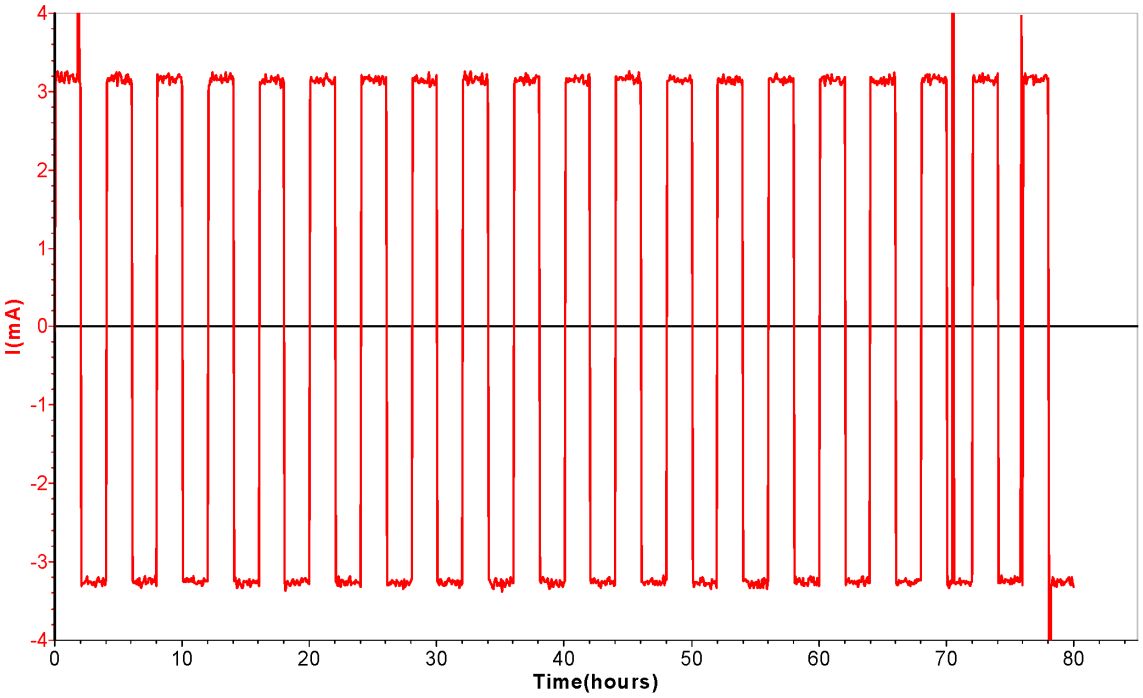

Figure 3.5: Current profile for galvanostatic cycling of symmetric Li^0 cell at the rate of C(τ=2 hrs) and $i = 2mA.cm^{-2}$.

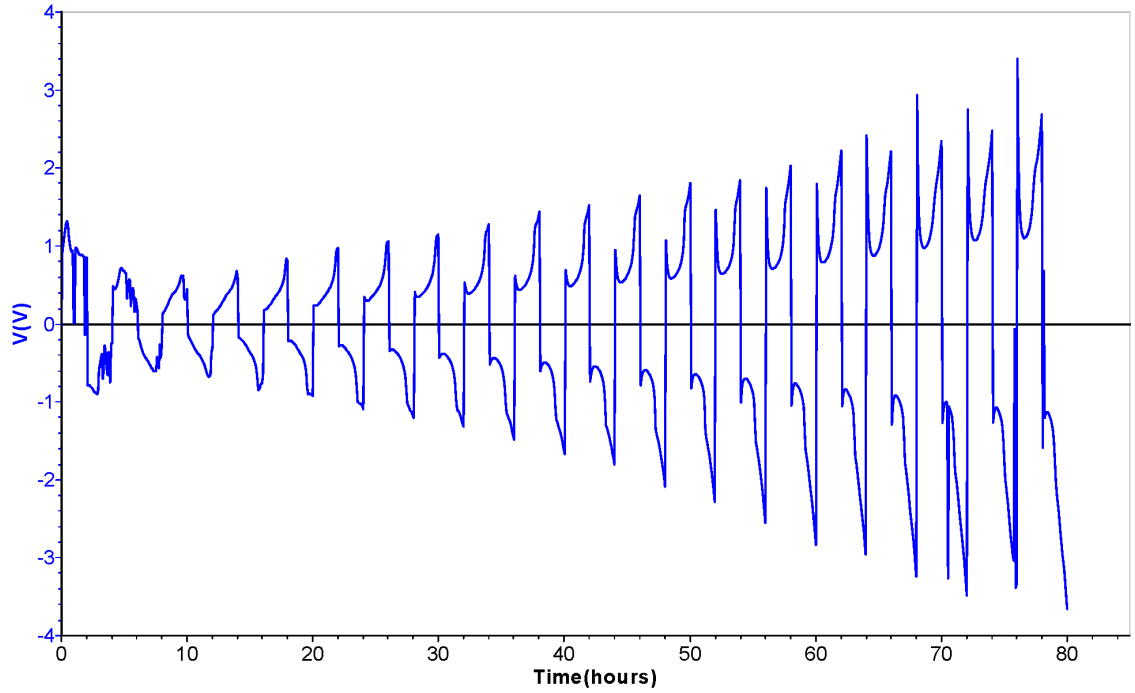

Figure 3.6: Current profile for galvanostatic cycling of symmetric Li^0 cell at the rate of C(τ=2 hrs) and $i = 2mA.cm^{-2}$.

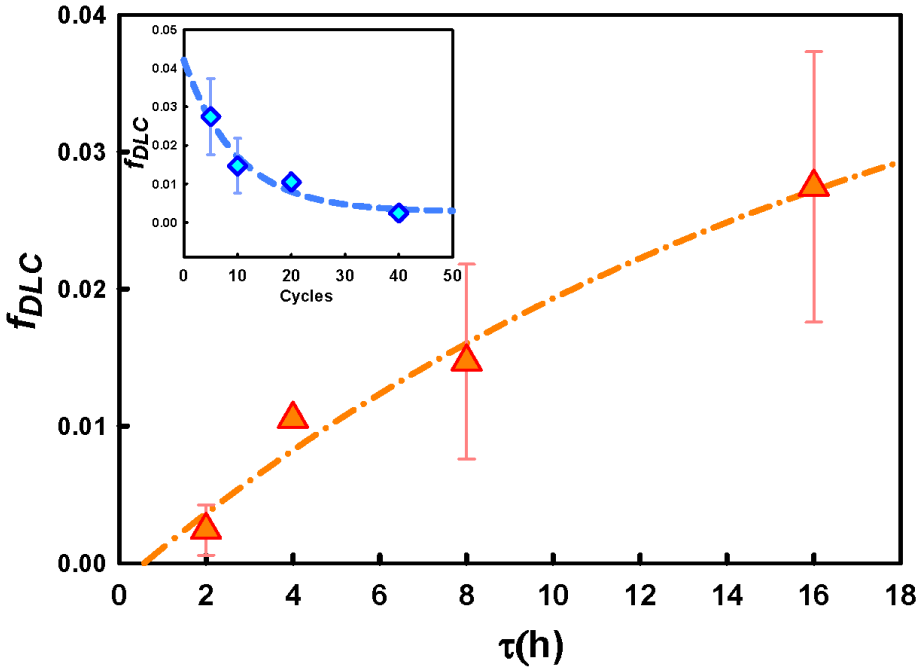

Figure 3.7: Dead lithium fraction f_{DLC} as a function of cycling period τ.

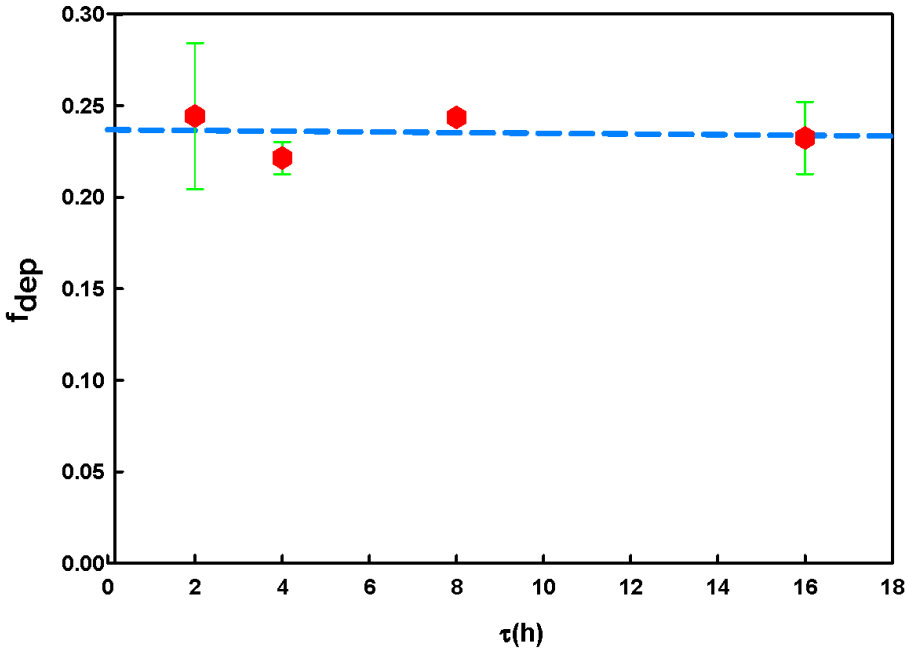

Figure 3.8: The fraction of deposited Li^0, f_{DEP} versus cycling period τ.

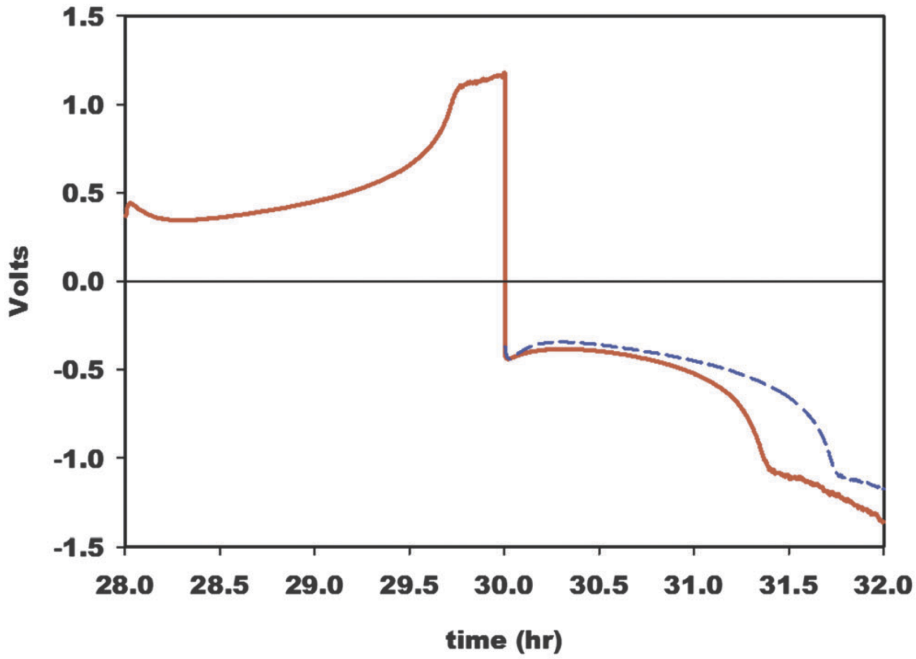

Figure 3.9: Voltage profiles of successive charge-discharge periods $V_{charge}(t)$, $V_{discharge}(t)$ (red trace). The blue trace corresponds to $-V_{charge}(\tau+2)$, which shows that the Li^0 electrodeposits requiring the highest negative overvoltages redissolve first at the lowest positive overpotentials.

have more negative reduction potentials than flatter electrode sectors:[72]

$$E(\rho) = E(\infty) + \frac{2\gamma V}{\rho} \tag{3.8}$$

where ρ is the radius of curvature, $\gamma \sim 1$ J.m^{-2} is the Li^0/electrolyte interfacial surface energy,[73, 74] and V= 1.3 $\times$ 10^{-5} m^3 mol^{-1} is the Li^0 molar volume. Thus, $V(t)$ has to become more and more negative to maintain η and hence i_0. The reverse phenomenon occurs during discharge: higher curvature structures will be the first to re-dissolve.[75] Since the experimental overpotentials in the later stages of charging and discharging cycles are actually the sum of charge transfer and diffusion overpotentials, by assuming that overall $\eta \sim 1V$ overpotentials correspond to effective $\eta \sim 0.1V$ charge transfer activation overpotentials, we deduce that Li^+ reduction takes place on structures having curvatures reaching atomic dimensions: $r \approx 10^{-9}m$. We ascribe the gradual increase of η along the sequence of charge-discharge cycles to the development of partially insulating solid-electrolyte interfaces (SEI) obtained by the decomposition

of the solvent.[28, 29, 3, 76] The preceding analysis suggests that thinner, i.e., higher curvature necks are produced in the later stages of extended charging cycles, thereby increasing the probability of DLC detachment during discharge.[52, 20, 63, 77, 78] The fact that DLCs appear preferentially at longer charging times implies that the root segments (necks) of the dendrite structures produced in later stages are thinner and/or longer.[66] Thinner and longer necks have a larger positive (convex) curvature radius, ρ_{convex}, about their cross sections, and a smaller negative (concave) curvature radius, $\rho_{concave}$, about their columns.[79] As a result, such necks having larger mean positive curvatures[75] will accumulate larger electron densities, and hence display faster Li^0 electrodissolution rates.

3.6 Conclusions

We have developed a novel method for quantification of DLCs and we have shown that the cumulative loss of battery capacity via the detachment of Li^0 particles after sequences of charge-discharge cycles amounting to the exchange of 144 Coulombs is significantly reduced by shortening the duration of the cycling period. This outcome is likely due to the faster electrodissolution of the thinner necks formed in the later stages of longer charging periods. We ascribe this phenomenon to the increased inaccessibility of the inner voids of the peripheral, late generation dendritic structures to incoming Li^+. [66]

Chapter 4

Thermal Relaxation

Acknowledgement: The main part of this chapter is published in the Physical Chemistry Chemical Physics, 2015, 17(12), 8000-8005. [80]

http://pubs.rsc.org/en/content/articlelanding/2015/cp/c4cp05786d

4.1 Abstract

The average lengths $\bar{\lambda}$ of lithium dendrites produced by charging symmetric Li^0 batteries at various temperatures are matched by Monte Carlo computations dealing both with Li^+ transport in the electrolyte and thermal relaxation of Li^0 electrodeposits. We found that experimental $\bar{\lambda}(T)$ variations cannot be solely accounted by the temperature dependence of Li^+ mobility in the solvent but require the involvement of competitive Li-atom transport from metastable dendrite tips to smoother domains over $\Delta E_R^{\ddagger} \approx$20 KJ.mol^{-1} barriers. A transition state theory analysis of Li-atom diffusion in solids yields a negative entropy of activation for the relaxation process, $\Delta S_R^{\ddagger} \approx$ - 46 J.mol^{-1}.K^{-1}, that is consistent with the transformation of amorphous into crystalline Li^0 electrodeposits. Significantly, our $\Delta E_R^{\ddagger} \approx$20 KJ.mol^{-1} value compares favorably with the activation barriers recently derived from DFT calculations for self-diffusion on Li^0 (001) and (111) crystal surfaces. Our findings underscore the key role the mobility of interfacial Li-atoms plays in determining the morphology of dendrites at temperatures T_{SR} above the onset of surface reconstruction: $T_{SR} \approx 0.65 T_{MB}$

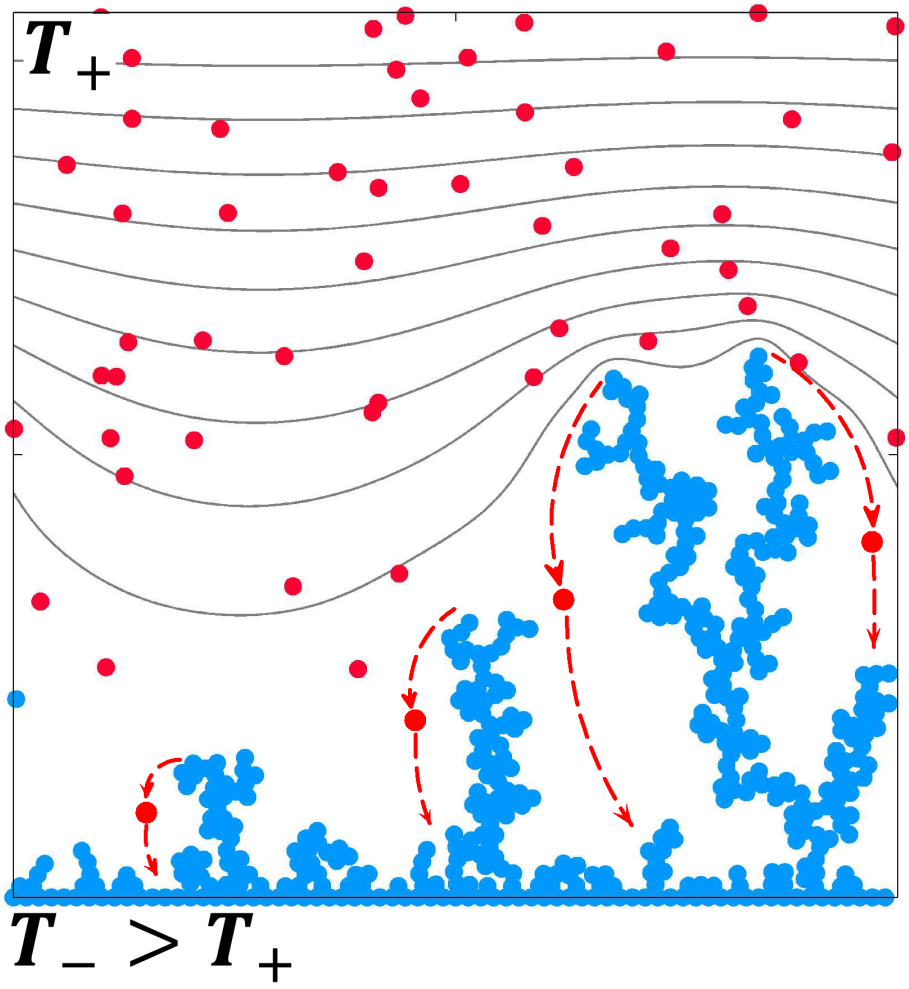

Figure 4.1: Graphical Abstract.

($T_{MB} = 453K$ is the melting point of bulk Li^0).

4.2 Introduction

Portable electronic devices and intermittent renewable energy sources demand high-capacity, reliable, long-lasting electric energy storage units.[14, 10, 81] The low mass density (ρ=0.564 g.cm^{-3}) and high reduction potential (E^0 = -3.04 V vs. SHE) of lithium metal (Li^0) should make it the ideal electrode material.[9, 82, 1, 83, 16] Li^0, however, is exceptionally prone to grow dendrites under the far from equilibrium conditions prevalent during electrodeposition.[9, 84, 85] The runaway growth of metallic dendrites is the harbinger of short-circuiting, overheating, and ultimately the ignition of the organic solvents used in Li^0 batteries.[3] Intense efforts are therefore underway to prevent such hazards by limiting dendrite growth during battery charging.[8, 63] At present, efforts aimed at controlling Li^0 dendrite growth remain semi-empirical because its mechanism is not fully understood.[72, 7, 27, 28, 26, 86, 31, 32, 23, 17, 11, 87, 58, 56, 64] Models fall short of capturing the complex dynamics of dendrite inception and growth,[7, 22, 88], or accounting for the peculiar facility of Li^0 to grow dendrites relative to other potentially useful 1st and 2nd period metals.[89, 90, 49, 13, 91, 92, 93, 94] In our view, control strategies should consider that dendrite growth is a non-deterministic stochastic process,[95, 40, 96, 21] and the propensity of Li^0 for growing dendrites is a direct consequence of the inherent Li-Li binding energy and energy barrier values for Li-atom transport on the metal surface.[97, 98] We have previously addressed the former issue via pulsed charging experiments and Monte Carlo computations.[8] Here we report experiments and computations aimed at quantify the thermal behavior of electrolytic Li^0 dendrites as a first step toward linking Li^0 properties with dendrite growth and control.[99, 100, 73]

4.3 Experiments

We charged symmetric coin Li^0 batteries that allow for *in situ* visualization of dendrites.[69, 101, 20] Disk electrodes (A = 1.6 cm^2) punched from cleaned Li^0 foil (Aldrich, 99.9%, 0.38 mm thick, were mounted L = 3.175 mm apart on an open-ended transparent polymethyl-methacrylate (PMMA) cylindrical tube separator. The electrolyte was a 1M $LiClO_4$ (Aldrich, battery grade, 99.99%, dried for 24 hours at 90^0C under vacuum) solution in PC (PC) (Aldrich, 99.7% Anhydrous). Batteries were submerged in a thermostated bath, as shown in Fig. 4.2, and charged galvanostatically at 2mA.cm^{-2} for 8 or 24 hours in a glovebox sparged with argon (H_2O, $O_2 \leq 0.5$ ppm). We estimated that:

1. Convection is negligible under present conditions.

2. Linear temperature gradients normal to the anode are established within minutes.

3. The limiting diffusional current density for Li^+ in PC is much bigger than 1mA.cm^{-2} (J ¿¿ D C_0/L = 78 mA.cm^{-2}).[102]

After charging, batteries were removed from the glovebox for the acquisition of high-resolution digital images of the electrodeposits with a Leica 205FA microscope. The digital images of the three equiangular 120^0 sectors of the curved peripheries of the cylindrical cells were then projected onto a flat surface as described in our previous publication.[94] Forty-five equidistant dendrites were selected from the projected images and sorted into $[n_i, \lambda_i]$ bins within specified length ranges λ_i. From this information we evaluated normalized average lengths,$\bar{\lambda}$, defined by Eq.2.3.

The experimental $[n_i, \lambda_i]$ distributions are shown in Fig. 4.3. Fig. 4.4 shows plots of average lengths $\bar{\lambda}$ versus anode temperature T_-.

The temperature distribution can easily be obtained from heat equation. Since the conductivity of PMMA separators is significantly lower than the copper current collectors ($\alpha_{Li,Cu} >> \alpha_{PMMA}$), we can assume that the heat within the cell flows in 1D. Hence:

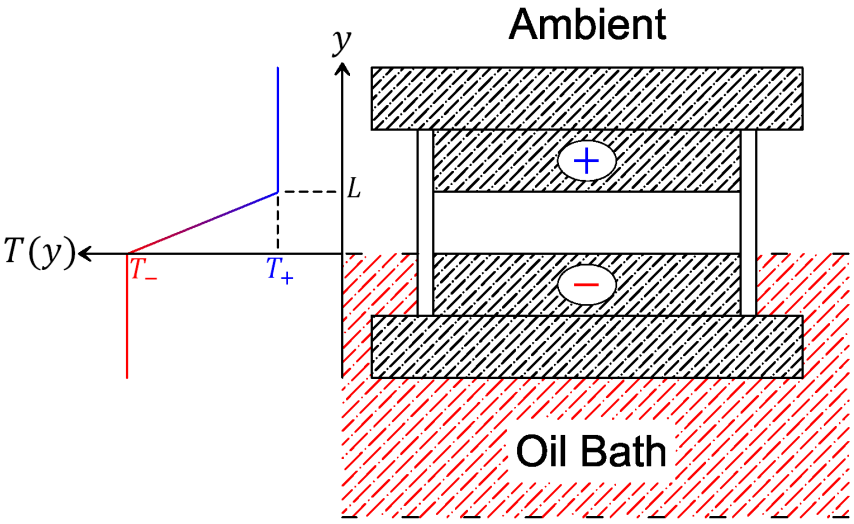

Figure 4.2: Schematic diagram of the experimental setup. The initial steady-state temperature profile is shown on the left.

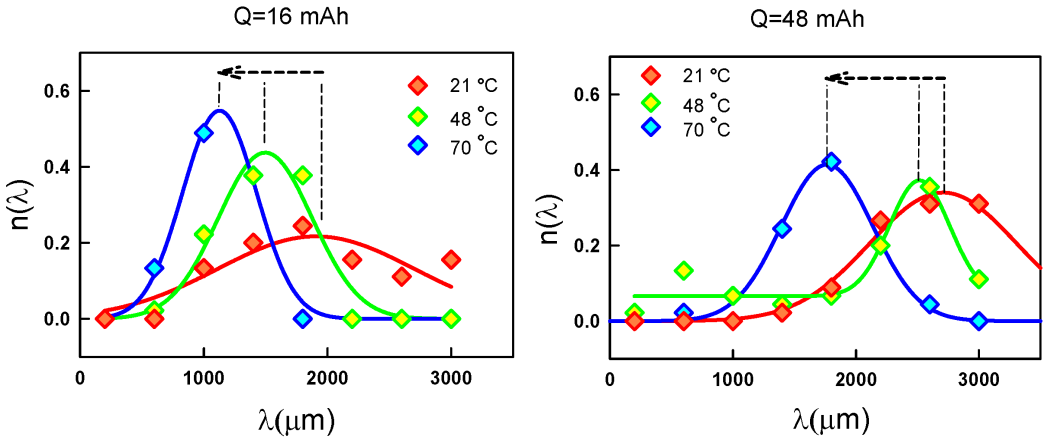

Figure 4.3: Normalized dendrite length distributions [n_i,λ_i] at various anode temperatures T_. Cells charged at 2mA.cm^{-2} for 8 hrs (left) and 24 hrs (right).

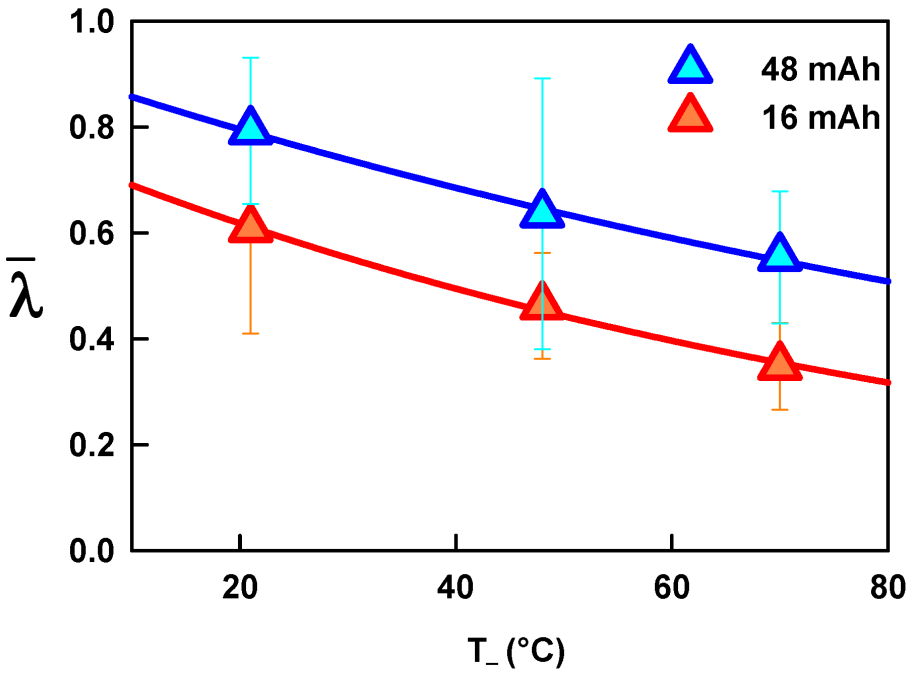

Figure 4.4: Dendrite measure $\bar{\lambda}$ variation versus anodic temperature T_.

$$\frac{\partial T}{\partial t} = \alpha \nabla^2 T \tag{4.1}$$

For quasi-steady state condition in which change in boundary condition is significantly slow, the initial temperature distribution is time independent, hence:

$$\frac{\partial^2 T}{\partial y^2} = 0 \tag{4.2}$$

and the imposed boundary conditions are:

$$\begin{cases} T(0) = T_- \\ T(L) = T_+ \end{cases} \tag{4.3}$$

Therefore we obtain linear temperature distributions from anode to cathode, which is material independent:

$$T(y) = T_- + (T_+ - T_-)\frac{y}{L} \tag{4.4}$$

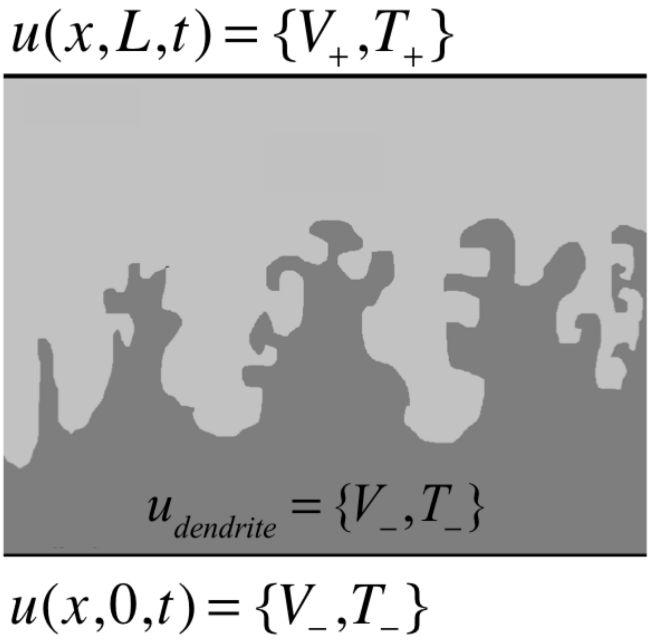

Figure 4.5: Schematic representation of model boundary conditions.

In principle, the potential field ϕ is obtained by solving Gauss's law. However, since electroneutrality is a valid approximation throughout the electrolyte, up to thin depletion boundary (i.e., ion-ion electrostatic interactions are screened out by counter ions because the Debye length ($\lambda_D = 0.27$ nm) is smaller than the average inter ionic separation ($R_{i,j}$=1.2 nm), Gauss's law reduces to Laplace's equation. Also, since the heat conductivity of metallic lithium and copper is much higher than the PMMA separator walls, we can assume that the dendrites are isothermal with the anode electrode and temperature profile is also described by Laplace's equation. Hence, we define a generic parameter u as follows:

$$u(x, y) = \{\phi(x, y), T(x, y)\} \tag{4.5}$$

where x and y are coordinates parallel and normal to the anode. Therefore:

$$\frac{\partial^2 u}{\partial x^2} + \frac{\partial^2 u}{\partial y^2} \approx 0 \tag{4.6}$$

Based on schematic representation in Fig. 4.5 we have the following imposed boundary conditions:

$$u(x,0) = \{V_-, T_-\} \tag{4.7}$$

$$u(x,L) = \{V_+, T_+\} \tag{4.8}$$

$$u_{dendrites} = u_{anode} \tag{4.9}$$

Note than the high electrical and thermal conductivities of Li^0 ensure that anodic electrodeposits are equipotential and isothermal surfaces at [V_-,T_-] at all times. To ensure a smooth surface, the equipotential surface extends slightly beyond the bonding radius of Li^0 at 1.3 r_+.

We solved Eq. 4.6 using a finite difference method in a (280 $\times$ 280) grid according to Eq. 4.10.

$$u_{i,j} = \frac{1}{4}(u_{i+1,j} + u_{i-1,j} + u_{i,j+1} + u_{i,j-1}) \tag{4.10}$$

Periodic boundary conditions (PBC) were assumed in the x direction, i.e., every Li^+ exiting the domain from right/left boundaries, enters from the opposite side. The electric field was obtained numerically as:

$$\vec{\mathbf{E}}_{i,j} = -\frac{\phi_{i+1,j} - \phi_{i-1,j}}{2\Delta x}\hat{\mathbf{i}} - \frac{\phi_{i,j+1} - \phi_{i,j-1}}{2\Delta y}\hat{\mathbf{j}} \tag{4.11}$$

Lithium has very small reduction potential, (E^+ = -3.04 V) [34], and hence we consider that the effect of the applied temperature gradient on dendrite growth operates via the enhancement of Li^+ migration rather than reduction and Li^+ would be reduced to a Li^0. Fig. 4.6 shows the distributions of normalized temperature $|T|$, defined as below:

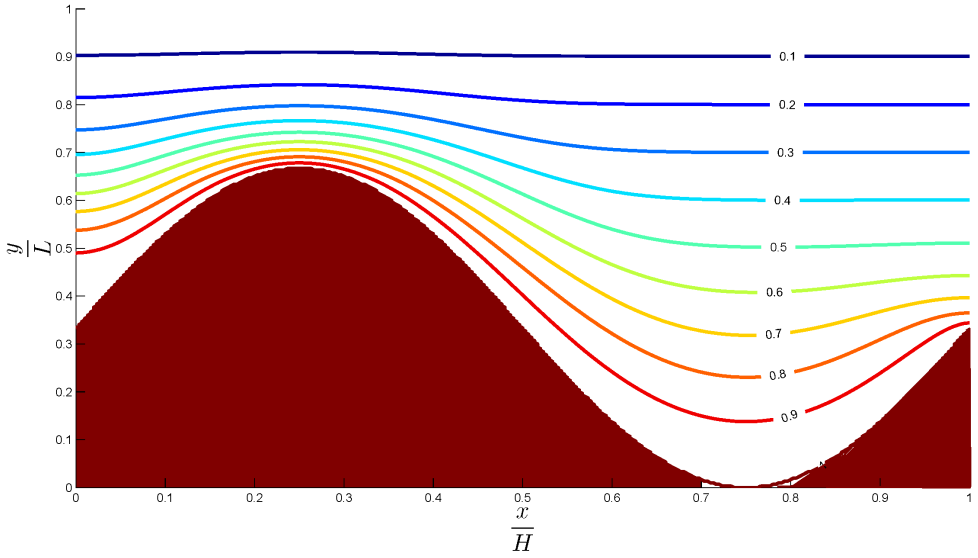

Figure 4.6: Normalized temperature $|T|$ distribution within normalized cell dimensions $[H, L]$ in the present of one convex (peak) and one concave (hollow) dendrite morphology.

$$|T| = |\frac{T - T_+}{T_- - T_+}| \leq 1 \tag{4.12}$$

within region normalized by height y/L over convex and concave regions of Li^0 electrode deposits. The concave/convex morphology has been imitated by sinusoidal function during one period and the higher curvatures have been approximated with higher *Sin* powers. Fig. 4.6 shows that the isothermal lines are closer to each other in the vicinity of convex surface (peaks) relative to the concave (hollow) regions. Fig. 4.7 shows the variation of normalized temperature with the normal distance from the dendrite surface in the convex/concave regions and their variation based on the curvature κ.

4.4 Modeling

Model calculations were based on our recently developed coarse-grained dynamical Monte Carlo (CG-MC) framework.[8] The core 2D CG-MC algorithm calculates the combined diffusional and migrational Li^+ displacements using temperature depen-

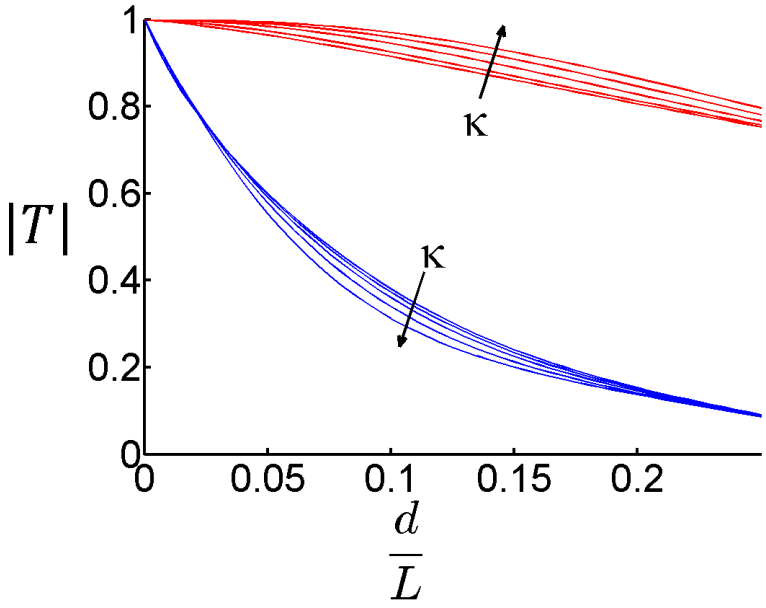

Figure 4.7: Normalized temperature $|T|$ variation versus normalized vertical distance $\frac{d}{L}$ for convex (blue traces) and concave (red traces). The gap is augmented with increasing positive/negative curvatures κ.

dent Li^+ diffusion coefficients, $D_+(T)$, and mobilities, $\mu_+(T)$, under local electric field $\vec{\mathbf{E}}(x,y,t)$ and temperature $T(x,y,t)$ fields (x and y are the parallel and perpendicular coordinates to electrodes surfaces). $D_+(T)$ is assumed to follow an Arrhenius temperature dependence, following Eq. 4.13:

$$D_+(T) = D_+^0 exp(\frac{E_\eta}{Nk_B}(\frac{1}{T} - \frac{1}{T_0})) \tag{4.13}$$

from which we evaluate $\mu_+(T)$ by using the Stokes-Einstein relation, Eq. 4.14:

$$\mu_+(T) = \frac{eD_+(T)}{Nk_BT} \tag{4.14}$$

k_B is Boltzmann's constant, N is Avogadro's number, e is the elementary charge, and $E_\eta = 13.5kJmol^{-1}$ is the experimental activation energy derived from viscosity $\eta(T)$ data for the PC solvent (Table 2.1).[102] Temperature $T(x,y,t)$ and electric field $\vec{\mathbf{E}}(x,y,t)$ profiles were evaluated by finite-differences integration of Eq. 2.9. The surface of electrodeposits was set at T_- and V_- throughout, on account of the high Li^0 thermal conductivities. CG-MC simulations were run in a $[L^* \times L^*]$, domain

that approximately corresponds to the thickness of the depletion layers where the relevant events take place in this system (Table 2.1). The actual D_+(T) value used in the calculations was scaled down from experimental values ($D_+^{Exp}(300K) = 2.58 \times 10^{-6} cm^2 s^{-1}$ [99] for Li^+ diffusion in PC to yield diffusional displacements $< x^2 >^{\frac{1}{2}} \approx L^*/2$ at the end of simulations.[95] Since the $\Delta t = 0.25 \mu s$ simulation time-step is much longer than the *picosecond* time-scale of ion-ion collisions, Li^+ ions positions $\vec{r}_i(t)$ were computed from average displacements given by Eq. 2.6.

We further assumed that Li^+ is reduced to Li^0 with temperature-independent unit probability under the applied overpotentials. The actual parameters used in the simulations are listed in Table 4.1.

Since dendrites tips are intrinsically metastable formations possessing excess surface free energy relative to flat Li^0 crystals, [24, 12] they should eventually relax at appreciable rates via Li^0-atom diffusion into interfacial sites of lower curvature/higher connectivity at sufficiently high temperatures.[103, 85] This relaxation process was incorporated into our model calculations by releasing Li^0 atoms with probabilities $p_R(T)$ given by Eq. 4.15: [103]

$$p_R(T) = p_R^0 . exp(\frac{\Delta E_R^{\ddagger}}{N k_B T}) \tag{4.15}$$

p_R^0 is an adjustable dimensionless pre-factor and $\Delta E_R^{\ddagger}$ is the effective activation energy for Li-atom hopping on our dendritic electrodeposits. The pre-factor was selected such that relaxation rates were competitive with deposition rates. We found that the temperature dependence of the $\bar{\lambda}(T)$ calculated in this manner was not overly sensitive to the value of the pre-factor, as long as the above condition was satisfied. At each integration step, Li^0 atoms are released into the electrolyte as Li^+ ions at distances $4r_+$ ($r_+ = 1.19 \mathring{A}$ is Li^+ crystalline radius) away from the nearest surface Li^0 atoms, which then evolve according to Eq. 2.6. Each interfacial Li^0-atom undergoes on average 4-5 rearrangements per simulation. The dissolution of Li^0 into Li^+ in close proximity of deposits followed by re-deposition is operationally equivalent to the diffusion of Li^0 atoms from dendrite tips to concave regions. This is so because

Li^+ ions released from dendrite tips have fewer neighboring surface sites to which return as Li^0 than those released from concave anode regions. Simulations were stopped the first time 400 Li^0 appeared the system. The total number of Li^+ ions was preserved by creating a new Li^+ at a random location whenever another Li^+ was annihilated as Li^0. Calculated dendrite heights were quantified by dividing the x-axis in four sectors. Here, *dendrite height* in each sector is the height of the uppermost Li^0 defined by Eq. 2.8.

To ensure good statistics, each simulation was run 10 times. From this information we evaluated $\bar{\lambda}$ values for comparison with experimental ones. Fig. 4.8 shows typical snapshots of calculated dendrites at three T_- values. In Fig. 4.9 computational $\bar{\lambda}$ values calculated by excluding and including surface relaxation are compared with experimental $\bar{\lambda}$ ones.

4.5 Results & Discussion

Our experimental results show that keeping the anode warmer than the surrounding solution does inhibit dendrite growth. We have recently shown that the positive feedback underlying runaway dendrite growth is due to the fact that Li^+ electromigration in the strong electric fields developing around high-curvature dendrite tips outpaces Li^+ diffusion to flatter regions.[8] Since D_+ and μ_+ increase exponentially with T, and the electrolyte filling concave pockets is significantly warmer than the layers surrounding dendrite tips 4.1, we expected that the application of negative temperature gradients to the anode would enhance diffusionally-limited current densities to concave regions relative to dendrite tips. In other words, we expected that model simulations of the relatively faster Li^+ electrodeposition on anode regions surrounded by warmer electrolyte layers would account for our experimental findings.

The results of GC-MC simulations (Fig. 4.9) dispelled our simplistic expectations. The reasons are that the $D_+(T)$, $\mu_+(T)$ dependences originating from $E_\eta = 13.5$ kJ.mol^{-1} (Table 4.1) are not only halved into diffusional $\bar{\lambda}(T)$ displacements, but they are also attenuated by the competition between ion diffusion and electromigration in

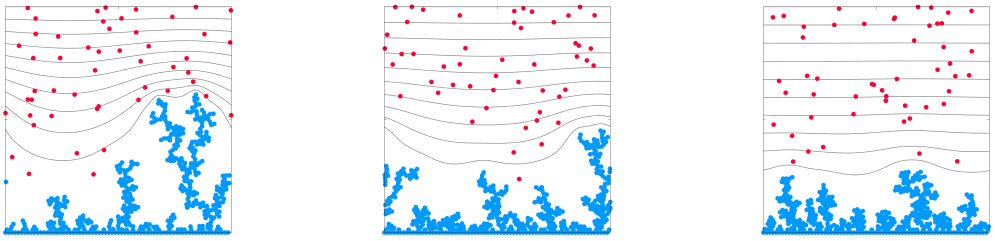

Figure 4.8: Results of CG-MC calculations for Li^+ transport. Li^0, Li^+, $|T|$. From left to right, results at T$_-$ ={21,48,70}^0C.

Table 4.1: Temperature dependent CG-MC simulation parameters.

D_+	3.4 $\times 10^{-8} cm^2/s$
r_+	1.19 Å
E	13.5 $KJmol^{-1}$
$\Delta E_R^{\ddagger}$	20 $KJmol^{-1}$
p_R^0	300

the non-linear $T(x,y,t)$, $\vec{\mathbf{E}}(x,y,t)$, and $[Li_+(x,y,t)]$ fields surrounding the irregular Li^0 deposits (Fig. 4.8). Thus, the results of Fig. 4.9 in effect implicate the participation of a process having a stronger temperature dependence that that is associated with Li^+ transport in the electrolyte solvent. Thus, we found that we could match the experimental $\bar{\lambda}(T)$ temperature trends by including the thermal relaxation of Li^0 dendrites, as simulated by the process described above, with $\Delta E_R^{\ddagger} \approx 20 KJmol^{-1}$.

A transition state theory (TST) analysis of atom diffusion in metallic solids provides a physical interpretation of our findings.[104, 105, 106] The TST expression for the diffusion coefficient D_{TST} of Li-atoms on the surface of Li^0 metal is given by Eq. 4.16.[98]

$$D_{TST} = \frac{1}{4} a^2 \frac{k_B T}{h} exp(\frac{\Delta S^*}{N k_B T}) exp(\frac{\Delta E^*}{N k_B T}) = D_{TST}^0 exp(\frac{\Delta E^*}{N k_B T}) \tag{4.16}$$

where $a = 3.49$Å is the lattice constant, h is Plank's constant, and ΔS^* and ΔE^* are the activation entropy and enthalpy of the process. Thus $D_{TST} \approx 2 \times 10^{-3} cm^2 s^{-1} exp(\frac{\Delta S^*}{N k_B T}) exp(\frac{\Delta E^*}{N k_B T})$ at $T_{1/2} = 318K$, the mean temperature in our ex-

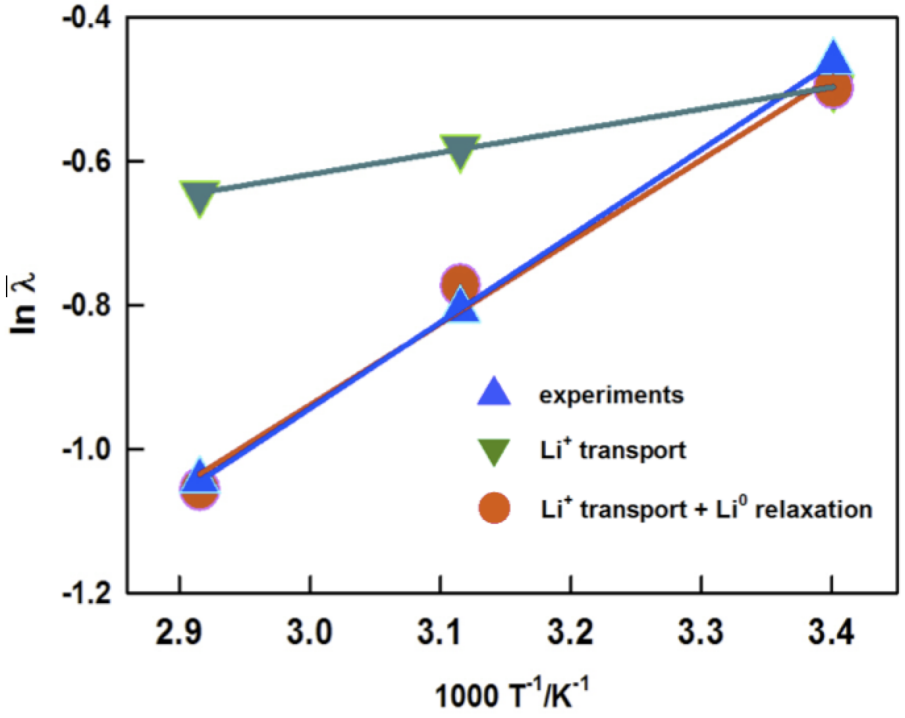

Figure 4.9: Arrhenius $log(\bar{\lambda})$ vs. $1/T$ plots. Simulated data (green and blue points) pinned to the experimental value (red) at 21^0C for 16mAh charge to help visualize slope differences.

periments. By assuming that the shortening of dendrites at higher temperatures is due to Li-atom diffusion from dendrite tips to sites of higher coordination, we interpret that relative $((\Delta\bar{\lambda} =< x^2 >_2 (T))^{1/2} - (< x^2 >_{T_0=21^0C})^{1/2}$ experimental decrements (from Fig. 4.3-a) correspond in fact to average Li-atom diffusional displacements on the surface of dendrites. On this basis, from $D_{exp} = \bar{\Delta\lambda}^2(2\tau)^{-1}$, $\tau = 8hrs$, we estimate an average experimental diffusion coefficient $D_{exp} \approx 9 \times 10^{-8} cm^2 s^{-1}$ at $T_{1/2}$. By identifying D_{TST} with D_{exp} , and $E_R^{\ddagger}$ with E^* we derive a pre-factor $D_{TST}^0 = 4 \times 10^{-5} cm^2 s^{-1}$ that is in the range of those typical for atom self-diffusion on metal surfaces, [107, 108, 109] and leads to a significant negative entropy of activation: $\Delta S^* = -46 Jmol^{-1} K^{-1}$, consistent with the transformation of (disordered) amorphous Li^0 dendrites into Li^0 crystals.[110, 111] Gratifyingly, the $\Delta E^* = 20 kJmol^{-1}$ value derived from our experiments and CG-MC calculations falls within the range of the DFT values for the activation barriers of Li-atom hopping and exchange on Li(001) and Li(111) single crystals.[97] The type of surface reconstruction we observe for metallic lithium dendrites above ambient temperatures is a universal phenomenon.[103] For a melting point of bulk Li^0: $T_{MB} = 180^0C = 453K$, the condition T/T_{MB} ¿ 0.7 that determines the onset of surface reconstruction is already met by Li^0 at $\approx 300K$. [103] The above condition, which strictly applies to flat Li^0 crystals, will be relaxed for microcrystalline dendrites because the melting point T_{MD} of dendrite tips of radius of curvature ρ is necessarily lower than T_{MB}. The Gibbs-Thompson Equation relates T_{MD} to T_{MB} as following: [112, 113, 114]

$$T_{MD} = T_{MB}(1 - \frac{\sigma_{S,L}}{\Delta H_{MB} d_S \rho}) \tag{4.17}$$

with solid-liquid surface energy $\sigma_{S,L} = 0.41 J.m^{-2}$, [115, 116] melting enthalpy $\Delta H_{MB} = 512 Kg.m^{-3}$, and solid density $d_S = 430 kJKg^{-1}$, we estimate that, for example, the T_{MD} of conceivable dendrite tips sharper than $\rho < 73nm$ would be $T_{MD} < 0.9 T_{MB} \approx 400K = 127^0C$.

4.6 Conclusions

Summing up, our experiments and calculations open up the possibility that the run-away growth of electrolytic Li^0 dendrites could be better controlled by increasing the mobility of Li-atoms on the solid than by increasing the mobility of Li^+ ions in the electrolyte. They also suggest specific approaches, such as enhancing interfacial Li-atom diffusion by implanting extrinsic defects. [106, 117, 118, 119, 4]

Chapter 5

Thermal Annealing Kinetics of Electrodeposited Lithium Dendrites

5.1 Abstract

The densifying kinetics of lithium dendrites is characterized with effective activation energy of $E_a \approx 6 - 7kcal.mol^{-1}$ in our experiments and molecular dynamics computations. We show that heating lithium dendrites for 55C reduces the representative dendrites length $\bar{\lambda}(T,t)$ up to 36%. NVT reactive force field simulations on three-dimensional glass phase dendrites produced by our coarse grained Monte Carlo method reveal that for any given initial dendrite morphology, there is a uniquely stable atomic arrangement for a certain range of temperature, combined with rapid morphological transition ($\sim$ 10 ps) within quasi-stable states involving concurrent bulk and surface diffusion. Our results are useful for predicting the inherent structural characteristics of lithium dendrites such as dominant coordination number.

5.2 Introduction

Wireless revolution and need for harnessing intermittent renewable energy sources, has created an exponential demand for energy storage devices such as batteries that require long-lasting storage capacity and high-power delivery during last decade. [10]

Lithium (Li^0), particularly, anode candidate material with an ideal energy density of 3862 mAh/g, could drastically satisfy this demand. However, due to it relatively low surface energy, it has very high propensity to grow dendrites during consecutive recharging. This phenomenon eventually leads to short-circuiting, overheating the cell and possible ignition of the organic electrolyte as well as creating isolated *dead lithium* crystals. [3] The current reports have investigated the effect of charging method, [8, 17] current density[25, 2, 7], electrode surface morphology [36, 58, 18], solvent and electrolyte chemical composition [27, 28, 26], electrolyte concentration [25, 61]on dendrite growth. Other methods include the use of powder electrodes [31] and adhesive polymers [32]. Recent studies have tried to explain the dendrite evolution mechanism [64] and have offered impurities as dendrite initiation drive [13, 63] . Although the ongoing research tends to extend the battery energy density by developing Lithium-Air and lithium-Sulfur batteries, the dendrite problem remains as a challenging issue in all kinds of rechargeable batteries. [92, 93] Temperature is a highly accessible parameter with foremost important effect in kinetics. It has been found that cycling at higher temperatures (from -50C up to 40C) can, on average, cause more frequent short-circuiting events up to a factor of 2 [120]. Other results show that the increasing cell temperature enhances the ionic mobilities in favor of dendritic inception and growth [40]. [25, 121] reported that the higher temperatures extends ion depletion layer length which is in agreement with temperature dependence of reaction rates [2]. [34] also pointed out that the probability of ionic reduction in the electrode surface correlates directly to the temperature. In contrast, [59] found that imposing higher temperatures reduces dendrite growth rate relatively to the electrode surface, and could results in more uniform deposition. Although all those approaches are helpful, it is apparent that further progress in tackling this crucial issue should accrue from a full understanding of the dynamics of dendrite growth on Li-metal electrodes. [122, 13]

In our recent work, we have found that applying temperature gradients has a destructive effect for growing dendrites during charging periods [80, 60] and show experimental evidence that higher post-charge temperatures can reduce lithium den-

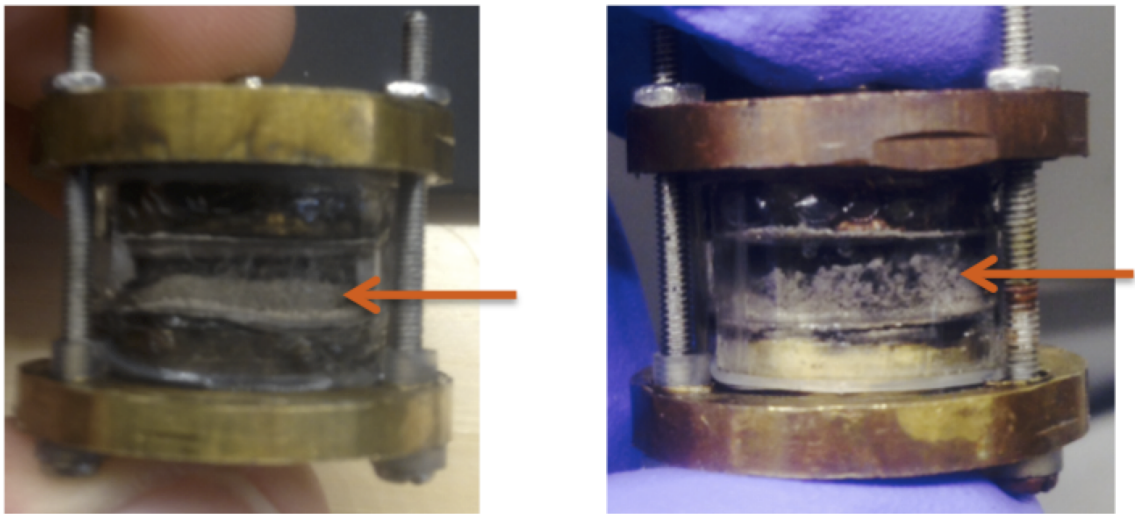

Figure 5.1: Lithium dendrites observable by naked eye. While certain morphologies are packed and shorter in height (left: $\bar{\lambda} \approx 0.4L$), others tend to be highly porous and taller in height (right: $\bar{\lambda} \approx 0.7L$), L:Inter-electrode distance

drites to a considerable amount. We train a reaxFF model afterwards for the initial morphologies and we explain reasons leading to such reduction in details from QM insights.

5.3 Experiments

We have used unique manually-made cells for in situ observation and measurement of electrolytic Li0 deposits (Fig. 2.2). The cell components and details of the fabrication for electrode and electrolyte have been described in previous chapter. Four cells were charged at the rate of 2mA/cm^2 for 24 hours (Q=48mAh) in ambient condition using Bio-logic instruments (SP-50, VSP). The cells were disconnected, taken out and rinsed with isopropyl alcohol. The optical observations were done on the post-charge anode surface and the cells were kept in various oil bath temperatures. The design enables observation of dendrites with naked eye.(Fig. 5.1)

In another set of experiments, 4 cells were charged under different current densities for 24 hours. The cells were disconnected and submerged in oil bath of different temperatures. The dendrites were measured under microscope after 12 hours and 24

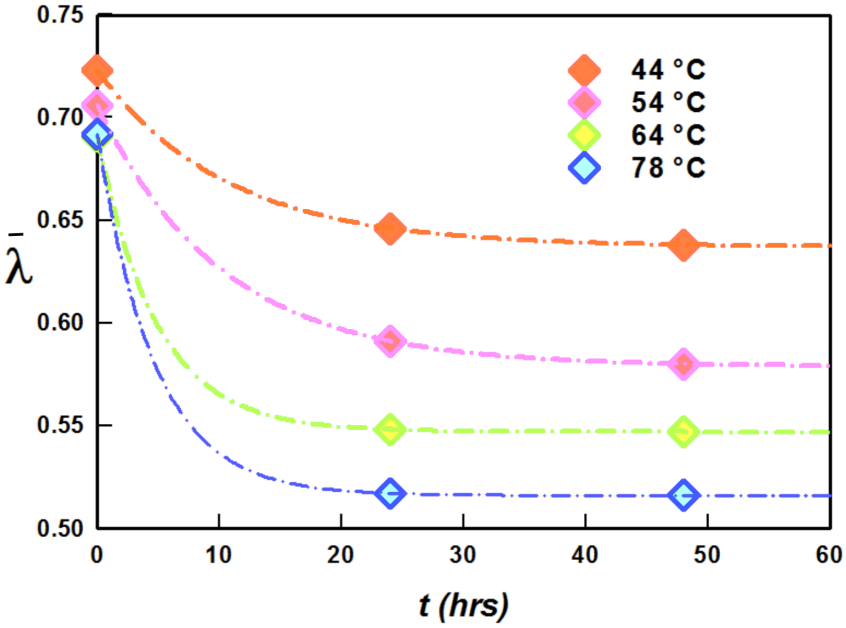

Figure 5.2: $\bar{\lambda}$ versus bath temperature for 4 various bath temperatures during 48 hours post-charge period.

hours and $\bar{\lambda}$ was extracted. (Fig. 5.2)

5.4 Simulations

We have utilized ReaxFF method to describe the interactions of deposited Li^0 atoms after deposition. [123] In ReaxFF, the interatomic interactions can be expressed as a function of bond orders where the energy terms can be expressed as:

$$E_{system} = E_{bond} + E_{lp} + E_{over} + E_{under} + E_{val} + E_{pen} + E_{C2} + E_{triple} + E_{tors} + E_{conj} + E_{H-bond} + E_{vdW} + E_{Coulomb} \quad (5.1)$$

The force field used is trained against extensive atomic structures, including charge, bond dissociation energy, geometry of finite moles, different crystal phases (cell parameters, relative stabilities and equation of state) and energy data. For Li metal, the training set includes Li_2^+ bond dissociation curves, crystal structure of dif-

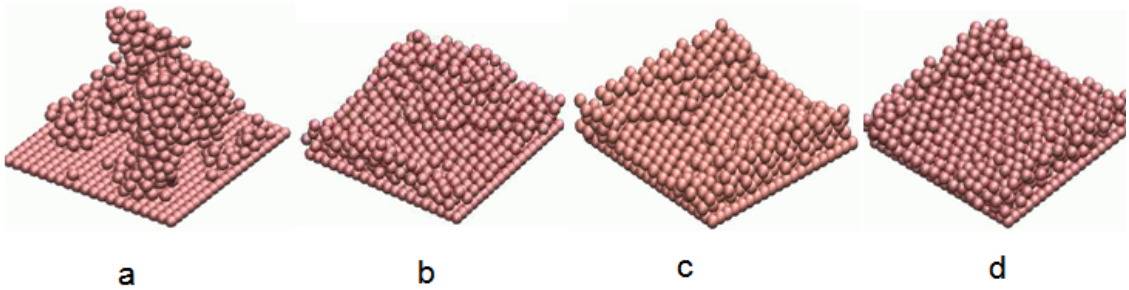

Figure 5.3: Initital optimized dendrite glass phase after charge, driven from CG framework. Final morphologies are shown after 200ps NVT simulations at 317K(b), 337(c) and 357(d) are demonstrated.

ferent crystal phases (BCC, FCC, HCP, diamond and SC), atomization energy, and energy differences of these crystals and equation of state (EOS). We also consider the surface energy of (100), (110) and (111) Li BCC. Without further training, ReaxFF can well reproduce the surface energy values obtained from QM calculations. We start from the parameters obtained from simple Li-Li bond as the initial set of data constants bond iterate it for the pyramid model until the convergence.

The initial glass phase morphology of dendrites are generated from our previously developed coarse grain (CG) framework [8], which utilized the same parameters for lithium electrode and $LiClO_4$/PC solution. Energy minimization was carried out using reaxFF with imposing fixed bottom layers for Li. The optimized structure is a glass phase of Li crystal (100) surface as shown in Fig. 5.3. NVT simulations were applied with temperatures ranging from 317K to 357K to investigate the temperature effect in elimination of dendrites. During the simulation in most cases, at the beginning, the Li dendrite quickly collapsed and filled up with available space. After 200 ps of simulation time, 3 to 5 atoms think layers were developed. Fig.5.3-b to 5.3-d show the atomic structures after 200 ps simulation. Although not fully crystalized, the obtained structures show ordered arranged Li atoms, which is a feather of crystalline morphologies.

In order to investigate the dendrite collapse in more details, we have considered an ideal case of initial pyramid morphology for simulation that consists of 15 layers of Li bulk (7715) and 6 layers of Li pyramid leading to single atom tip(Fig.5.4). The

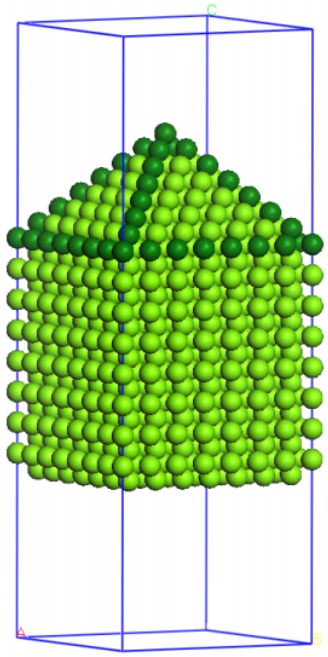

Figure 5.4: The simulation pyramid tip model.

size in x and y direction is 24.57Å and in z direction is 38.61 Å . A 30Å vacuum space is built to avoid the interactions between the slab and its imagines. Since nano-scale structures usually exhibit very low melting point comparing with that in bulk phase, we fixed the bottom ten layers to avoid the unrealistic melting.

Model parameters are shown in Table 5.1.

We recognized two dominant reduction mechanisms:

1. **Bulk Diffusion (BD):** The ad-atom creates a vacancy with energy barriers staring from 9.715 kcal/mol to create a vacancy, followed with vacancy diffusion with very small barriers (2.490 kcal/mol) which make it easy for the vacancy to diffuse from bottom to top and may lead to structure collapse.(fig. 5.6)

2. **Surface Diffusion (SD):** The ad-atom drops off from top with energy barrier starting from 5.198 kcal/mol, with followed diffusion with increased barriers, 10.082 kcal/mol, from layer 2 to layer 3, and 11.185 kcal/mol, from layer 3 to layer 4.(Fig. 5.5)

From this point of view, BD mechanism may be more prevalent than the SD

Table 5.1: Pyramid model characterisitics

x and y dimensions	24.57 Å
z dimension	1 μs
Cube layers	$7 \times 7 \times 15$
Tip layers	15
Domain width	24.57 Å$\times$ 24.57 Å
Domain height	10.53 Å
Target temperatures	250K, 300K, 350K, 400K, 450K (melting point)
Simulation time	200 ps
Simulation time step	0.25 fs

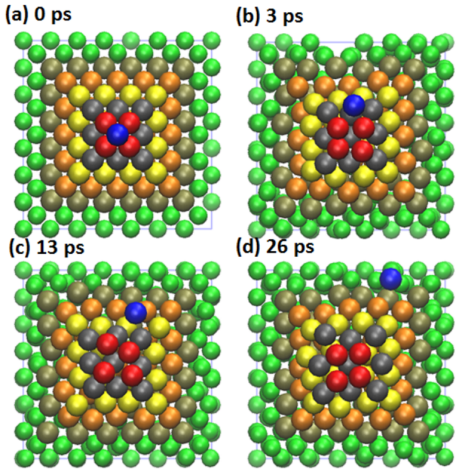

Figure 5.5: Surface diffusion:The tip atoms falls frop the at 250K.

mechanism, because the diffusion barrier of the rate determining step (9.715 kcal/mol) in BD is lower than that (11.185 kcal/mole) in SD. However, the difference is so small (maybe even smaller if consider the entropy), it is highly possible that both of these mechanism occur in the realist conditions, which make it hard to distinguish the contributions of these mechanism in the simulation.

Assuming the flatten of the tip follows Arrhenius equation, we can also derive the effective energy barriers by calculating the melting rate at evaluated temperatures, 350K, 400K and 450K. The activation energy barrier obtained from fitting to Arrhenius equation is 7.196 kcal/mol (as shown in Figure 10), consistent with the NEB calculations.

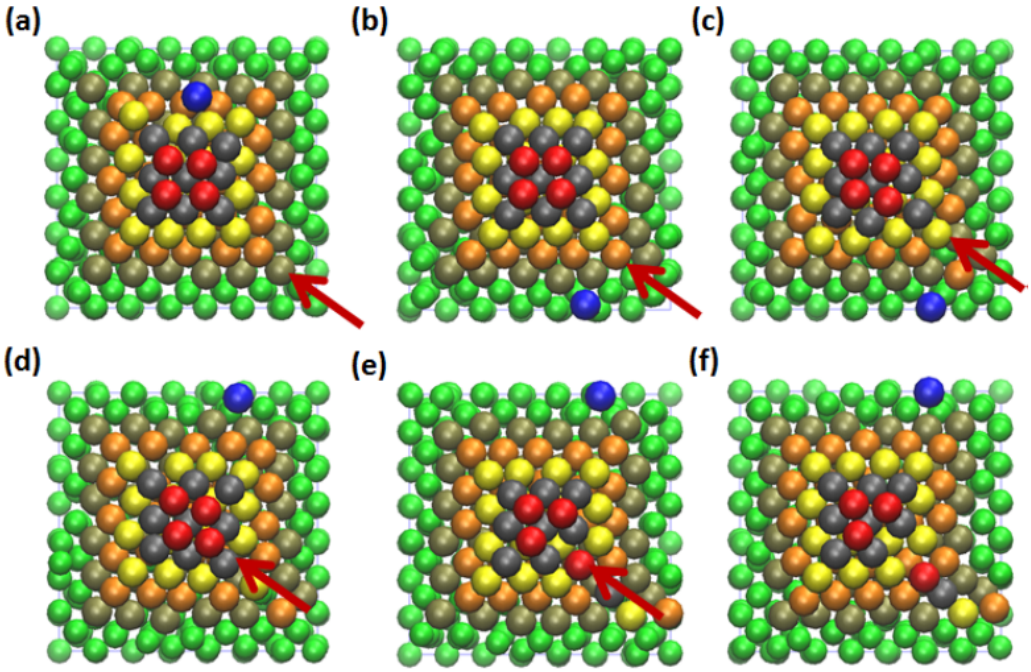

Figure 5.6: Bulk diffusion: A bottom atom created vacancy that diffuses to the top and leads to collapse of pyramid.

5.5 Resutls & Discussion

It is very obvious that the higher post charge temperatures anneals the dendrites to lower heights.(Fig. 5.7) We interpret that the degradation (reduction) of lithium dendrites follows the first-order kinetics and we ascribe the following:

$$\bar{\lambda} = \lambda_{\infty} + a.exp(-k.t) \tag{5.2}$$

The reduction rate k in our experiments shows to be affected by temperature T. Considering Arrhenius relation for kinetics, we have the following equation:

$$k(T) = k(T_0)exp(\frac{E_a}{k_B}(\frac{1}{T} - \frac{1}{T_0})) \tag{5.3}$$

As we compare the experimental and computational calculated energy barriers, they fall in the proximity of each other. (Fig. 5.8).

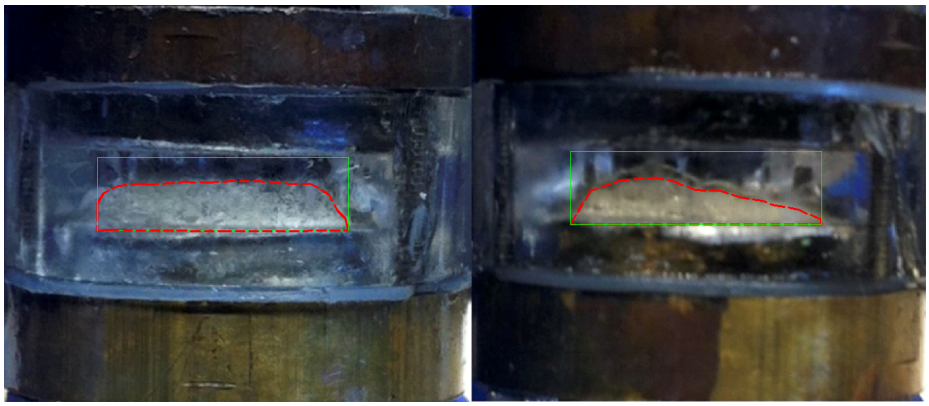

Figure 5.7: The morphology of post-charge lithium dendrites before (left) and after (right) imposing higher temperatures.

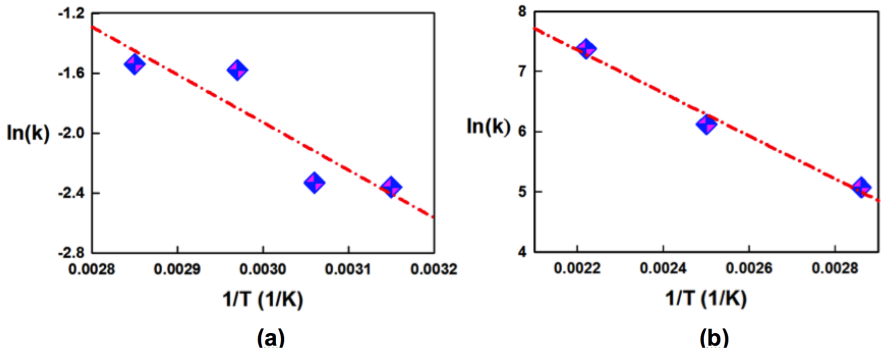

Figure 5.8: Comparison between experimental (a) and computational (b) energy barriers, which are **7.1 kcal.mol**$^{-1}$ and **6.3 kcal.mol**$^{-1}$ respectively.

5.6 Conclusion

In this work, we quantified the thermal annealing kinetics of lithium dendrites in our experiments and simulations. We produced the lithium dendrites in laboratory experiments and measured their temperature dependent reduction via a novel design and method. On the other hand, we created lithium dendrites using our CG-MC framework and by training ReaxFF framework for lithium, we predicted their effective thermal relaxation energy barrier. The acquired effective activation energy of 7.1 kcal/mol from the experiments matches well with the corresponding value of 6.3 kcal/mol from simulations. The surface diffusion of low-coordinated atoms and bulk diffusion were ascribed as the dominant mechanisms for thermal relaxation of lithium dendrites. The results have potential for predicting the internal structural properties of amorphous dendrites such as the dominant coordination number, porosity, branching characteristics and material dependency. Further work along these lines is underway and the corresponding publication is in press.

Appendices

Appendix A

The Role of Fluoride Additive on SEI layer and Lithium Dendrites Inhibition

A.1 Abstract

The mechanism for controlling lithium dendrites growth due to fluoride electrolytic additive has been extracted. Our experiments reveal that fluoride is, in fact, deterministic for creating more compact solid electrolyte interphase (SEI) on the pre-charge lithium electrode surface before nucleation of lithium dendrites which is considerably more stable during subsequent cycles. We attribute this phenomenon to the cleaning of the electrode surface by creating HF, which reduces the nucleation (i.e. active) sites. Furthermore we prove that F- ions diffuse at the dendrites structure as an interstitial impurity due to their small size and which facilitate the collapse of metastable lithium dendrites during electrodeposition.

A.2 Introduction

Dendrite growth has been considered one of the major problems facing rechargeable batteries. Major efforts were made testing the effects of solvent and electrolyte chemical composition and concentration on dendrite reduction [26, 27, 28, 29]. A recent study on the effect of fluoride ion has motivated us to investigate the mechanism of

such effects in more detail. [105]

Our previous experiments on the thermal relaxation of electrodeposited lithium metal dendrites within hours at temperatures well below the melting point of Li^0 revealed that dendrites are metastable structures that must eventually reconstruct into thermodynamically stable Li^0 crystals, whose imperfections also manifest into enhanced relaxation rates. On the basis of microscopic concepts about the dynamics of this process [98, 106].The idea suggested itself that thermal relaxation rates should be accelerated by the presence of interstitial impurities.

The conceptual issue at stake was whether relaxation was due to surface diffusion of Li-atoms, or it also involved large atomic displacements within dendrites bodies. Surface diffusion on metals is an important subject that has been extensively investigated for almost a century. There are reports on hetero-diffusion of lithium atoms on W and graphite [124]. However, the thermal relaxation of fractal lithium electrodeposits is a specialized subject that has apparently not received much attention, either experimentally or theoretically, until very recently.

In 2014, Archer et al. [105] have shown that lithium dendrites are not inevitable. Remarkably, electrolysis of Li halides instead of Li perchlorate electrolytes in PC led to significant dendrite reductions, a phenomenon they attributed to the enhancement of the surface mobility of Li-atoms by the selective enrichment of lithium halide salts in the interfacial layers of electrodeposits. This finding resonates with our results on the unexpectedly fast thermal relaxation of lithium dendrites at above-ambient temperatures, and our conjecture that surface diffusion of Li-atoms could be enhanced by the injection of suitable impurities.

A.3 Experiments

We conducted two sets of experiments based on the design and method of measurement defined in Chapter 2. In the first set, we electrolyzed 4 identical cells, two of them filled with 0.1M $LiClO_4$/PC and the other two with 0.1M LiF/PC. We confirmed

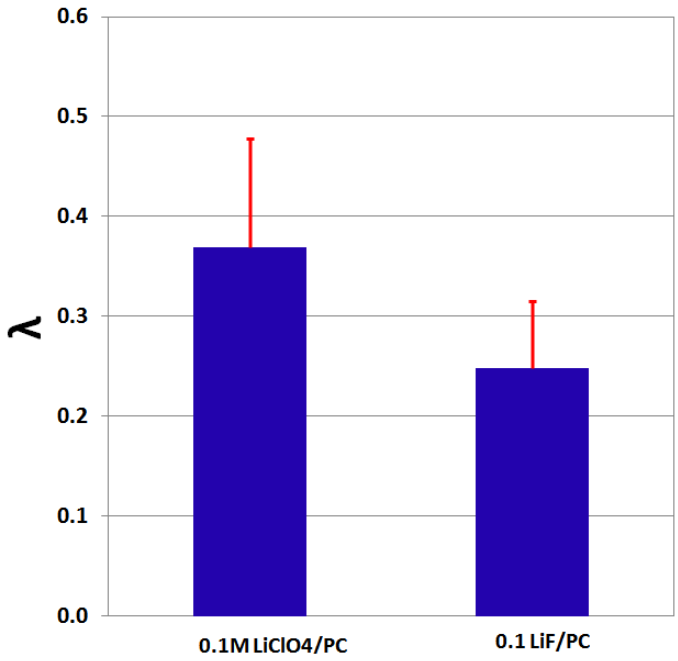

Figure A.1: Dendrite measure (defined in Eq. 2.3) vs electrolyte type. (C=0.1 M/PC)

Archer's results in our laboratory by comparing average dendrite lengths grown in cells filled with 0.1M LiF and 0.1 M $LiClO_4$ charged under identical conditions with the rate of 0.125 $mA.cm^{-2}$.Fig. A.1

In the second set of experiments, we fabricated 4 cells, 2 cells with $LiClO_4$/PC and 2 other cells containing the same electrolyte with addition of 0.1M LiF/PC. We charged the cells with the rate of 0.125$mA.cm^{-2}$ for 24 hours (C=3 mAh/cm^2). After imaging the 4 cells, we removed the electrolyte from the 2 cells containing LiF, rinsed and refilled them with original electrolyte (1M $LiClO_4$/PC) and applied another set of charge with the same rate and period as previous cells so the total charge applied to them become double (C=6 mAh/cm^2). The results after imaging and microscopic measurement of images (from Eq. 2.3) are shown in Fig. A.2.

The SEM comparison of the electrolytes has been illustrated in Figure A.3.

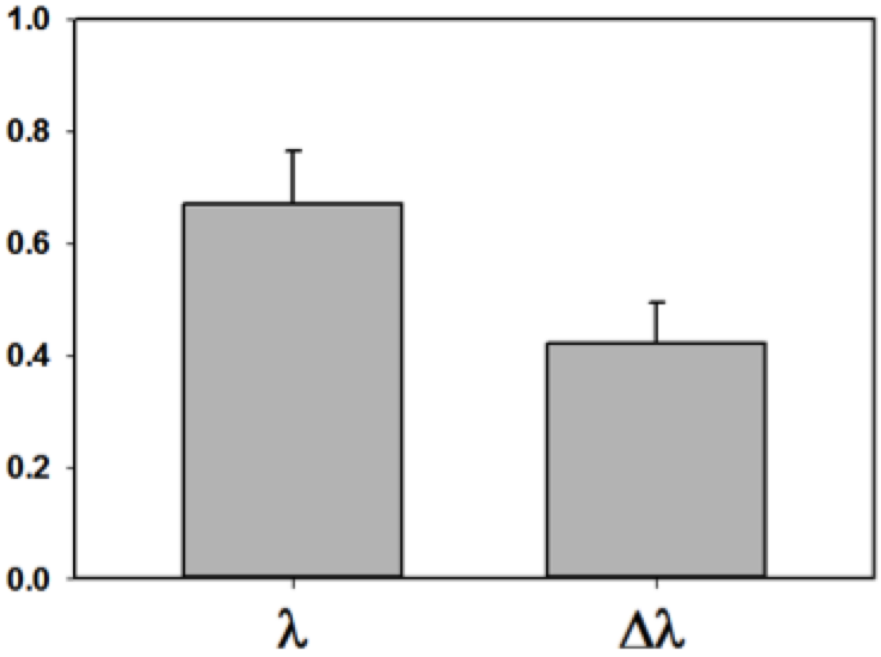

Figure A.2: The dendrites formed on the flat surface (left) versus the additional dendrites formed on the original dendrites produced in the presence of F^-.

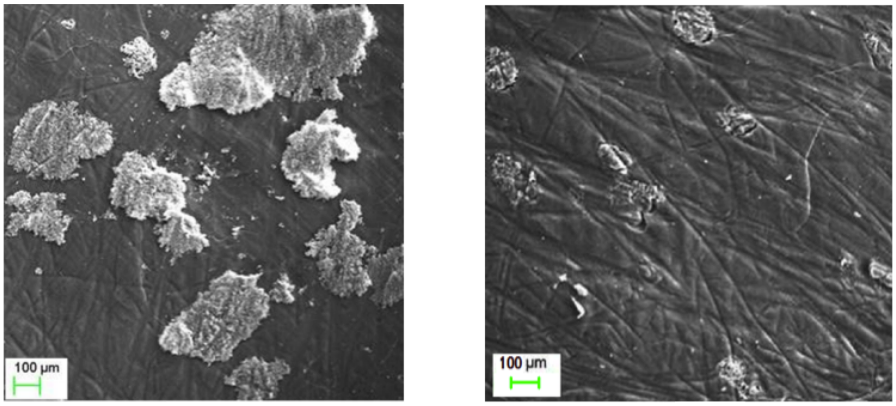

Figure A.3: SEM image for the morphology of dendrites using electrolytes types of without (left) and with (right) electrolytes

A.4 Conclusion

In this paper we have realized the mechanism of suppression of dendrites due to fluoride additive to the electrolyte. We have obtained that: i. the SEI passivation layer is more compact and stable in the presence of F^- due to higher decomposition of PC solvent. ii. The F^- diffuses inside the dendrites and SEI structure as an interstitial impurity and causes the structural instability in the meta-stable dendrites. We ascribe this effect due to small size on F^-. The corresponding publication is in press.

Appendix B

Appendix II: Potential and Chloride Role on COD Removal

Acknowledgement: We acknowledge Kangwoo Cho. who has conducted the major research in this chapter. The detailed content is published in the Environmental Science and Technology, 2014, 48(4), pp 2377-2384.[8]

http://pubs.acs.org/doi/abs/10.1021/es404137u

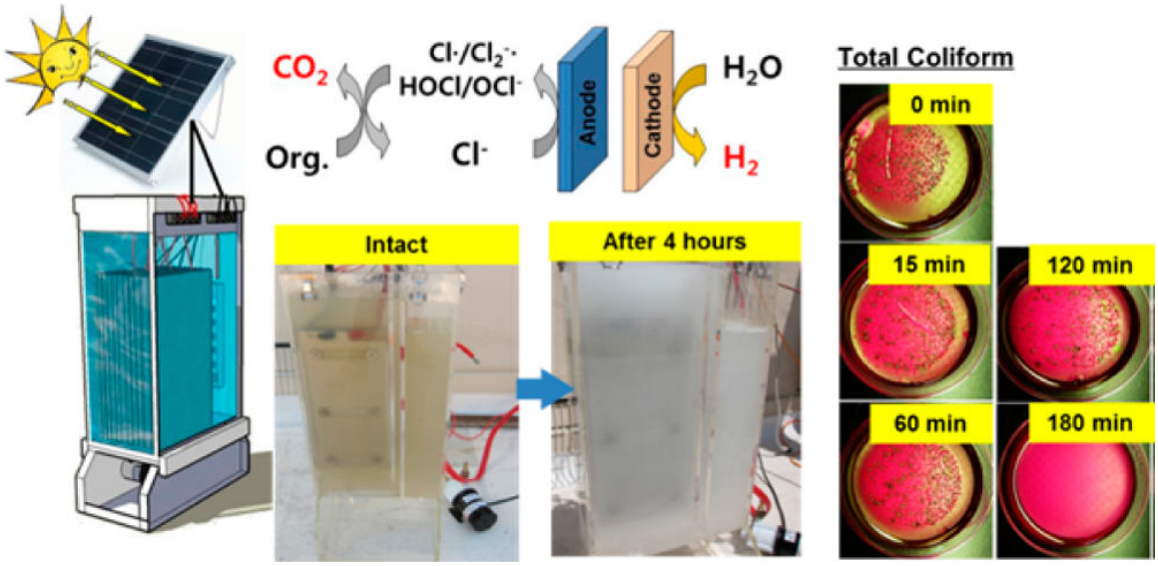

Figure B.1: Graphical Abstract

B.1 Abstract

We have investigated electrochemical treatment of real domestic wastewater coupled with simultaneous production of molecular H_2 as useful byproduct. The electrolysis cells employ multilayer semiconductor anodes with electroactive bismuth-doped TiO_2 functionalities and stainless steel cathodes. DC-powered laboratory-scale electrolysis experiments were performed under static anodic potentials ($+2.2 or +3.0 VNHE$) using domestic wastewater samples, with added chloride ion in variable concentrations. Greater than 95% reductions in chemical oxygen demand (COD) and ammonium ion were achieved within 6 hours. In addition, we experimentally determined a decreasing overall reactivity of reactive chlorine species toward COD with an increasing chloride ion concentration under chlorine radicals ($Cl.$, Cl_2^-) generation at +3.0 V NHE. The current efficiency for COD removal was 12% with the lowest specific energy consumption of $96 kWh kgCOD^{-1}$ at the cell voltage of near 4 V in 50 mM chloride. The current efficiency and energy efficiency for H_2 generation were calculated to range from 34 to 84% and 14 to 26%, respectively. The hydrogen comprised 35 to 60% by volume of evolved gases. The efficacy of our electrolysis cell was further demonstrated by a 20 L prototype reactor totally powered by a photovoltaic (PV) panel, which was

shown to eliminate COD and total coliform bacteria in less than 4 h of treatment.

B.2 Introduction

In wastewater electrolysis cells (WEC), environmental pollutants can be eliminated by either direct heterogeneous or indirect homogeneous oxidation/reduction pathway.[125] Surface-bound reactive oxygen species (ROS) are intermediates in O_2 evolution during water splitting which may also result in the direct oxidation of chemical substrates.[126] ROS also reacts with chloride in wastewater to produce reactive chlorine species (RCS) such as free chlorine (Cl_2, HOCl, ClO^-) and chlorine radical species (Cl, Cl_2^-).[127, 128] Organic substrates can be converted via reactions with RCS to CO_2 and an array of lower molecular weight carboxylic acids.[129] At the same time, with sufficient RCS generation, disinfection of fecal coliform bacteria can be achieved. Inexpensive polycrystalline photo- voltaic (PV) panels can be used to convert incident solar irradiation into a direct current (DC) potential across anode-cathode pairs to produce ROS.[130] Water oxidation at the anode is balanced in part by water or proton reduction at the cathode to produce H_2.

B.3 Experiments

The semiconductor anodes employed in this study were prepared according to a basic procedure described in previous reports.[129, 130]Cyclic voltammetry (CV) profiles were collected over a range of 0 to 2.0 V NHE by three repetitive scans (5 mV s^{-1}) in quiescent 30 mM NaCl solution. In benchtop reactors, the electrode module was installed in a single compartment cell with working volume of 60 mL.

B.4 Prototype

A 20 L WEC powered by a PV panel was tested in roof-top experiments in order to assess the feasibility of PV panels as the sole source of energy for COD elimination

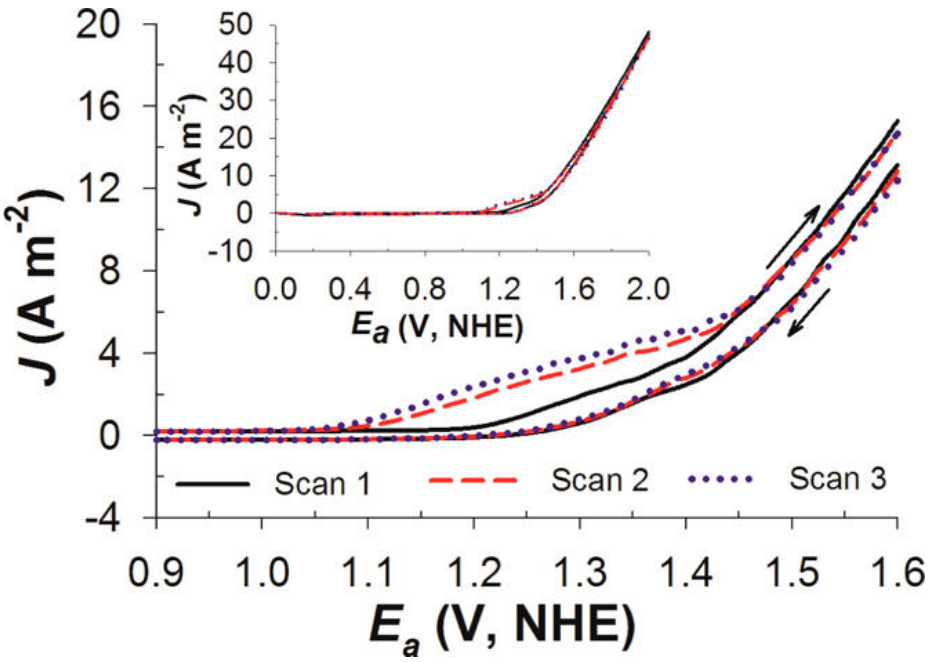

Figure B.2: CV of the BiO_x/TiO_2 anode in 30mM NaCl.

and disinfection due to in situ RCS generation. The PWEC system had an anode/ cathode array module consisting of five doubly coated BiO_x/TiO_2 anodes and six SS cathodes ($40 \times 20cm^2$ each) with a distance of separation between each anode and cathode pair of 0.2 cm.

B.5 Analysis

COD and total nitrogen (TN) concentration of samples were measured based on the absorbance at 420 nm in UV-vis spectrophotometer (Agilent, USA), after digestion in a low-range dichromate digestion solution (3-150 mg.L^{-1}, Hach, USA) and in a low-range TN reagent set (0.5-25 mgN L^{-1}, Hach, USA), respectively. Anions (Cl^-, $ClO3^-$, NO_3^-) and cations (NH_4^+, Ca_2^+, Mg_2^+) were simultaneously determined by ion chromatography (Dionex, USA), using anion-exchange column (Ionpac AS 19) and cation-exchange column (Ionpac CS 16). The total chlorine (ClDPD) was measured using DPD (N,N-diethyl-p-phenylenediamine) reagent (Hach, USA) coupled with quantification via absorbance measurements at 530 nm. A standard wastewater membrane filtration method was used to count the number of total coliforms and

fecal coliforms during electrolysis.

B.6 Results & Discussion

Fig. B.2 shows CV plots for the BiO_x/TiO_2 anode in a 30 mM NaCl electrolyte solution. The onset potential, which corresponds to $1 Am^{-2}$ of current density, initially appeared at near 1.2 V. In comparison to the reduction potential of O_2/H_2O couple at pH 7, the observed onset potential estimated oxygen evolution overpotential of 0.38 V. This value is quite comparable to RuO_2 and IrO_2 based electrodes,[131] demonstrating that the BiO_x/TiO_2 electrode can be regarded as an active electrode for oxygen evolution. The activity may be attributed to intrinsic oxide vacancies of Bi_2O_3 in lattice structure, which can facilitate the transition of surface-bound hydroxyl radicals to higher oxides.[132] Although a chloride oxidation peak is hidden by the large anodic wave from the oxygen evolution, the chloride oxidation is generally accepted to produce Cl_2.[133, 134] The Cl_2 will be in equilibrium with HOCl and ClO^- in bulk aqueous phase depending on the specific pH.[135] On the other hand, the second and third scan showed a significant decrease of the onset potential to 1.05 V, which would result from a formation of chlorate.[129] The ClO_3^- is known to be produced electrochemically either by oxidation of chloride or free chlorine (HOCl or ClO^-).[136, 137] The decrease in onset potential in Fig. 1 suggests that the chlorate is produced by the oxidation of the RCS [138] which requires 4 electrons for free chlorine oxidation.

When the COD concentration profiles were fit to pseudo-first-order kinetics, the rate constant increased with an increase in E_a. These results are consistent with COD removal in the low E_a that is limited by anodic electron transfer (heterogeneous RCS generation). Under the electron-transfer-limited regime, increasing cell voltage or the current density normally enhances the rate of pollutant degradation, except for those interfacial reactions that are controlled by mass transport.[131, 138, 139, 140]

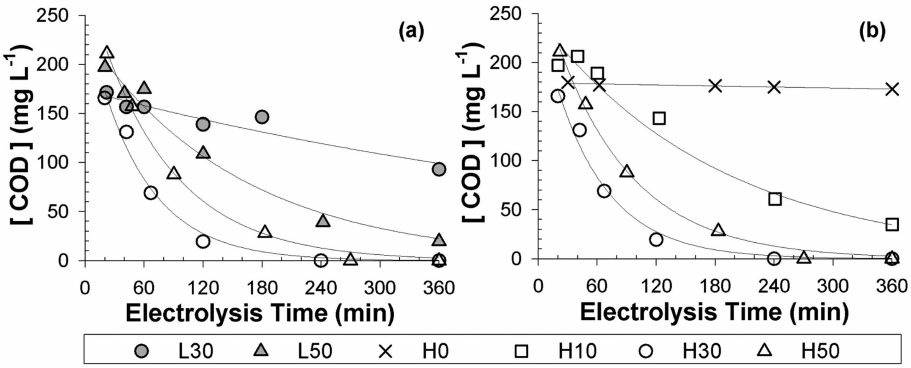

Figure B.3: COD vs time under variable applied anodic potential (L: 2.2 V, H: 3.0 V NHE) and added Cl^- (0, 10, 30, 50 mM) in domestic wastewater samples.

B.7 Impact of Cl and Cl_2^- on COD Removal.

The effects of $[Cl^-]_{ext.}$ were interpreted using a simple kinetic model applied to the data of experiments H10, H30, and H50. The CV profiles (Fig. 1) suggested that the oxidation of Cl^- produces RCS and chlorate in series. The oxidation of Cl^- and RCS as well as the homogeneous reaction between the RCS and COD were assumed to be first-order in each reactant.[137, 141, 142] The linear dependence of J on the [Cl^-] (Fig. S2) is consistent with first-order kinetics for RCS generation as follows

$$\frac{d[RCS]}{dt} = k_1 Cl^- - k_2[RCS]_{SS}[COD] - k_3 RCS_{SS} \approx 0 \tag{B.1}$$

$$\frac{d[COD]}{dt} = -k_2[RCS]_{SS}[COD] \approx -k_{COD}[COD] \tag{B.2}$$

$$\frac{ClO_3}{dt} = k_3[RCS]_{SS} \approx k_{ClO_3^-} \tag{B.3}$$

$$k_2 = k_3 \frac{k_{COD}}{k_{ClO_3^-}} \tag{B.4}$$

where k_1, k_2, and k_3 are rate constant for heterogeneous Cl_ oxidation to RCS, homogeneous reaction between RCS and COD, and heterogeneous RCS oxidation to chlorate. In addition, we assume a pseudo-steady-state condition for the rate of

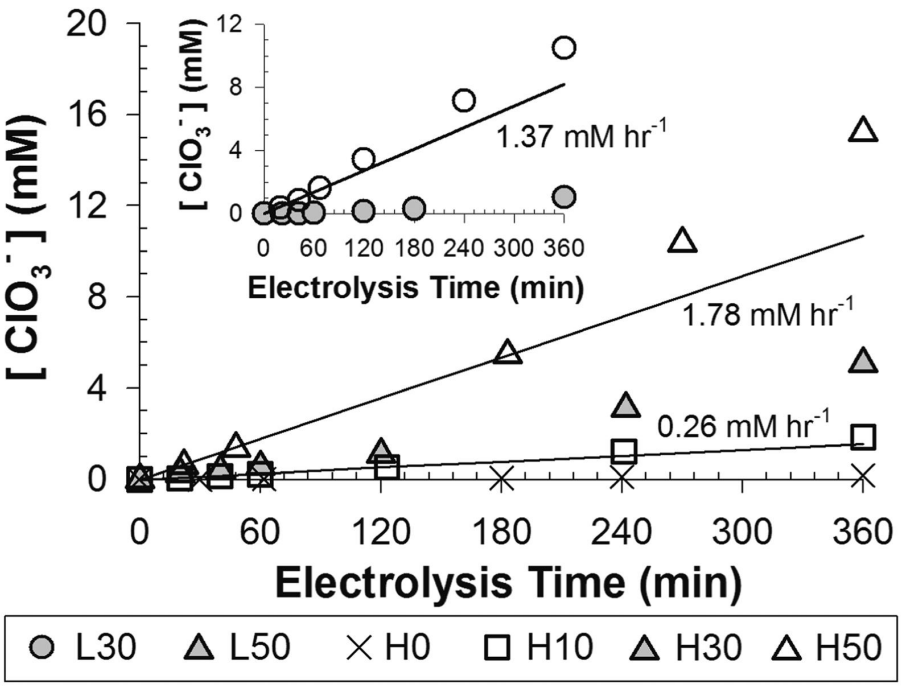

Figure B.4: [ClO$^-$] vs time using domestic wastewater samples under variable applied anodic potential (L: 2.2 V, H: 3.0 V NHE) and added Cl$^-$ concentration (0, 10, 30, 50 mM).

RCS production. The total chlorine concentration was negligible when the COD concentration was higher than 100 mg.L^{-1} (Fig. S3a). A linear relationship between [Cl$^-$] and [COD], indicated by eq 1 with quasi-constant [RCS], is supported by Fig. S3b. Furthermore, the steady-state assumption for [RCS] is self-consistent with the decrease in [COD] versus time, which follows apparent pseudo-first-order kinetics (Fig. 2). Therefore, the pseudo-first-order rate constant for COD removal (k_{COD}) and the pseudo-zero-order rate constant for chlorate production ($k^-_{ClO_3}$) can be expressed ClO_3 as the steady-state RCS concentration ($[RCS]_{SS}$) multiplied by the reactivity of the RCS toward the COD (k_2) and heterogeneous rate constant (k_3), respectively. It could be argued that the heterogeneous rate constants, k_1 and k_3, should vary with the electrolysis time as given by the Butler-Volmer formulation.[34]

Fig. B.4 shows [ClO_3^-] increasing faster after depletion of [COD]. Nevertheless, the rate of ClO_3^- formation appeared almost constant when the steady-state assumption for [RCS] was valid, as shown in Fig. 3(inset). From the observed $k_{ClO_3^-}$ and k_{COD},

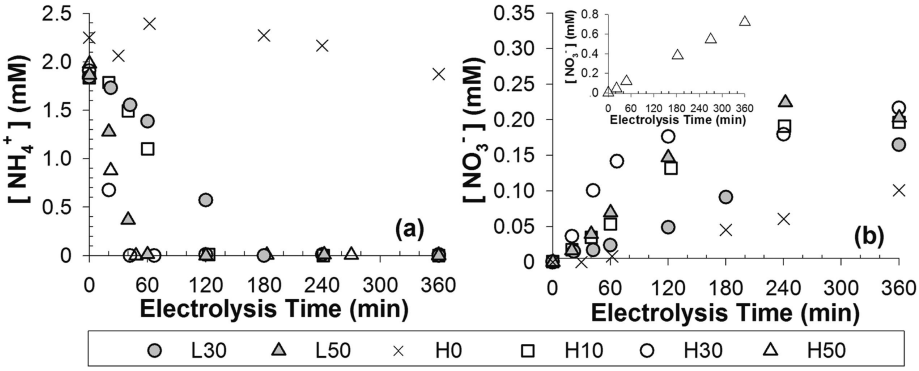

Figure B.5: $[NH_4^+]$ (a) and NO_3^- (b) under variable applied anodic potential (L: 2.2 V, H: 3.0 V NHE) and added Cl^- concentration (0, 10, 30, 50 mM) in electrolysis experiments using domestic wastewater samples.

the k_2/k_3 was calculated to be 1.1 mM^{-1} for H10, 0.60 mM^{-1} for H30, and 0.31 mM^{-1} for H50. Assuming that the k_3 is similar in each case, the reactivity between the RCS and COD (k_2) decreases as the $[Cl^-]_{ext.}$ increases.

B.8 CE and Energy Consumption for Anodic Reactions

The efficiency of electrochemical reactions is often expressed in $[Cl^-]$. The linear relation between the [COD] and $[Cl^-]$ also contributes to the apparent self-consistent current efficiencies. At lower anodic potentials (L30 and L50), in which the heterogeneous RCS generation is limiting, the increase in $[Cl^-]_{ext.}$ significantly enhanced the CE. In contrast, at higher potentials, where homogeneous reactions between RCS and COD become important, the CE for COD removal was the highest in the wastewater sample H30. Oxidation of NH_4^+ to NO_3^- and N_2 were minor fractions ($\sim$ 10%) of the anodic charge transfer due to the small initial $[NH_4^+]$. The CE for the observed residual chlorine were similar to those for ClO_3^- production and COD loss. The sum of the RCS mediated reactions was below 40%. The loss in CE can be attributed to O_2 evolution and RCS reduction at the cathode.

The corresponding specific energy consumption DPD(SEC) for COD removal at

t_{COD30}. The SEC was calculated as follows:

$$\text{Specific Energy Consumption} = \frac{\int_0^t (E_a - E_c) \times I dt}{([COD]^0 - [COD]^t) \times V} \times 100 \tag{B.5}$$

where E_a - E_c and I are cell voltage (V) and current (A), $[COD]^0$ and $[COD]^t$ are COD concentration ($mg.L^{-1}$) at the electrolysis time of zero and $t(h)$, and V is electrolyte volume (0.06 L). For galvanostatic electrolyses, an increasing [Cl^-] decreases the SEC by decreasing the cell voltage.[131, 143, 142] Under potentiostatic conditions, however, the SEC value has been reported to increase with [Cl^-] or conductivity via an increase in J.[144] Under both electrolytic conditions, increasing the cell voltage or current density for a given electrolyte composition normally increases the SEC.[139] In this regard, H30 gave the best space-time yield and SEC for COD removal at the high E_a. However, an increase in cell voltage and J at E_a of 3.0 V NHE requires larger energy consumption compared to E_a of 2.2 V NHE. Thus, the minimal energy usage was obtained with $[Cl^-]_{ext.}$ of 50 mM at Ea of 2.2 V NHE, which corresponds to a cell voltage of about 4 V.

B.9 Hydrogen Production

The generation rate of total gaseous products, the H_2 volumetric fraction and the H_2 molar flow rate increased with increasing current density. The fraction of H_2 was $\sim$ 40% in L30 and L50, while $\sim$ 60% in higher E_a. Other gaseous products would include O_2, H_2O, N_2, and CO_2.[130] The CE and energy efficiency of H_2 generation were calculated as follows

$$\text{Current Efficiency for Hydrogen Production (\%)} = \frac{2FQ_{H_2}t}{\int I dt} \times 100 \tag{B.6}$$

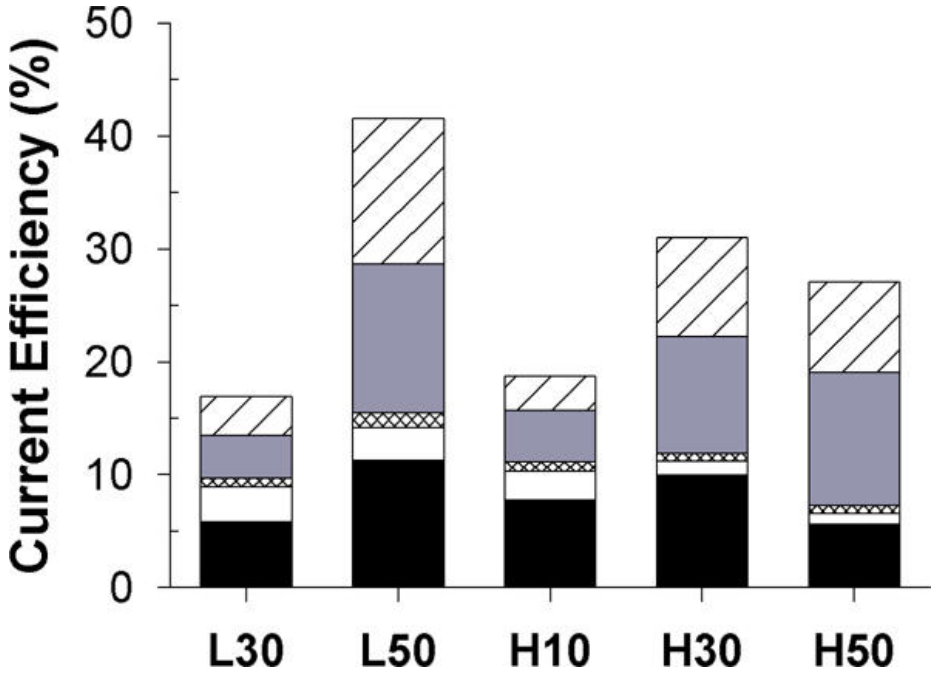

Figure B.6: General current efficiencies for anodic reactions including COD oxidation (black), formation of N_2 (white), NO_3^- (cross-hatched pattern), ClO_3^- (gray), and free chlorine (hatched pattern) under variable applied anodic potential (L: 2.2 V, H: 3.0 V NHE) and added Cl^- concentration (10, 30, 50 mM) in electrolysis experiments using domestic wastewater samples. Estimates are based on the time when COD decreases to below 30 mg.L^{-1}.

$$\text{Energy Efficiency for Hydrogen Production (\%)} = \frac{3600 \times 78 Wh.mole^{-1} Q_{H_2} \times t}{\int (E_a - E_c) \times I dt} \times 100 \quad \text{(B.7)}$$

where E_a - E_c and I are cell voltage (V) and current (A), QH_2 is H_2 molar production rate (mol.s^{-1}), t is time for gas collection (s), and F is Faraday constant (96485.3 C.mol^{-1}). The CE for H_2 generation was below 50% at low Ea and then increased with increasing J up to 84% at higher E_a. The remaining fraction of electron transfer at the cathode can be attributed to the combined reduction of RCS and O_2.[128, 145, 146] In particular, a reduction of the RCS would reduce the current efficiency both for desired anodic and cathodic reactions. We previously estimated[130, 145, 147] the CE for hydrogen generation in the range from 50% to 90% depending on cell voltage and, more importantly, the relative concentration of organic electron doners to chloride. An augmented presence of electron donors significantly increase the CE for H_2 generation via quenching the RCS. The energy efficiency for H_2 production was estimated to be from 14% to 26%. Higher energy efficiencies up to 46% have been reported under lower cell voltages ($\sim 3V$)[130] or under a photoelectrocatalytic operation of the BiO_x/ TiO_2 anode.[148] H_2 generated as a primary byproduct in WEC or PWEC can be used to in either a proton exchange membrane (PEM) or solid-state fuel cell. Therefore, a moderate reduction in the SEC is expected when utilizing the produced H_2 as a back-up energy source for the PWEC.

B.10 Prototype (20 L) PV-Powered Wastewater Electrolysis

If a PV panel DC output is connected directly to an electrolysis reactor, then the cell voltage and current will be affected by the electrolyte conductivity, temperature, and solar intensity. The E_a - E_c and J values are determined by the characteristic $I - V$ curve of a PV panel at a given incident solar radiation, the panel temperature, and the

resistance of the electrolysis cell.[149] We had previously reported[145] a solar energy conversion efficiency below 2% when using a PV panel that was directly connected to an electrolysis cell containing industrial wastewater. In order to increase the solar energy conversion efficiency, we employed a rechargeable lead acid battery regulated by a charge controller to generate an electrical energy output of $\sim 84W(12V \times 7A)$, while maintaining a constant cell

Bibliography

[1] J.-M. Tarascon and M. Armand, "Issues and challenges facing rechargeable lithium batteries," *Nature*, vol. 414, no. 6861, pp. 359–367, 2001.

[2] F. Orsini, A. Du Pasquier, B. Beaudoin, J. Tarascon, M. Trentin, N. Langenhuizen, E. De Beer, and P. Notten, "In situ scanning electron microscopy (sem) observation of interfaces within plastic lithium batteries," *Journal of power sources*, vol. 76, no. 1, pp. 19–29, 1998.

[3] K. Xu, "Nonaqueous liquid electrolytes for lithium-based rechargeable batteries," *Chemical reviews*, vol. 104, no. 10, pp. 4303–4418, 2004.

[4] R. Huggins, *Advanced batteries: materials science aspects*. Springer, 2008.

[5] M. Winter and R. J. Brodd, "What are batteries, fuel cells, and supercapacitors?," *Chemical reviews*, vol. 104, no. 10, pp. 4245–4270, 2004.

[6] D. Linden and T. B. Reddy, "Handbook of batteries," 1865.

[7] C. Monroe and J. Newman, "Dendrite growth in lithium/polymer systems a propagation model for liquid electrolytes under galvanostatic conditions," *Journal of The Electrochemical Society*, vol. 150, no. 10, pp. A1377–A1384, 2003.

[8] A. Aryanfar, D. Brooks, B. V. Merinov, W. A. Goddard, A. J. Colussi, and M. R. Hoffmann, "Dynamics of lithium dendrite growth and inhibition-pulse charging experiments and monte carlo calculations," *The Journal of Physical Chemistry Letters*, 2014.

[9] W. Xu, J. Wang, F. Ding, X. Chen, E. Nasybulin, Y. Zhang, and J.-G. Zhang, "Lithium metal anodes for rechargeable batteries," *Energy & Environmental Science*, vol. 7, no. 2, pp. 513–537, 2014.

[10] M. Armand and J.-M. Tarascon, "Building better batteries," *Nature*, vol. 451, no. 7179, pp. 652–657, 2008.

[11] F. Ding, W. Xu, G. L. Graff, J. Zhang, M. L. Sushko, X. Chen, Y. Shao, M. H. Engelhard, Z. Nie, J. Xiao, *et al.*, "Dendrite-free lithium deposition via self-healing electrostatic shield mechanism," *Journal of the American Chemical Society*, vol. 135, no. 11, pp. 4450–4456, 2013.

[12] S. Chandrashekar, N. M. Trease, H. J. Chang, L.-S. Du, C. P. Grey, and A. Jerschow, "7li mri of li batteries reveals location of microstructural lithium," *Nature materials*, vol. 11, no. 4, pp. 311–315, 2012.

[13] K. J. Harry, D. T. Hallinan, D. Y. Parkinson, A. A. MacDowell, and N. P. Balsara, "Detection of subsurface structures underneath dendrites formed on cycled lithium metal electrodes," *Nature materials*, vol. 13, no. 1, pp. 69–73, 2014.

[14] J. Rugolo and M. J. Aziz, "Electricity storage for intermittent renewable sources," *Energy & Environmental Science*, vol. 5, no. 5, pp. 7151–7160, 2012.

[15] B. Huskinson, M. P. Marshak, C. Suh, S. Er, M. R. Gerhardt, C. J. Galvin, X. Chen, A. Aspuru-Guzik, R. G. Gordon, and M. J. Aziz, "A metal-free organic-inorganic aqueous flow battery," *Nature*, vol. 505, no. 7482, pp. 195–198, 2014.

[16] J. B. Goodenough, "Rechargeable batteries: challenges old and new," *Journal of Solid State Electrochemistry*, vol. 16, no. 6, pp. 2019–2029, 2012.

[17] M. Z. Mayers, J. W. Kaminski, and T. F. Miller III, "Suppression of dendrite formation via pulse charging in rechargeable lithium metal batteries," *The Journal of Physical Chemistry C*, vol. 116, no. 50, pp. 26214–26221, 2012.

[18] T. Nishida, K. Nishikawa, M. Rosso, and Y. Fukunaka, "Optical observation of li dendrite growth in ionic liquid," *Electrochimica Acta*, vol. 100, pp. 333–341, 2013.

[19] N. Williard, W. He, C. Hendricks, and M. Pecht, "Lessons learned from the 787 dreamliner issue on lithium-ion battery reliability," *Energies*, vol. 6, no. 9, pp. 4682–4695, 2013.

[20] K. Nishikawa, T. Mori, T. Nishida, Y. Fukunaka, M. Rosso, and T. Homma, "In situ observation of dendrite growth of electrodeposited li metal," *Journal of The Electrochemical Society*, vol. 157, no. 11, pp. A1212–A1217, 2010.

[21] V. Fleury, "Branched fractal patterns in non-equilibrium electrochemical deposition from oscillatory nucleation and growth," *Nature*, vol. 390, no. 6656, pp. 145–148, 1997.

[22] J.-N. Chazalviel, "Electrochemical aspects of the generation of ramified metallic electrodeposits," *Physical review A*, vol. 42, no. 12, p. 7355, 1990.

[23] D. R. Ely and R. E. García, "Heterogeneous nucleation and growth of lithium electrodeposits on negative electrodes," *Journal of the Electrochemical Society*, vol. 160, no. 4, pp. A662–A668, 2013.

[24] R. Akolkar, "Mathematical model of the dendritic growth during lithium electrodeposition," *Journal of Power Sources*, vol. 232, pp. 23–28, 2013.

[25] C. Brissot, M. Rosso, J.-N. Chazalviel, and S. Lascaud, "In situ concentration cartography in the neighborhood of dendrites growing in lithium/polymer-electrolyte/lithium cells," *Journal of The Electrochemical Society*, vol. 146, no. 12, pp. 4393–4400, 1999.

[26] O. Crowther and A. C. West, "Effect of electrolyte composition on lithium dendrite growth," *Journal of The Electrochemical Society*, vol. 155, no. 11, pp. A806–A811, 2008.

[27] P. Howlett, D. MacFarlane, and A. Hollenkamp, "A sealed optical cell for the study of lithium-electrode— electrolyte interfaces," *Journal of power sources*, vol. 114, no. 2, pp. 277–284, 2003.

[28] N. Schweikert, A. Hofmann, M. Schulz, M. Scheuermann, S. T. Boles, T. Hanemann, H. Hahn, and S. Indris, "Suppressed lithium dendrite growth in lithium batteries using ionic liquid electrolytes: Investigation by electrochemical impedance spectroscopy, scanning electron microscopy, and in situ 7li nuclear magnetic resonance spectroscopy," *Journal of Power Sources*, vol. 228, pp. 237–243, 2013.

[29] A. Basile, A. F. Hollenkamp, A. I. Bhatt, and A. P. O'Mullane, "Extensive charge–discharge cycling of lithium metal electrodes achieved using ionic liquid electrolytes," *Electrochemistry Communications*, vol. 27, pp. 69–72, 2013.

[30] M. Rosso, T. Gobron, C. Brissot, J.-N. Chazalviel, and S. Lascaud, "Onset of dendritic growth in lithium/polymer cells," *Journal of power sources*, vol. 97, pp. 804–806, 2001.

[31] I. W. Seong, C. H. Hong, B. K. Kim, and W. Y. Yoon, "The effects of current density and amount of discharge on dendrite formation in the lithium powder anode electrode," *Journal of Power Sources*, vol. 178, no. 2, pp. 769–773, 2008.

[32] G. Stone, S. Mullin, A. Teran, D. Hallinan, A. Minor, A. Hexemer, and N. Balsara, "Resolution of the modulus versus adhesion dilemma in solid polymer electrolytes for rechargeable lithium metal batteries," *Journal of The Electrochemical Society*, vol. 159, no. 3, pp. A222–A227, 2012.

[33] E. Ben-Jacob and P. Garik, "The formation of patterns in non-equilibrium growth," *Nature*, vol. 343, pp. 523–530, 1990.

[34] A. J. Bard and L. R. Faulkner, *Electrochemical methods: fundamentals and applications*, vol. 2. Wiley New York, 1980.

[35] R. J. LeVeque, *Finite difference methods for ordinary and partial differential equations: steady-state and time-dependent problems*, vol. 98. Siam, 2007.

[36] X. H. Liu and J. Y. Huang, "In situ tem electrochemistry of anode materials in lithium ion batteries," *Energy & Environmental Science*, vol. 4, no. 10, pp. 3844–3860, 2011.

[37] X. Zhong, X. Guo, Y. Qiu, Z. Chen, and G. Zhang, "In situ study the electrochemical migration of tin under unipolar square wave electric field," *Journal of The Electrochemical Society*, vol. 160, no. 11, pp. D495–D500, 2013.

[38] C. Léger, F. Argoul, and M. Z. Bazant, "Front dynamics during diffusion-limited corrosion of ramified electrodeposits," *The Journal of Physical Chemistry B*, vol. 103, no. 28, pp. 5841–5851, 1999.

[39] M. Rosso, "Electrodeposition from a binary electrolyte: new developments and applications," *Electrochimica Acta*, vol. 53, no. 1, pp. 250–256, 2007.

[40] J. Diggle, A. Despic, and J. Bockris, "The mechanism of the dendritic electrocrystallization of zinc," *Journal of The Electrochemical Society*, vol. 116, no. 11, pp. 1503–1514, 1969.

[41] S. Roy, "Formation of dual diffusion layer by pulsing currents," *Industrial & Engineering Chemistry Research*, vol. 51, no. 4, pp. 1756–1760, 2011.

[42] M. Wang and N.-b. Ming, "Concentration field oscillation in front of a dendrite tip in electrochemical deposition," *Physical Review A*, vol. 45, no. 4, p. 2493, 1992.

[43] M. Z. Bazant, K. Thornton, and A. Ajdari, "Diffuse-charge dynamics in electrochemical systems," *Physical review E*, vol. 70, no. 2, p. 021506, 2004.

[44] J. D. Norton, H. S. White, and S. W. Feldberg, "Effect of the electrical double layer on voltammetry at microelectrodes," *Journal of physical chemistry*, vol. 94, no. 17, pp. 6772–6780, 1990.

[45] A. Alexe-Ionescu, G. Barbero, S. Bianco, G. Cicero, and C. Pirri, "Electrical response of electrolytic cells limited by different types of electrodes," *Journal of Electroanalytical Chemistry*, vol. 669, pp. 21–27, 2012.

[46] J. R. Macdonald, "Theory of ac space-charge polarization effects in photoconductors, semiconductors, and electrolytes," *Physical Review*, vol. 92, no. 1, p. 4, 1953.

[47] R. Hossain and K. Adamiak, "Dynamic properties of the electric double layer in electrolytes," *Journal of Electrostatics*, vol. 71, no. 5, pp. 829–838, 2013.

[48] N. Ibl, "Some theoretical aspects of pulse electrolysis," *Surface Technology*, vol. 10, no. 2, pp. 81–104, 1980.

[49] Z. Li, J. Huang, B. Yann Liaw, V. Metzler, and J. Zhang, "A review of lithium deposition in lithium-ion and lithium metal secondary batteries," *Journal of Power Sources*, vol. 254, pp. 168–182, 2014.

[50] J. Yamaki, S. Tobishima, and J. Besenhard, "Handbook of battery materials," *Handbook of Battery Materials*, 1999.

[51] I. Yoshimatsu, T. Hirai, and J.-i. Yamaki, "Lithium electrode morphology during cycling in lithium cells," *Journal of the Electrochemical Society*, vol. 135, no. 10, pp. 2422–2427, 1988.

[52] M. Arakawa, S. Tobishima, Y. Nemoto, M. Ichimura, and J. Yamaki, "Lithium electrode cycleability and morphology dependence on current density," *Journal of Power Sources*, vol. 43, pp. 27–35, 1993.

[53] D. Aurbach, I. Weissman, H. Yamin, and E. Elster, "The correlation between charge/discharge rates and morphology, surface chemistry, and performance of li electrodes and the connection to cycle life of practical batteries," *Journal of The Electrochemical Society*, vol. 145, no. 5, pp. 1421–1426, 1998.

[54] D. Aurbach, E. Zinigrad, H. Teller, and P. Dan, "Factors which limit the cycle life of rechargeable lithium (metal) batteries," *Journal of The Electrochemical Society*, vol. 147, no. 4, pp. 1274–1279, 2000.

[55] J. K. Stark, Y. Ding, and P. A. Kohl, "Dendrite-free electrodeposition and reoxidation of lithium-sodium alloy for metal-anode battery," *Journal of The Electrochemical Society*, vol. 158, no. 10, pp. A1100–A1105, 2011.

[56] J. Vaughey, G. Liu, and J.-G. Zhang, "Stabilizing the surface of lithium metal," *MRS Bulletin*, vol. 39, no. 05, pp. 429–435, 2014.

[57] D. Aurbach, E. Zinigrad, Y. Cohen, and H. Teller, "A short review of failure mechanisms of lithium metal and lithiated graphite anodes in liquid electrolyte solutions," *Solid State Ionics*, vol. 148, no. 3, pp. 405–416, 2002.

[58] C. Monroe and J. Newman, "The effect of interfacial deformation on electrodeposition kinetics," *Journal of The Electrochemical Society*, vol. 151, no. 6, pp. A880–A886, 2004.

[59] R. Akolkar, "Modeling dendrite growth during lithium electrodeposition at sub-ambient temperature," *Journal of Power Sources*, vol. 246, pp. 84–89, 2014.

[60] A. Aryanfar, A. J. Colussi, and M. R. Hoffmann, "Lithium dendrite growth control using local temperature variation," in *MRS Proceedings*, vol. 1680, pp. mrss14–1680, Cambridge Univ Press, 2014.

[61] C. Brissot, M. Rosso, J.-N. Chazalviel, and S. Lascaud, "Dendritic growth mechanisms in lithium/polymer cells," *Journal of power sources*, vol. 81, pp. 925–929, 1999.

[62] A. Aryanfar, M. R. Hoffmann, and A. J. Colussi, "Predictive modeling of size-dependent dendritic growth in dilute-electrolyte lithium metal batteries with potentiostatic cycling," in *Meeting Abstracts*, no. 11, pp. 1164–1164, The Electrochemical Society, 2012.

[63] J. Steiger, D. Kramer, and R. Mönig, "Mechanisms of dendritic growth investigated by¡ i¿ in situ¡/i¿ light microscopy during electrodeposition and dissolution of lithium," *Journal of Power Sources*, vol. 261, pp. 112–119, 2014.

[64] J. Steiger, D. Kramer, and R. Mönig, "Microscopic observations of the formation, growth and shrinkage of lithium moss during electrodeposition and dissolution," *Electrochimica Acta*, 2014.

[65] A. Aryanfar, M. Hoffmann, and A. Colussi, "Investigation of lithium dendrite necking and formation of dead lithium crystals," in *Meeting Abstracts*, no. 8, pp. 506–506, The Electrochemical Society, 2014.

[66] C. Léger, J. Elezgaray, and F. Argoul, "Internal structure of dense electrodeposits," *Physical Review E*, vol. 61, no. 5, p. 5452, 2000.

[67] J.-i. Yamaki, S.-i. Tobishima, K. Hayashi, K. Saito, Y. Nemoto, and M. Arakawa, "A consideration of the morphology of electrochemically deposited lithium in an organic electrolyte," *Journal of Power Sources*, vol. 74, no. 2, pp. 219–227, 1998.

[68] K. Saito, M. Arakawa, S. Tobishima, and J. Yamaki, "Specific surface-area measurement of lithium anode in rechargeable lithium cells," *Journal of power sources*, vol. 72, no. 2, pp. 111–117, 1998.

[69] A. Aryanfar, "Method and device for dendrite research and discovery in batteries," Mar. 10 2014. US Patent App. 14/201,979.

[70] P. P. Trigueros, J. Claret, F. Mas, and F. Sagués, "Some effects of cell dimensions on zinc electrodeposits," *Journal of Electroanalytical Chemistry*, vol. 328, no. 1, pp. 165–178, 1992.

[71] N. Otsu, "A threshold selection method from gray-level histograms," *Automatica*, vol. 11, no. 285-296, pp. 23–27, 1975.

[72] J. Barton and J. Bockris, "The electrolytic growth of dendrites from ionic solutions," *Proceedings of the Royal Society of London. Series A. Mathematical and Physical Sciences*, vol. 268, no. 1335, pp. 485–505, 1962.

[73] K. Doll, N. Harrison, and V. Saunders, "A density functional study of lithium bulk and surfaces," *Journal of Physics: Condensed Matter*, vol. 11, no. 26, p. 5007, 1999.

[74] I. Galanakis, N. Papanikolaou, and P. Dederichs, "Applicability of the broken-bond rule to the surface energy of the fcc metals," *Surface science*, vol. 511, no. 1, pp. 1–12, 2002.

[75] F. van Swol, S. R. Challa, and J. A. Shelnutt, "A thermodynamic perspective of the metastability of holey sheets: the role of curvature," *Physical Chemistry Chemical Physics*, vol. 14, no. 38, pp. 13309–13318, 2012.

[76] L. Yang, C. Smith, C. Patrissi, C. R. Schumacher, and B. L. Lucht, "Surface reactions and performance of non-aqueous electrolytes with lithium metal anodes," *Journal of Power Sources*, vol. 185, no. 2, pp. 1359–1366, 2008.

[77] D. Aurbach, "Review of selected electrode–solution interactions which determine the performance of li and li ion batteries," *Journal of Power Sources*, vol. 89, no. 2, pp. 206–218, 2000.

[78] D. Aurbach, M. Daroux, P. Faguy, and E. Yeager, "Identification of surface films formed on lithium in propylene carbonate solutions," *Journal of The Electrochemical Society*, vol. 134, no. 7, pp. 1611–1620, 1987.

[79] M. Sun, H.-G. Liao, K. Niu, and H. Zheng, "Structural and morphological evolution of lead dendrites during electrochemical migration," *Scientific reports*, vol. 3, 2013.

[80] A. Aryanfar, D. J. Brooks, A. J. Colussi, B. V. Merinov, W. A. Goddard III, and M. R. Hoffmann, "Thermal relaxation of lithium dendrites," *Physical Chemistry Chemical Physics*, vol. 17, no. 12, pp. 8000–8005, 2015.

[81] B. Dunn, H. Kamath, and J.-M. Tarascon, "Electrical energy storage for the grid: a battery of choices," *Science*, vol. 334, no. 6058, pp. 928–935, 2011.

[82] H. Kim, G. Jeong, Y.-U. Kim, J.-H. Kim, C.-M. Park, and H.-J. Sohn, "Metallic anodes for next generation secondary batteries," *Chemical Society Reviews*, vol. 42, no. 23, pp. 9011–9034, 2013.

[83] J. B. Goodenough, "Evolution of strategies for modern rechargeable batteries," *Accounts of chemical research*, vol. 46, no. 5, pp. 1053–1061, 2012.

[84] R. L. Sacci, N. J. Dudney, K. L. More, L. R. Parent, I. Arslan, N. D. Browning, and R. R. Unocic, "Direct visualization of initial sei morphology and growth kinetics during lithium deposition by in situ electrochemical transmission electron microscopy," *Chemical Communications*, vol. 50, no. 17, pp. 2104–2107, 2014.

[85] C. M. López, J. T. Vaughey, and D. W. Dees, "Morphological transitions on lithium metal anodes," *Journal of the Electrochemical Society*, vol. 156, no. 9, pp. A726–A729, 2009.

[86] C. Brissot, M. Rosso, J.-N. Chazalviel, P. Baudry, and S. Lascaud, "¡ i¿ in situ¡/i¿ study of dendritic growth inlithium/peo-salt/lithium cells," *Electrochimica acta*, vol. 43, no. 10, pp. 1569–1574, 1998.

[87] C. M. López, J. T. Vaughey, and D. W. Dees, "Insights into the role of interphasial morphology on the electrochemical performance of lithium electrodes," *Journal of The Electrochemical Society*, vol. 159, no. 6, pp. A873–A886, 2012.

[88] P.-L. Taberna, S. Mitra, P. Poizot, P. Simon, and J.-M. Tarascon, "High rate capabilities fe3o4-based cu nano-architectured electrodes for lithium-ion battery applications," *Nature materials*, vol. 5, no. 7, pp. 567–573, 2006.

[89] B. Scrosati and J. Garche, "Lithium batteries: Status, prospects and future," *Journal of Power Sources*, vol. 195, no. 9, pp. 2419–2430, 2010.

[90] P. G. Bruce, B. Scrosati, and J.-M. Tarascon, "Nanomaterials for rechargeable lithium batteries," *Angewandte Chemie International Edition*, vol. 47, no. 16, pp. 2930–2946, 2008.

[91] E. S. Nimon and A. V. Churikov, "Electrochemical behaviour of li, sn, li, cd and li, sn, cd alloys in propylene carbonate solution," *Electrochimica acta*, vol. 41, no. 9, pp. 1455–1464, 1996.

[92] J. B. Goodenough and Y. Kim, "Challenges for rechargeable batteries," *Journal of Power Sources*, vol. 196, no. 16, pp. 6688–6694, 2011.

[93] J. B. Goodenough and K.-S. Park, "The li-ion rechargeable battery: a perspective," *Journal of the American Chemical Society*, vol. 135, no. 4, pp. 1167–1176, 2013.

[94] A. Aryanfar, D. J. Brooks, A. J. Colussi, and M. R. Hoffmann, "Quantifying the dependence of dead lithium losses on the cycling period in lithium metal batteries," *Physical Chemistry Chemical Physics*, vol. 16, no. 45, pp. 24965–24970, 2014.

[95] R. Khurana, J. Schaefer, L. A. Archer, and G. W. Coates, "Suppression of lithium dendrite growth using cross-linked polyethylene/polyethylene oxide electrolytes: A new approach for practical lithium-metal polymer batteries," *Journal of the American Chemical Society*, 2014.

[96] J. Graetz, C. Ahn, R. Yazami, and B. Fultz, "Highly reversible lithium storage in nanostructured silicon," *Electrochemical and Solid-State Letters*, vol. 6, no. 9, pp. A194–A197, 2003.

[97] T. Trimble and R. Cammarata, "Many-body effects on surface stress, surface energy and surface relaxation of fcc metals," *Surface Science*, vol. 602, no. 14, pp. 2339–2347, 2008.

[98] A. Gross, *Theoretical surface science: a microscopic perspective*. Springer New York, 2003.

[99] J. Sullivan, D. Hanson, and R. Keller, "Diffusion coefficients in propylene carbonate, dimethyl formamide, acetonitrile, and methyl formate," *Journal of The Electrochemical Society*, vol. 117, no. 6, pp. 779–780, 1970.

[100] H. Jonsson, "Theoretical studies of atomic-scale processes relevant to crystal growth," *Annual review of physical chemistry*, vol. 51, no. 1, pp. 623–653, 2000.

[101] A. Zhamu, G. Chen, C. Liu, D. Neff, Q. Fang, Z. Yu, W. Xiong, Y. Wang, X. Wang, and B. Z. Jang, "Reviving rechargeable lithium metal batteries: enabling next-generation high-energy and high-power cells," *Energy & Environmental Science*, vol. 5, no. 2, pp. 5701–5707, 2012.

[102] P. K. Muhuri and D. K. Hazra, "Density and viscosity for propylene carbonate+ 1, 2-dimethoxyethane at 298.15, 308.15, and 318.15 k," *Journal of Chemical and Engineering Data*, vol. 39, no. 2, pp. 375–377, 1994.

[103] H. Brune, "Thermal dynamics at surfaces," *Annalen der Physik*, vol. 18, no. 10-11, pp. 675–698, 2009.

[104] C. Kittel, *Elementary statistical physics*. Courier Dover Publications, 2004.

[105] Y. Lu, Z. Tu, and L. A. Archer, "Stable lithium electrodeposition in liquid and nanoporous solid electrolytes," *Nature materials*, 2014.

[106] G. Antczak and G. Ehrlich, *Surface diffusion: metals, metal atoms, and clusters*. Cambridge University Press, 2010.

[107] E. Seebauer and C. Allen, "Estimating surface diffusion coefficients," *Progress in Surface Science*, vol. 49, no. 3, pp. 265–330, 1995.

[108] T. Ala-Nissila and S. Ying, "Theory of classical surface diffusion," *Progress in surface science*, vol. 39, no. 3, pp. 227–323, 1992.

[109] D. A. Reed and G. Ehrlich, "Surface diffusion, atomic jump rates and thermodynamics," *Surface Science*, vol. 102, no. 2, pp. 588–609, 1981.

[110] S.-Y. Chang, C.-E. Li, Y.-C. Huang, H.-F. Hsu, J.-W. Yeh, and S.-J. Lin, "Structural and thermodynamic factors of suppressed interdiffusion kinetics in multi-component high-entropy materials," *Scientific reports*, vol. 4, 2014.

[111] L. P. Jeurgens, Z. Wang, and E. J. Mittemeijer, "Thermodynamics of reactions and phase transformations at interfaces and surfaces," *International Journal of Materials Research*, vol. 100, no. 10, pp. 1281–1307, 2009.

[112] J. Sun and S. Simon, "The melting behavior of aluminum nanoparticles," *Thermochimica Acta*, vol. 463, no. 1, pp. 32–40, 2007.

[113] P. Couchman and W. Jesser, "Thermodynamic theory of size dependence of melting temperature in metals," 1977.

[114] L. Wang, "Vacancy formation and squashing during surface melting and the size effect on surface-induced melting of metals," *Philosophical Magazine*, vol. 93, no. 27, pp. 3648–3663, 2013.

[115] B. Alchagirov, L. K. Afaunova, F. Dyshekova, A. Mozgovoi, T. Taova, and R. K. Arkhestov, "The density and surface tension of liquid lithium at melting temperature," *High Temperature*, vol. 47, no. 2, pp. 287–291, 2009.

[116] A. A. Grosse, "The relationship between surface tension and energy of liquid metals and their heat of vaporization at the melting point," *Journal of Inorganic and Nuclear Chemistry*, vol. 26, no. 8, pp. 1349–1361, 1964.

[117] A. Tudela Ribes, P. Beaunier, P. Willmann, and D. Lemordant, "Correlation between cycling efficiency and surface morphology of electrodeposited lithium. effect of fluorinated surface active additives," *Journal of power sources*, vol. 58, no. 2, pp. 189–195, 1996.

[118] P. Ehrhart, *Atomic defects in metals*, vol. 25. Springer, 1991.

[119] Q. Mei and K. Lu, "Melting of metals: role of concentration and migration of vacancies at surfaces," *Philosophical Magazine Letters*, vol. 88, no. 3, pp. 203–211, 2008.

[120] H. E. Park, C. H. Hong, and W. Y. Yoon, "The effect of internal resistance on dendritic growth on lithium metal electrodes in the lithium secondary batteries," *Journal of Power Sources*, vol. 178, no. 2, pp. 765–768, 2008.

[121] C. Brissot, M. Rosso, J.-N. Chazalviel, and S. Lascaud, "Concentration measurements in lithium/polymer–electrolyte/lithium cells during cycling," *Journal of power sources*, vol. 94, no. 2, pp. 212–218, 2001.

[122] R. Bhattacharyya, B. Key, H. Chen, A. S. Best, A. F. Hollenkamp, and C. P. Grey, "In situ nmr observation of the formation of metallic lithium microstructures in lithium batteries," *Nature materials*, vol. 9, no. 6, pp. 504–510, 2010.

[123] A. C. Van Duin, S. Dasgupta, F. Lorant, and W. A. Goddard, "Reaxff: a reactive force field for hydrocarbons," *The Journal of Physical Chemistry A*, vol. 105, no. 41, pp. 9396–9409, 2001.

[124] L. Mandeltort and J. T. Yates Jr, "Rapid atomic li surface diffusion and intercalation on graphite: A surface science study," *The Journal of Physical Chemistry C*, vol. 116, no. 47, pp. 24962–24967, 2012.

[125] C. Comninellis, "Electrocatalysis in the electrochemical conversion/combustion of organic pollutants for waste water treatment," *Electrochimica Acta*, vol. 39, no. 11, pp. 1857–1862, 1994.

[126] C. A. Martinez-Huitle and S. Ferro, "Electrochemical oxidation of organic pollutants for the wastewater treatment: direct and indirect processes," *Chemical Society Reviews*, vol. 35, no. 12, pp. 1324–1340, 2006.

[127] M. Panizza and G. Cerisola, "Direct and mediated anodic oxidation of organic pollutants," *Chemical Reviews*, vol. 109, no. 12, pp. 6541–6569, 2009.

[128] H. Park, C. D. Vecitis, and M. R. Hoffmann, "Electrochemical water splitting coupled with organic compound oxidation: the role of active chlorine species," *The Journal of Physical Chemistry C*, vol. 113, no. 18, pp. 7935–7945, 2009.

[129] K. Cho, D. Kwon, and M. R. Hoffmann, "Electrochemical treatment of human waste coupled with molecular hydrogen production," *RSC Advances*, vol. 4, no. 9, pp. 4596–4608, 2014.

[130] H. Park, C. D. Vecitis, and M. R. Hoffmann, "Solar-powered electrochemical oxidation of organic compounds coupled with the cathodic production of molecular hydrogen," *The Journal of Physical Chemistry A*, vol. 112, no. 33, pp. 7616–7626, 2008.

[131] G. Malpass, D. Miwa, D. Mortari, S. Machado, and A. Motheo, "Decolorisation of real textile waste using electrochemical techniques: effect of the chloride concentration," *Water research*, vol. 41, no. 13, pp. 2969–2977, 2007.

[132] P. Shuk, H.-D. Wiemhöfer, U. Guth, W. Göpel, and M. Greenblatt, "Oxide ion conducting solid electrolytes based on bi2o3," *Solid State Ionics*, vol. 89, no. 3, pp. 179–196, 1996.

[133] S. Trasatti, "Progress in the understanding of the mechanism of chlorine evolution at oxide electrodes," *Electrochimica acta*, vol. 32, no. 3, pp. 369–382, 1987.

[134] M. H. Santana and L. A. De Faria, "Oxygen and chlorine evolution on ruo2 tio2 ceo2 nb2 o5 mixed oxide electrodes," *Electrochimica acta*, vol. 51, no. 17, pp. 3578–3585, 2006.

[135] M. Deborde and U. von Gunten, "Reactions of chlorine with inorganic and organic compounds during water treatment kinetics and mechanisms: a critical review," *Water research*, vol. 42, no. 1, pp. 13–51, 2008.

[136] L. Czarnetzki and L. Janssen, "Formation of hypochlorite, chlorate and oxygen during nacl electrolysis from alkaline solutions at an ruo2/tio2 anode," *Journal of Applied Electrochemistry*, vol. 22, no. 4, pp. 315–324, 1992.

[137] Y. J. Jung, K. W. Baek, B. S. Oh, and J.-W. Kang, "An investigation of the formation of chlorate and perchlorate during electrolysis using pt/ti electrodes: The effects of ph and reactive oxygen species and the results of kinetic studies," *Water research*, vol. 44, no. 18, pp. 5345–5355, 2010.

[138] O. Scialdone, S. Randazzo, A. Galia, and G. Silvestri, "Electrochemical oxidation of organics in water: role of operative parameters in the absence and in the presence of nacl," *Water research*, vol. 43, no. 8, pp. 2260–2272, 2009.

[139] A. Fernandes, M. Pacheco, L. Ciríaco, and A. Lopes, "Anodic oxidation of a biologically treated leachate on a boron-doped diamond anode," *Journal of hazardous materials*, vol. 199, pp. 82–87, 2012.

[140] D. Miwa, G. Malpass, S. Machado, and A. Motheo, "Electrochemical degradation of carbaryl on oxide electrodes," *Water research*, vol. 40, no. 17, pp. 3281–3289, 2006.

[141] M. Panizza and G. Cerisola, "Olive mill wastewater treatment by anodic oxidation with parallel plate electrodes," *Water Research*, vol. 40, no. 6, pp. 1179–1184, 2006.

[142] C. R. Costa and P. Olivi, "Effect of chloride concentration on the electrochemical treatment of a synthetic tannery wastewater," *Electrochimica Acta*, vol. 54, no. 7, pp. 2046–2052, 2009.

[143] G. Malpass, D. Miwa, S. Machado, P. Olivi, and A. Motheo, "Oxidation of the pesticide atrazine at dsa electrodes," *Journal of hazardous materials*, vol. 137, no. 1, pp. 565–572, 2006.

[144] M. Gotsi, N. Kalogerakis, E. Psillakis, P. Samaras, and D. Mantzavinos, "Electrochemical oxidation of olive oil mill wastewaters," *Water Research*, vol. 39, no. 17, pp. 4177–4187, 2005.

[145] J. Choi, Y. Qu, and M. R. Hoffmann, "Sno2, iro2, ta2o5, bi2o3, and tio2 nanoparticle anodes: electrochemical oxidation coupled with the cathodic reduction of water to yield molecular h2," *Journal of Nanoparticle Research*, vol. 14, no. 8, pp. 1–12, 2012.

[146] J. Kim, W. J. K. Choi, J. Choi, M. R. Hoffmann, and H. Park, "Electrolysis of urea and urine for solar hydrogen," *Catalysis Today*, vol. 199, pp. 2–7, 2013.

[147] H. Park, K.-H. Choo, H.-S. Park, J. Choi, and M. R. Hoffmann, "Electrochemical oxidation and microfiltration of municipal wastewater with simultaneous hydrogen production: Influence of organic and particulate matter," *Chemical Engineering Journal*, vol. 215, pp. 802–810, 2013.

[148] H. Park, A. Bak, Y. Y. Ahn, J. Choi, and M. R. Hoffmann, "Photoelectrochemical performance of multi-layered biox-tio2 ti electrodes for degradation of phenol and production of molecular hydrogen in water," *Journal of hazardous materials*, vol. 211, pp. 47–54, 2012.

[149] D. Valero, J. M. Ortiz, E. Expósito, V. Montiel, and A. Aldaz, "Electrochemical wastewater treatment directly powered by photovoltaic panels: electrooxidation of a dye-containing wastewater," *Environmental science & technology*, vol. 44, no. 13, pp. 5182–5187, 2010.